Adhesion Measurements on Patterned Elastomeric Surfaces

Dissertation
zur Erlangung des Grades
des Doktors der Naturwissenschaften
der Naturwissenschaftlich-Technischen Fakultät III
Chemie, Pharmazie, Bio- und Werkstoffwissenschaften
der Universität des Saarlandes

von

Elmar K. Kroner

Angefertigt am INM – Leibniz-Institut für Neue Materialien
Programmbereich Funktionelle Oberflächen
Universität des Saarlandes

Saarbrücken
01.03.2011

Tag des Kolloquiums: 08. Juli 2011

Vorsitzender:
Prof. Dr.-Ing. F. Mücklich

Berichterstatter:
Prof. Dr. E. Arzt
Prof. Dr. W. Possart
Prof. Dr. A. Crosby

Akademischer Beisitzer:
Dr.-Ing. Aubertin

Danksagung

Diese Arbeit ist im Zeitraum vom 01.01.2008 bis zum 01.03.2011 am INM – Leibniz-Institut für Neue Materialien in Saarbrücken entstanden.

Bei einer Dissertation steht in der Regel der Autor im Mittelpunkt. Man wird für seine Arbeit bewundert, geschätzt, manchmal auch beneidet – in jedem Falle aber erhält man große Beachtung. Dabei wird leider allzu oft vergessen, dass eine Dissertation nicht die Arbeit eines Einzelnen widerspiegelt, sondern vielmehr die Zusammenarbeit Vieler darstellt. An dieser Stelle möchte ich mich deshalb bei allen bedanken, die mich bei dieser Arbeit unterstützt haben, sowohl aus wissenschaftlicher Sicht, als auch im privaten Bereich. Einige Personen möchte ich dabei gesondert erwähnen.

Zu aller erst möchte ich mich bei *Prof. Dr. Eduard Arzt* bedanken, in dessen Programmbereich ich diese Arbeiten durchgeführt habe und der mein Betreuer über die gesamte Zeit war. Die Inspiration durch wissenschaftliche Diskussionen, die fokussierte Arbeitsweise, aber auch seine Fairness und der menschliche Umgang verdienen meinen allergrößten Respekt und waren für mich immer eine Quelle neuer Energie zum weiteren Forschen.

Prof. Dr. Wulff Possart, der den Mitbericht dieser Dissertation übernommen hat, eröffnete für mich immer neue Sichtweisen von wissenschaftlichen Problemen. Bei jedem Treffen mit ihm hat sich mein Horizont ein Stück erweitert und neue Wege taten sich auf.

Herzlich möchte ich mich auch bei *Prof. Dr. Robert McMeeking* bedanken, der mich in die Welt der Kontakttheorie entführt hat, um mich dort wie Alice im Wunderland zu bewegen. Auf ihn geht auch Kapitel 6.4.3 zurück. Danke auch an *Prof. Dr. Roya Maboudian*, mit der ich einige Zeit zusammen arbeiten und aus ihren Erfahrungen lernen durfte.

Inspirierende Diskussionen, neue Ideen, Lösung von Problemen, wissenschaftliche Kaffeepausen – für all das möchte ich mich bei meinen Kollegen, vor allem *Dr. Marleen Kamperman*, *Dadhichi Paretkar*, *Jessica Kaiser*, *Dr. Andreas Schneider* und *Dr. Baptiste Girault*, aus dem *Programmbereich Funktionelle Oberflächen* bedanken. Nicht zu vergessen sind an dieser Stelle auch die *Kollegen aus den anderen Programmbereichen*, die immer bei Problemen halfen, oder wenn nötig mit einer Runde Tischkicker meinen Kopf frei machten.

Ein Wissenschaftler ist immer nur so gut, wie diejenigen, mit denen er arbeitet. Ohne die unermüdliche Arbeit an MAD und den tollen Ideen von *Joachim Blau* wäre die Arbeit sicherlich nicht das geworden, was sie ist. Ebenso möchte ich mich bei den *Mitarbeitern der Werkstatt des INM* bedanken, die für mich Unmögliches möglich gemacht haben. Große Unterstützung habe ich auch von *Günter Marchand* erhalten, durch den die Aufenthalte im Reinraum zu einem neuen Erlebnis wurden.

Ein großer Dank gilt *meiner Familie*, die mir zu jeder Zeit den Rücken frei hielten und die für mich immer da waren, da sind und da sein werden, und das, obwohl meine Arbeit mich räumlich und zeitlich von meiner Familie getrennt hat und ich ihr bei Weitem nicht die Zeit und Nähe geben konnte, die sie verdient hätte.

Vor allem aber möchte ich *Karla Hillerich* für die Kraft und den Rückhalt danken, den ich von ihr in den gemeinsamen Jahren erhalten habe. Dies möchte ich mit den Worten Reinhard Meys ausdrücken: „Lachen und Weinen sind in jener Zeit verklungen, die in Siebenmeilen-Stiefeln an uns vorübereilt, und von den besten all meiner Erinnerungen hab‘ ich die schönsten, meine Freundin, wohl mit Dir geteilt. Nein, keine Stunde gibt‘s, die ich bereute, und mir bleibt nur als Trost dafür, dass keine wiederkehrt: Viel mehr als gestern liebe ich Dich heute, doch weniger, als ich Dich morgen lieben werd‘.“ Danke!

Index

Symbols and Abbreviations

a	contact radius, [m]
b	width of square probe, [m]
c	contact length of square probe, [m]
c_0	half length of square probe at zero load [m]
δ	indentation depth, [m]
ε	strain, [-]
E	Young´s modulus, [N/m^2]
E^*	reduced Young´s modulus, [N/m^2]
K	reduced stiffness, [m^2/N]
K_I^x	stress intensity factor at position x, [$N/m^{3/2}$]
l	pillar length, [m]
Δl	length change of the sample [m]
$\Delta l_{backing}$	indentation into the backing layer [m]
Δl_{pillar}	length change of the pillar [m]
Δl_{tip}	length change of the tip [m]
n	number of contacts, [-]
P	load, [N]
P_p	preload, [N]
P_c	pull-off force, [N]

R	sphere radius, [m]
s	splitting efficiency, [-]
θ	tilt angle, [°]
μ	Tabor parameter, [-]
υ	Poisson number, [-]
ω	work of adhesion, [N/m]
γ	surface energy, [N/m]
γ_{xy}	interfacial energy of materials x and y, [N/m]
z_0	equilibrium separation distance, [m]

AFM	Atomic Force Microscopy
AR	Aspect Ratio
CNT	Carbon NanoTubes
DMT	Derjaguin-Muller-Toporov
FIB	Focused Ion Beam
ICP	Inductively Coupled Plasma
JKR	Johnson-Kendall-Roberts
MAD	Macroscopic Adhesion measurement Device
PDMS	Poly(DiMethyl)Siloxane
PU	PolyUrethane
RF	Radio Frequency
RIE	Reactive Ion Etching
SEM	Scanning Electron Microscopy
WLI	White Light Interferometry

Abstract

Since the discovery of the gecko's hairy attachment pads, scientists tried to mimic these surface patterns due to the unique adhesion properties. Lately, scientists succeeded to fabricate artificial adhesives, which show similar complexity in geometry and achieved adhesive forces, exceeding the sticking forces of geckos. Due to the increasing commercial interest, a race has started to fabricate more complex surface patterns. However, due to this race some fundamental scientific aspects have fallen into oblivion, e.g. the distinction between real effects and measurement artefacts. In this work, the adhesion of patterned surfaces was investigated using different probe geometries. It was shown that the adhesion changes with the number of contacts due to material transfer between sample and probe. Adhesion measurements with flat and spherical probes on patterned surfaces were compared and the angle dependent adhesion was determined. Flat tip pillars showed a large tilt angle dependency, while pillars with spherical and mushroom shaped tips exhibited angle independent pull-off forces. Due to the angle dependencies, spherical probes tended to underestimate the adhesion of patterned surfaces compared to well-aligned flat probes. Flat probe measurements allowed a closer investigation of contact phenomena and yielded new information on adhesion and mechanical properties of patterned surfaces. These results may help in a more successful design of bioinspired adhesives.

Zusammenfassung

Seit Entdeckung der Oberflächenstruktur von Geckozehen haben Wissenschaftler versucht, diese wegen ihrer einzigartigen Hafteigenschaften zu kopieren. Kürzlich ist es gelungen, Haftsysteme mit ähnlich komplexen Strukturen zu entwickeln, die die Haftkräfte des Geckos sogar übertreffen. Aufgrund des wachsenden kommerziellen Interesses werden immer komplexere Strukturen hergestellt. Dabei werden jedoch fundamentale wissenschaftliche Prinzipien vernachlässigt: der Unterschied zwischen Effekt und Messartefakt. In dieser Arbeit wurde die Adhäsion strukturierter Oberflächen mit unterschiedlichen Prüfkörpergeometrien bestimmt. Dabei wurde gezeigt, dass sich die Haftkraft aufgrund von Materialtransfer mit der Anzahl der Kontakte zwischen Prüfkörper und Probe ändert. Adhäsionsmessungen mit sphärischen und flachen Prüfkörpern wurden verglichen. Flache Prüfkörper erlaubten dabei eine Quantifizierung der winkelabhängigen Adhäsion. Strukturen mit flachen Enden zeigen, im Gegensatz zu Strukturen mit sphärischen und pilzförmigen Enden, winkelabhängige Adhäsion. Aus diesem Grund wird bei Adhäsionsmessungen mit sphärischen Prüfkörpern die Haftkraft strukturierter Oberflächen oftmals unterschätzt. Messungen mit flachen Prüfkörpern ermöglichen eine genauere Untersuchung von Kontaktphänomenen und liefern zusätzliche Informationen über Adhäsion und mechanische Eigenschaften von strukturierten Oberflächen. Diese Ergebnisse können dabei helfen, bioinspirierte Haftsysteme weiter zu optimieren.

1. Introduction

During evolution, several animals have developed and optimized astonishing adhesion systems to adapt to their natural habitat. The variety in these systems is as big as the variety of the animals themselves. Mussels for example have developed a very strong irreversible adhesion system [1-3]. They attach themselves to reefs or the hull of ships and can only be removed by brute force – the mussels cannot be flushed away even by very strong tides, although they live in a highly aggressive environment. Other animals like slugs or tree-frogs owe their adhesion abilities to a constantly produced secretion [4-14]. This also prevents them from drying out and acts as a protection layer. A third class of adhesion systems found in nature is the so-called "dry" adhesion. Various insects, spiders and lizards have developed hairy adhesion systems where van der Waals forces – sometimes in combination with capillary forces – help these animals to walk up walls and stick even to ceilings [15-18]. Due to the physical nature of van der Waals forces, these animals can stick to nearly every kind of surface, almost independent of the surface chemistry or roughness. The absence of secretions results in a "clean" adhesion system, which can be detached almost without residues. As the gecko is the largest known animal supporting a dry adhesion system, it has been the subject of intensive investigation. But only since the development of electron microscopy has the mystery of gecko adhesion been explained scientifically.

The investigation of gecko toe pads reveals a hairy surface with hierarchical design [19]. Each toe is covered with thousands of micrometer thick hairs, which branch into millions of finer hairs terminating in tips with dimensions in the range of tens of nanometers [18,20-34]. Figure 1.1 shows the hierarchical nature of the gecko's adhesion system [35].

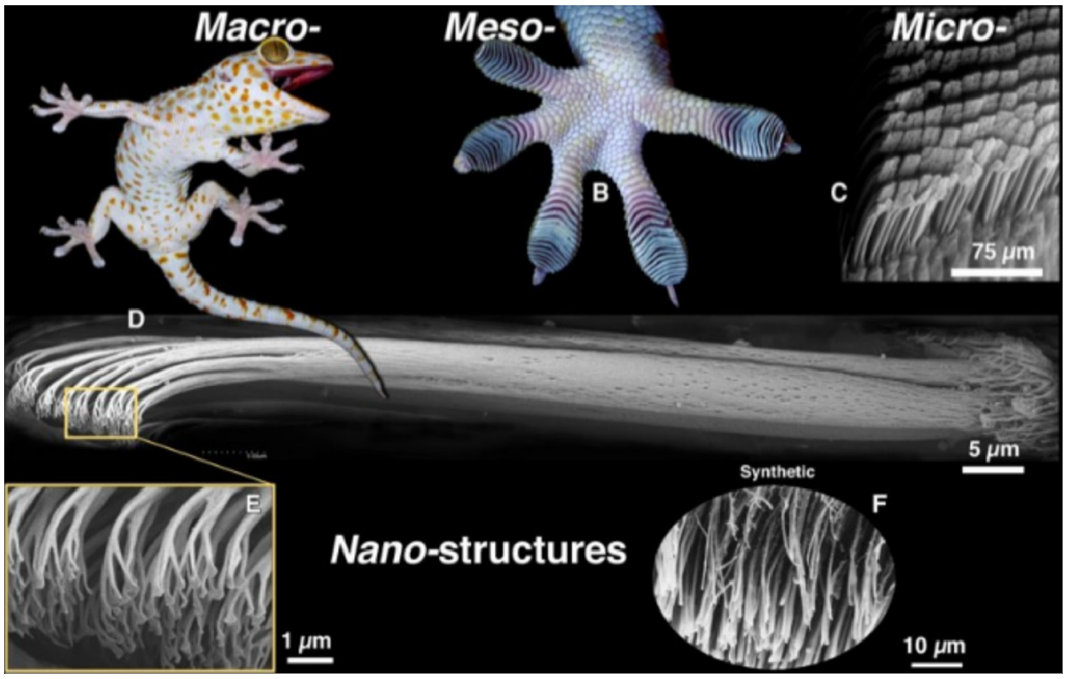

Figure 1.1: Hierarchical adhesion system of the gecko. The gecko has fine lamellae on his toes (b), which consist of thousands of setae (c, d). These setae branch up into very fine tips, called spatulae (e). The picture is taken from [35] with kind permission of K. Autumn.

Since the discovery of these surface structures, scientists have modified old theories or developed new ones to describe the adhesion properties of hairy attachment systems. While theories like the "contact splitting principle" or the "splitting efficiency of tip geometries" [19] were experimentally confirmed [36-37], there is still a huge field of poorly investigated parameters, for example the effect of roughness on adhesion or anisotropic behavior of non symmetric pillars. Another serious problem within the scientific community of gecko adhesives is the lack of comparability due to different measurement set-ups. Different

experimental methods for acquiring adhesion data complicate or even hinder a better understanding of bioinspired adhesion.

But the scientific race does not end with theory or scientific experiments: new fabrication methods for highly adhesive surfaces with self-cleaning properties and easy detachability are being developed. While scientific fabrication methods for well defined pillars are getting more complex, new fabrication approaches with regard to large-scale production are under development, as the industrial interest in gecko-like adhesives is growing steadily. To close in on a commercially available artificial gecko adhesive, much basic research has still to be done to ensure a better understanding of the principles of gecko-inspired adhesion systems.

The goal of the present work is the investigation of effects which are directly related to the probe used for adhesion measurements. For this, a new adhesion measurement system is developed, which allows precise and reproducible evaluation of adhesive properties of patterned surfaces. With this set-up, measurements are performed to investigate for example the influence of probe geometry, angle dependent adhesion and repeated adhesion measurements. To fabricate model surfaces, a new fabrication method for bioinspired adhesives is developed, which allows to control the three dimensional geometry of adhesive surfaces.

This thesis is built up as follows: In Chapter 2, a literature overview is given. Fabrication methods for fibrillar adhesion systems, adhesion measurement techniques and new developments in contact mechanics will be discussed. Chapters 3 and 4 contain preparation details for the fabrication of bioinspired adhesion systems and the experimental set-up for adhesion testing, respectively. Chapters 5 to 7 will discuss various effects such as repeated

contact experiments, comparison of different probe geometries and the influence of pillar geometry on angle dependent adhesion. In Chapter 8 the thesis will be summarized. All chapters are written as stand alone chapters and can be read without knowledge of the previous chapters.

Parts of Chapter 2 were published in the review *Functional Adhesive Surfaces with "Gecko Effect": The Concept of Contact Splitting,* Kamperman, M.; Kroner, E.; del Campo, A.; McMeeking, R. M.; Arzt, E. *Adv. Eng. Mater.* **2010**, *12*, 335-348. Chapter 5 was published in the article *Adhesion Characteristics of PDMS Surfaces During Repeated Pull-Off Force Measurements*, Kroner, E.; Maboudian, R.; Arzt, E. *Adv. Eng. Mater.* **2010**, *12 (5)*, 398-404. Chapter 6 was accepted for publication in The Journal of Adhesion: *Adhesion of Flat and Structured PDMS Samples to Spherical and Flat Probes: A Comparative Study*, Kroner, E.; Paretkar, D. R.; McMeeking, R. M.; Arzt, E.

1.1 Definitions

To avoid misunderstandings some definitions are given, which clarify the use of some terms throughout the thesis:

Adhesion – The term adhesion is almost always used as soon as two different objects are brought into contact and attractive forces appear. However, it must be clearly differentiated between the direction of applied and measured forces as well as the location at which failure or detachment occurs. In the following the term "adhesion" will be used for displacement and force measurements normal to the sample surface and detachment occurs along the interface (no bulk fracture or similar). If necessary, "adhesion" will be described as "normal adhesion" or "frictional adhesion", but will always be distinguished from friction (displacement and

forces measured parallel to the sample surface). Note that although forces are macroscopically measured perpendicular to a surface, local forces may have deviating directions, e.g. friction forces during the detachment phase.

Alignment – While in literature the issue of alignment is often circumvented by measuring the adhesion with a spherical probe, the alignment of a flat probe is crucial. Though it is possible to align sample and probe very well, it is nearly impossible to achieve perfect alignment due to possible curvatures of the sample, the probe, and due to limited accuracy of the experimental setup. In this thesis sample and probe will be described as aligned if alignment is optimized within the experimental possibilities of ± 0.02° unless stated otherwise. This "parallel" alignment is the base for tilted measurements and will be described with a misalignment angle of 0.0° without indication of the error.

Cleaning – To ensure repeatability of experiments, a stable measurement system is necessary. Even slight changes in the system can cause deviating results. As the adhesion between two objects depends strongly on surface properties, the surface state needs to be carefully controlled. There are possibilities to clean a probe or a sample objectively, e.g. plasma treatment or etching in acids. However, reproducible cleaning of probes is very time consuming and cleaning of samples (especially polymers) will influence their mechanical properties. Probes and samples will be described as "clean" after a thorough cleaning process, although it cannot be guaranteed that all residues will be removed.

Contamination – Adhesion as defined above is a phenomenon based on surface interactions. As the experiments cannot be performed in ultra clean conditions, it is unavoidable that foreign particles will be present on the relevant surfaces. Furthermore, adsorbed atoms and

molecules will change the surface properties, influencing the determined adhesion. Throughout the thesis the term "contamination" will be used only for material transfer from sample to probe or vice versa, independent of the transferred material, but not for residues or impurities such as dust particles.

Error bars – The experimental error in force values measured by the adhesion tester is included in the symbol size.

Flat – In the following chapters, the term "flat" will describe geometries with very low or no measureable curvature and low roughness. Values for curvature or roughness will be provided whenever possible. The waviness of samples is generally low and will be neglected.

Pattern and pillar – A pattern is defined as a macroscopic array of pillars, while the term pillar will be used for single geometric bodies.

Preload and pull-off force – The preload is the maximum applied compressive force value and the pull-off force the maximum tensile force value in the force displacement curves obtained by adhesion measurements.

Sample, probe and template – In this thesis, a sample is defined as a flat or patterned polymeric material on which adhesion tests are performed. A probe (often called indenter or substrate in literature) is a material with a high Young's Modulus and a specific geometry against which the adhesion is measured. A template is a patterned surface on which a liquid polymer is poured and cross-linked to achieve a patterned sample or another template.

Work of separation – If two surfaces are brought into contact and forces are needed for separation, work is done. This work is often called work of adhesion. However, besides work of adhesion other types of work may be done within the measured work, e.g. thermal work. Here, the term work of separation will be generally used and only be specified if necessary.

1.2 References

[1] Waite, J. H. *Comp. Biochem. Physiol., Part B* **1990**, *97*, 19.

[2] Yu, M.; Hwang, J.; Deming, T. J. *J. Am. Chem. Soc.* **1999**, *121*, 5825.

[3] Yu, M.; Deming, T. J. *Macromolecules* **1998**, *31*, 4739.

[4] Barnes, W. J. P. *Tire Technol. Int.* **1999**, 42–47.

[5] Barnes, W. J. P.; Smith, J.; Oines, C.; Mundl, R. *Tire Technol. Int.* **2002**, 56–60.

[6] Beutel, R. G.; Gorb, S. N. *J. Zool. Syst. Evol. Res.* **2001**, *39*, 177–207.

[7] Emerson, S. B.; Diehl, D. *Biol. J. Linn. Soc.* **1980**, *13*, 199–216.

[8] Ernst, V. V. *Tissue Cell* **1973**, *5*, 83–96.

[9] Ernst, V. V. *Tissue Cell* **1973**, *5*, 97–104.

[10] Hanna, G.; Barnes, W. J. P. *J. Exp. Biol.* **1991**, *155*, 103–125.

[11] Gorb, S.; Jiao, Y.; Scherge, M. *J. Comp. Physiol. A* **2000**, *186*, 821–831.

[12] Green, D. M. *Copeia* **1981**, 790–796.

[13] Nachtigall, W. *Biological mechanisms of attachment.* New York: Springer **1974**.

[14] Scherge, M.; Gorb, S. N. *Biological micro- and nanotribology: nature's solutions.* Berlin: Springer **2001**.

[15] Autumn, K.; Liang, Y. A.; Hsieh, S. T.; Zesch, W.; Chan, W. P.; Kenny, T. W.; Fearing, R.; Full, R. J. *Nature* **2000**, *405*, 681-685.

[16] Autumn, K.; Sitti, M.; Liang, Y. C. A.; Peattie, A. M.; Hansen, W. R.; Sponberg, S.; Kenny, T. W.; Fearing, R.; Israelachivili, J. N.; Full, R. J. *Proc. Natl. Acad. Sci. USA* **2002**, *99*, 12252-12256.

[17] Autumn, K.; Peattie, A. M., *Integr. Comp. Biol*. **2002**, *42*, 1081-1090.

[18] Huber, G.; Mantz, H.; Spolenak, R.; Mecke, K.; Jacobs, K.; Gorb, S. N.; Arzt, E., *Proc. Natl. Acad. Sci. USA* **2002**, *102*, 16293-16296.

[19] Spolenak, R.; Gorb, S.; Gao, H. J.; Arzt, E. *Proc. R. Soc. London, Ser. A* **2004**, *461*, 305-318.

[20] Hiller, U. *Z. Morphol. Tiere* **1968**, *62***,** 307-362.

[21] Hiller, U.; Blaschke, R. *Naturwissenschaften* **1967**, *54***,** 344-345.

[22] Irschick, D.J. *Biol. J. Linnaean Soc*. **1996**, *59*, 21.

[23] Maderson, P.F.A. *Nature* **1964**, *203*, 780.

[24] Peterson, J.A.; Williams, E.E. *Bull. Mus. Comp. Zool.* **1981**, *149*, 215.

[25] Roll, B. *J. Zool*. **1995**, *235*, 289.

[26] Russell, A.P. *Can. J. Zool*. **1986**, *64*, 948.

[27] Russell, A.P. *J. Morphol*. **1981**, *169*, 293.

[28] Russell, A.P. *J. Zool. London* **1975**, *176*, 437-476.

[29] Russell, A.P.; Bauer, A.M. *J. Morphol*. **1988**, *197*, 221.

[30] Russell, A.P.; Bauer, A.M. *Mem. Queensl. Mus*. **1990**, *29*, 453.

[31] Ruibal, R.; Ernst, V. *J. Morphol*. **1965**, *117*, 271-294.

[32] Schleich, H.H.; Kästle, W. *Amphibia-Reptilia* **1986**, *7*, 141.

[33] Stork, N. E. *J. Nat. Hist.* **1983**, *17***,** 829-835.

[34] Williams, E.E.; Peterson, J.A. *Science* **1982**, *215*, 1509-1511.

[35] Autumn, K.; Gravish, N. *Phil. Trans. Roy. Soc. A* **2008**, *366*, 1575-1590.

[36] del Campo, A.; Greiner, C.; Arzt, E. *Langmuir* **2007**, *23*, 10235-10243.

[37] Greiner, C.; del Campo, A.; Arzt, E. *Langmuir* **2007**, *23*, 3495-3502.

2. Literature Overview

Abstract – This chapter is organized in five parts. The first part will discuss state of the art methods for the fabrication of bioinspired adhesives. In the second part, the common measurement techniques for adhesion and friction will be reviewed, followed by a brief description of adhesion measurements on bioinspired adhesives. Then, an overview of contact mechanics principles with focus on theories for bioinspired adhesives and patterned surfaces will be given. The last part will critically comment on current issues in bioinspired adhesion, and the goal of this thesis will be defined.

Parts of this chapter are from the pre-peer reviewed version of the following article:

Functional Adhesive Surfaces with "Gecko Effect": The Concept of Contact Splitting, Kamperman, M.; Kroner, E.; del Campo, A.; McMeeking, R. M.; Arzt, E. *Adv. Eng. Mater.* **2010**, *12*, 335-348.

2.1 Fabrication of bioinspired adhesion systems

During the last few years, several fabrication methods have been applied to obtain bioinspired patterned surfaces with complex geometries. Although there are countless possibilities to pattern a surface, only few methods are suitable for the fabrication of bioinspired adhesives. This is due to the fact that several boundary conditions need to be fulfilled. For this reason, only fabrication methods suitable for designing bioinspired adhesives will be discussed here. These fabrication methods can be classified into three groups:

- template-less bottom-up patterning
- template-less top-down patterning
- patterning using a template

The first class contains the growth of patterns by adding material, e.g. growth of carbon nanotubes (CNTs). The second class contains template-less patterning by removing material such as cutting or etching. The last group containing the probably most widely used techniques is patterning using a template, e.g. molding of polymers.

2.1.1 Template-less bottom-up patterning

A promising method for the fabrication of adhesive patterns without templates is the use of CNTs. The first application of CNTs for artificial adhesives was realized by *Yurdumakan et al.* [1] and *Zhao et al.* [2]. They grew multi-walled CNT patterns on silicon wafers using chemical vapor deposition techniques. Afterwards they embedded the CNT patterns in a polymer, removed the sample from the wafer and partially dissolved the polymer, thus receiving a patterned surface. In a recently published work by *Qu et al.* [3], CNT patterns with high frictional forces and relatively low normal forces were reported. This behavior allows a versatile application, as the adhesion performance is anisotropic. The CNT

fabrication for artificial attachment systems is a complicated process, but can be transferred to larger scale production. Unfortunately, the fiber length is not constant within a sample, lowering the adhesive performance. This problem needs to be solved to optimize the adhesion of CNT based attachment systems. The potential of CNTs for high friction applications has been shown more recently by *Maeno et al.* [4], where high shear strength values of 44.5 kN/m² (N/cm²) were found. However, it was necessary to apply high compressive preload, which sometimes exceeded the resulting shear forces. As CNTs usually decompose at high temperatures (>500°C), CNT based gecko inspired adhesives could be suited for high temperature applications. Other publications have shown that CNT-based adhesives can be designed on flexible tapes [5], thus increasing their field of application.

Another approach for the fabrication of adhesive patterns is the direct drawing of micro- and nanofibers [6]. The method is based on stretching polymer bumps. A hot cylinder is rolled over a pre-patterned sample, the polymer melts in the contact area, elongates and can be hardened by cooling down rapidly, resulting in hairy patterns. This fabrication method however is restricted to thermoplastic materials, which usually have a high Young's modulus. Furthermore, densely packed pillars are difficult to obtain due to fiber collapse during the drawing process. The main drawback, however, is the tip shape of these pillars. The drawing process usually results in pointed ends, which will lead to a low contact area and thus low adhesion. Further approaches for the fabrication of patterned surfaces, e.g. surface instabilities, have not shown significant adhesion.

2.1.2 Template-less top-down patterning

The easiest way to obtain patterned surfaces is by manually cutting bulk material with a razor blade [7-9]. Of course, this technique only allows patterning in the millimeter range.

Furthermore, control over geometrical parameters such as pillar shape and height is poor. A more accurate possibility to achieve fine micropillars is given by Focused Ion Beam (FIB) cutting. An ion beam is used to cut out material, and pillars down to sub micrometer dimensions with complex geometries can be produced [10-12]. FIB cutting, however, is not widely used for direct polymer patterning due to beam damage, sample heating and high fabrication cost for large patterns. Thermoplastic polymers can also be patterned using Scanning Probe Nanomachining, where a small tip is heated up above the glass transition temperature and the pattern is "written" into a bulk sample. Several writing tips can be mounted in parallel to speed up the process [13-14].

A more successful method for micro patterning is selective cross-linking of a polymer, using different irradiation sources, such as electron, ion or laser beams. The exposed polymer layer can then be developed, removing the soluble part of the polymer and resulting in a patterned surface. The simplest way to fabricate a patterned surface by selective cross-linking is irradiation of a thin polymer film with a laser beam, where a resolution down to 1 μm was achieved [15]. To improve the resolution, special polymers were developed which react only by excitation with two photons (Two Photon Lithography) [16]. This technique allows high resolution patterning with feature sizes of 150 nm and below [17-22]. To increase the resolution even further, electron beams can be used to directly pattern a polymer layer, allowing a resolution down to 10 nm and complex surface geometries [23-25]. However, the penetration depth of electrons is limited and does not allow fabrication of high aspect ratio (AR) features. *Geim et al.* [26] used electron beam lithography to fabricate aluminum discs on top of a polyimide film and then transferred the pattern into the polyimide using reactive ion etching (RIE). A scanning probe microscope can also be taken as electron source and successful fabrication of vertical lines with a width of 20 nm and AR of 10 were reported

[27]. As the penetration depth is higher for ions than for electrons, ion beam lithography is more suitable for fabrication of high AR features, and the resolution still allows fabrication of features smaller than 1 µm [28-31]. After hardening of the exposed polymer, a new layer may be deposited and the whole process can be repeated, which allows fabrication of hierarchical geometries. Although all these techniques allow fabrication of pillars with well defined geometry, they have a main drawback: as the processes are serial, only small areas can be patterned. This results in high cost for sample fabrication.

A recent approach in template-less structuring is the oxygen plasma treatment of polymer foils. After treatment, a hairy pattern is formed [32]. The mechanism of pattern formation is not yet completely understood and hard to control. Moreover, the adhesion values are negligible, though increased friction forces are expected.

2.1.3 Patterning using templates

To overcome long sample preparation and high cost, molding and imprinting techniques are applied to fabricate patterned templates. Several samples can then be produced from a single template [33-84]. The difference between molding and imprinting is visualized in Figure 2.1.

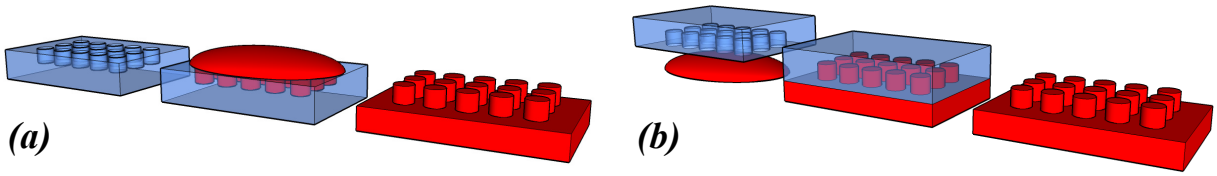

Figure 2.1: Principle of molding and imprinting. For molding, a liquid polymer is poured onto a template, hardened and removed afterwards (a). For imprinting, a template is pressed into a liquid or a heated thermoplastic polymer (b). After cross-linking a patterned sample can be demolded.

In principle, numerous patterning methods allow the fabrication of templates. However, there are three major restrictions:

- Template and sample material must be chosen to avoid high adhesive forces during the demolding process, which could lead to defects in the sample pattern. In the worst case, the sample material reacts with the template creating a chemical bond. Thus, it will be impossible to demold the sample from the template (Figure 2.2a). A surface treatment of the template before molding, such as coverage with a fluorosilane, may be necessary [85-87].
- The correct viscosity, wetting properties and air permeability of the liquid sample material must be chosen to allow complete filling of the cavities. Otherwise the template pattern will not be filled completely, resulting in pillars with lower AR and poorly controlled geometry (Figure 2.2b).
- Depending on the template geometry, the material must be deformable enough to allow the pillars to squeeze through the openings of the template. If the material is too stiff, the pillars will tear off during demolding (Figure 2.2c).

Porous membranes, such as anodic alumina, can be taken to mold patterned surfaces [55,69,88-95]. These templates result in high AR patterns with high packing density. However, the templates must be dissolved by a wet etching process after molding. This process can cause fiber collapse, as capillary forces between the pillars due to the liquid etching agent result in additional bending of the pillars. Further, the tip geometry of the pillars is not controllable and requires additional process steps. A large variety of processes were developed to control tip geometry or fabricate hierarchical geometries [26,37,40,42-45,47-49,53-54,56,58-60,62-63,66,70-72,75-76,79,82]. Some modification possibilities are schematically shown in Figure 2.3. Other modifications such as using semiconductor structuring techniques based on sacrificial layers were reported [96-98].

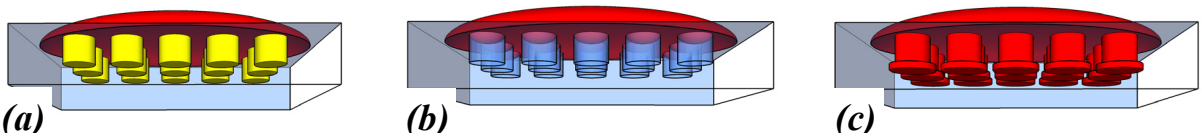

Figure 2.2: Restrictions for molding. Demolding is not possible if adhesion and friction between sample and template material are too high (a). De-wetting materials or materials with low air permeability will not fill the cavities of the template (b). If the sample is not deformable enough to squeeze through the openings of the template, the pillars will be damaged during demolding (c).

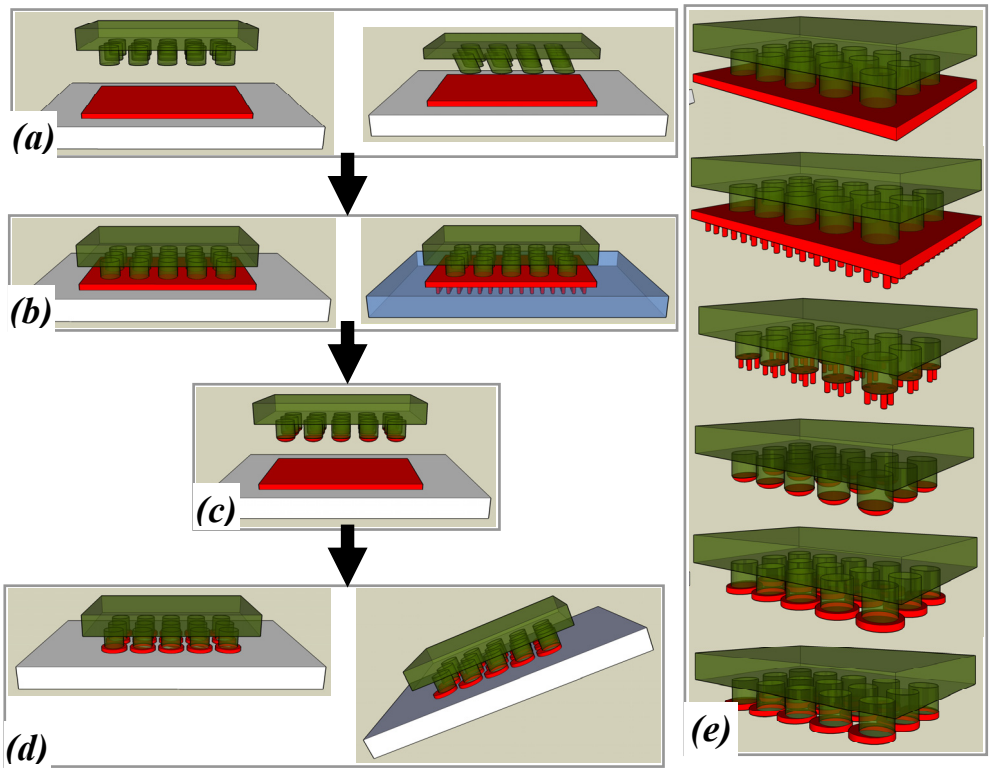

Figure 2.3: Possible modification of patterned samples (based on [44]). Straight or tilted pillars can be used for modification (a). A thin polymer layer is spin-coated onto a flat or patterned template and the sample is dipped into the polymer (b). After removing the sample, polymer droplets will stick to the pillars, forming spherical tips (c). By pressing the sample onto a flat or patterned template, the spherical droplets are deformed into mushroom or spatula shaped tips for horizontal or tilted templates (d). Resulting patterns at a certain point of the process are shown in (e).

2.2 Adhesion measurement techniques

Adhesive properties are investigated using a variety of testing methods. Generally, adhesion and friction experiments may be classified by the direction of the force measurement and the displacement direction during the experiment with respect to the sample surface (Figure 2.4). A defined preload is applied perpendicular to the sample surface. The sample is then moved, measuring force and displacement. For a shear or friction experiment, the force is measured perpendicular to the preload [2-4,69,80,99-107] (Figure 2.4a), while for normal adhesion experiments, forces are measured parallel to the preload [1-2,9,26,33,36,39,43-44,46-47,51,55 ,59,70,74,79,81,89,95,97-98,108-115] (Figure 2.4b). For a peel-test, the sample is peeled off from one end of the probe at a defined angle [8,64,99,109,116-117] (Figure 2.4c). Normal forces can be detected using weight balances [2,89] or load cells [1,33,46], by cantilever deflection of Atomic Force Microscopes (AFM) or AFM-like devices [9,26,36,44,47,55,70, 74,97,112,114-115], by surface-probe microscopes [26,36,51,55,59,95,97], or with nano-indentation set-ups [79,110-111].

Since geckos are known to increase adhesion upon shearing [118-119], modified measurement set-ups were proposed for bioinspired adhesives, combining the adhesion measurement classes described above. Such tests include, for example, shearing the sample while measuring the normal force [71,80,102,106,120]. Each system can then be extended by additional parameter controls, e.g. *in situ* contact area visualization, controlled environmental data (temperature, air pressure, relative humidity) and others. Although experiments can be macroscopically separated into normal, shear or peel tests, the acquired forces do not necessarily reflect the same mechanism on the micro- or nanoscopic length scale. This necessitates a careful evaluation of the measurement system as well as the obtained data.

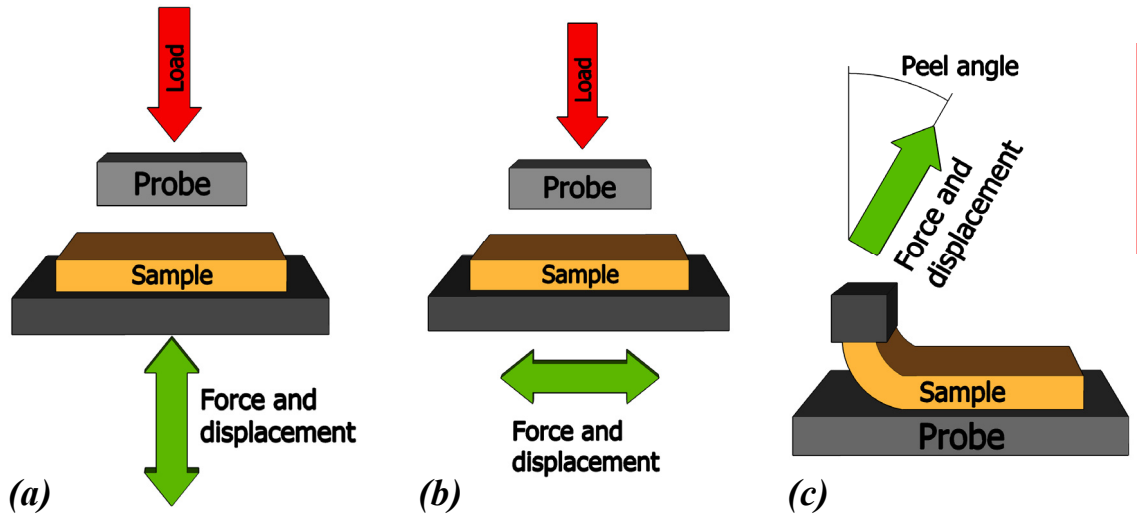

Figure 2.4: Classification of measurements. Measurements for determining adhesive properties may be classified as normal force measurements (a), shear force measurements (b) and peel tests (c). By combination of these classes, other adhesive properties, e.g. frictional adhesion (combination of (a) and (b)) are accessible.

Force values obtained by different adhesion experiments are not directly comparable, as they depend on the contact area and thus on the probe geometry. For spherical probes it was shown that the pull-off force of patterned surfaces strongly increases with the applied compressive preload until a plateau is reached [39,51,58,81]. The force values obtained by measurements with spherical probes are usually normalized by the contact area resulting in the contact strength [1-2,7,33,96,109]. The contact area depends on the indentation depth of the probe into the sample, and thus on the applied compressive preload. In addition, the contact area is continuously changing during the measurement due to the curvature of the spherical probe. This necessitates *in situ* visualization or calculation of the contact area using the displacement data of the measurement curve [9,33,39,46-47,81,108,110]. For patterned surfaces the change in contact area during the detachment phase is even more crucial as either single pillars or groups of pillars loose contact, leading to a stepwise detachment and thus to significant scatter in the force values [39].

To overcome the issue of changing contact area and inhomogeneous strain in the pillars, adhesion experiments with flat probes were performed [48,53,121-122]. Experiments did not show any dependence of the pull-off force on preload, which is expected from the Johnson-Kendall-Roberts theory (JKR; see below). However, normal adhesion experiments with flat probe geometry require careful alignment of sample and probe, as the tilting angle between probe and sample will most certainly influence the pull-off force.

Unfortunately, adhesion measurements as reported in literature do not provide all necessary data to gain a deeper understanding in adhesion of patterned surfaces. Thus, complementary experiments are necessary, but a standardized adhesion test protocol is not yet available. Furthermore, some literature often provides only poor description of the measurement set-up and experimental details, which complicates data comparison obtained by other researchers. This clearly shows that there is a gap in knowledge on the field of data acquisition as well as of data analysis, which has to be filled to ensure reliable and reproducible data.

2.3 Adhesion measurements on bioinspired adhesives

Detailed adhesion measurements were performed to evaluate the performance of bioinspired attachment systems. In 2003, measurements on high AR polyimide pillars with low packing density and poorly defined tips showed that the pull-off force strongly increases with decreasing pillar spacing. The pillar diameter and height did not seem to strongly influence the pull-off force [26]. *Crosby et al.* [39] mentioned later that the adhesive properties of cylindrical polydimethylsiloxane (PDMS) patterns fabricated by molding show three regions of pull-off force evolution. Up to ~ 70 μm pillar diameter, the pull-off force decreases with increasing pillar radius, then increases between ~ 70 μm and ~ 160 μm pillar diameter, and again decreases for pillars with radii above 160 μm. These controversial results were clarified

by a systematic study on the influence of geometric parameters on adhesion by *Greiner et al.* [51] in 2007. They fabricated well defined PDMS pillar arrays with cylindrical geometry and different radii and heights and showed that the pull-off strength increases with decreasing pillar radius, while decreasing AR results in decreasing pull-off strength.

Meanwhile, patterns with more complex geometries, designed more closely to natural attachment systems, were fabricated and tested. *Gorb et al.* [48] and *Kim et al.* [58] were the first to test patterns with mushroom-shaped tips. Compared to flat control samples, they found a 2.5-fold and a threefold pull-off force enhancement for polyvinylsiloxane pillars with approximately 15 μm radius and dumbbell shaped polyurethane (PU) pillars of 2.25 μm radius, 4.5 μm tip diameter and 20 μm height, respectively. Again, a more systematic study by *del Campo et al.* [44] compared different tip shapes and investigated their influence on the adhesive performance. They found that the tip shape has a strong influence on the adhesive performance. While PDMS cylinders with sharp and rounded edges, suction cups and spherical tips showed low pull-off forces, usually below the values for flat control samples, spatula and mushroom shaped tips exceeded the pull-off force value for flat PDMS by a factor of ~ 20 and ~ 30, respectively.

Since these studies, several modified and complex geometries were tested to optimize the adhesive properties, ranging from tilted pillars [33,70-71] over sub-surface patterns [47,60,77] and hierarchical geometries [49,53,66,72] to pillars with modified surface chemistry [65,68]. However, in these studies no noticeable enhancement in adhesion performance was found compared to the values in the study of *del Campo et al.* [44].

2.4 Contact mechanics

Attractive forces between two solids were already mentioned by Sir Isaac Newton. In his book "Opticks", published in 1704, he described his observations during experiments with glass lenses. Newton brought two glass lenses into contact and noticed a "clink" sound during separation of the lenses. As a comment to this observation he wrote: "*...The attractions of Gravity, Magnetism, and Electricity, reach to very sensible distances, and so have been observed by vulgar Eyes, and there may be others which reach to so small distances as hitherto escape Observation ; ...*" However, between the first mention of attractive forces between two solids and the beginning of closer investigation of contact mechanics nearly 180 years passed.

2.4.1 Spherical contacts

Hertz theory – In 1881, the graduate student *Heinrich Hertz* developed the first contact theory for two elastic solid spheres during his Christmas holidays. He assumed two elastic bodies during compression with a defined force and calculated the contact radius, the penetration depth and the stress distribution, assuming a frictionless, adhesion-free contact [123]. A schematic for spherical bodies is shown in Figure 2.5. The theory is based on the assumption of small contact area (described by the contact radius a) compared to the complete surface of the spheres – defined by their radii R_1 and R_2. A preload P causes a radius a of the contact area, described by the following equations:

$$a^3 = \frac{PR}{K} \qquad (2.1),$$

$$P = \frac{a^3 K}{R} \qquad (2.2).$$

R is the effective radius of the spheres, K the reduced stiffness and E^* the reduced Young's modulus, all defined as:

$$\frac{1}{R} = \frac{1}{R_1} + \frac{1}{R_2} \tag{2.3},$$

$$\frac{1}{K} = \frac{3}{4}\left(\frac{1-\nu_1^2}{E_1} + \frac{1-\nu_2^2}{E_2}\right) = \frac{3}{4}\frac{1}{E^*} \tag{2.4}.$$

E_1, E_2, υ_1 and υ_2 are the Young's moduli and Poisson's ratios of the spheres *1* and *2*, respectively.

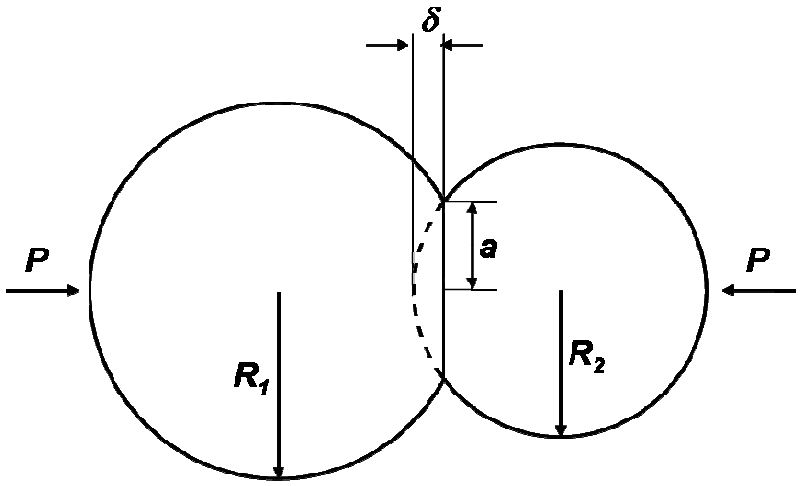

Figure 2.5: Schematic of a contact experiment based on the Hertz theory. The spheres with radii R_1 *and* R_2 *are compressed by a force* P *resulting in a contact area with radius* a*, and an indentation depth* δ*.*

The Hertz theory has been extended to include different contact shapes such as cylinders and flat punches. A variety of different contact shapes can be found in [124]. However, this theory assumes the elastic behavior of two frictionless solid objects only. Further, the Hertzian analysis describes a situation, where only compressive stresses can exist within the contact area. As attractive forces usually result in tensile stresses, this analysis cannot be applied to

adhesive contacts. Based on the work of Hertz, many modified theories were postulated, amongst which the Johnson-Kendall-Roberts (JKR) and the Derjaguin-Muller-Toporov (DMT) theories are the most famous ones and have been the basis of further, more specialized contact theories.

Johnson-Kendall-Roberts theory – Some experiments in the late 1960´s [125-126] gave evidence that the actual contact area for very soft elastic materials was considerably larger than expected from the Hertz theory. Furthermore, even without the external load *P* a contact area was visible and the elastic objects could only be separated by applying an external force.

These discrepancies to the Hertz theory led to a new theory, which soon became the most cited contact theory with regard to contact between soft elastic objects, the *Johnson-Kendall-Roberts* theory, widely known as JKR theory [127]. The theory published in 1971 starts with the Hertz theory described above but considers attractive forces based on the surface energy within the contact area. The results of this theory are obtained by balancing elastic, potential and surface energy. This energy balance leads to an additional deformation, causing a larger contact area and a remnant force after unloading the elastic objects. The JKR theory predicts the contact radius *a* under fixed load conditions as:

$$a^3 = \frac{PR}{K} + \frac{PR}{K}\left[\frac{3\pi\omega R}{P} + \sqrt{2\frac{3\pi\omega R}{P} + \left(\frac{3\pi\omega R}{P}\right)^2}\right] \qquad (2.5),$$

where ω describes the work of adhesion, which is defined as:

$$\omega = \gamma_1 + \gamma_2 - \gamma_{12} \qquad (2.6).$$

γ_1 and γ_2 are the respective surface energies, while γ_{12} is the interfacial energy for the two materials in contact. Note that Equation (2.5) can be interpreted as a sum of a Hertzian term and a JKR addition.

These considerations lead to the described increase in contact area as well as the residual attractive force after unloading. Consequently, a negative (tensile) force is needed to separate the spheres. This force is called pull-off force P_C and is given by:

$$P_C = -\frac{3}{2}\pi\omega R \qquad (2.7),$$

in the JKR theory. If attractive interactions are neglected, the value for γ is 0 and the JKR solution equals the results of the Hertz theory.

The JKR theory has been confirmed by many experimental data. However, it is designed only for soft materials with high attractive interactions. *Maugis et al.* [128] showed in 1976 that the JKR theory is consistent with linear elastic fracture mechanics if the edge of a contact is treated as a crack front. The equilibrium point, where the "crack" neither advances nor recedes is found when the strain energy release rate G equals the work of adhesion ω. This means that the adhesion force limits the stability of the system. In the case of $\omega = 0$, the JKR theory again reduces to the Hertz theory.

Derjaguin-Muller-Toporov theory – As the JKR theory is limited to materials with low Young´s moduli and high attractive interactions, a complementary theory is needed for hard materials and lower attractive interactions. *Derjaguin*, *Muller* and *Toporov* developed a theory which is based on the Hertzian deformation profile, but considers attractive van der

Waals forces outside the contact area [129]. This so called DMT theory results in the following values for contact radius a and pull-off force P_C:

$$a^3 = \frac{RP}{K} + \frac{2\pi\gamma R^2}{K} \qquad (2.8),$$

$$P_C = -2\pi\gamma R \qquad (2.9).$$

Note that the contact area can again be considered as a sum of the Hertzian term and a DMT addition.

JKR-DMT transition – As the JKR theory is an extreme case of contact mechanics for soft materials with high energy of adhesion and the DMT theory was developed to describe hard materials with low energy of adhesion, there should be a transition between both theories for intermediate values of Young´s modulus and adhesion energies. This proposal made by *David Tabor* leads to the dimensionless so-called Tabor parameter [130], which is defined as:

$$\mu = \left(\frac{R\gamma^2}{E^{*2} z_0^3} \right)^{1/3} \qquad (2.10),$$

where z_0 is the equilibrium separation distance of two surfaces and usually lies within 0.3 and 0.5 nm. The transition between the two theories occurs within the interval of 0.1 and 5 for μ, while values bigger than 5 can be treated using the JKR theory and values below 0.1 are well described by the DMT theory. For example, a spherical glass probe with R_1 = 2 mm, ν_1 = 0.3 and E_1 = 100 GPa and a flat silicone sample with $R_2 \rightarrow \infty$ (flat), ν_2 = 0.5 and E_2 = 4 MPa would result in a value of $\mu \approx 1286$, if γ = 0.044 J/m² and z_0 = 0.4 nm. This value lies clearly within the JKR regime.

Comparison of Hertz, JKR and DMT theories – Figure 2.6 graphically shows the differences between the Hertz, DMT and JKR theories. The Hertz theory results in a repulsive force profile with a maximum below the center of the sphere and an approach to zero towards the border of the contact area (Fig. 2.6a). In the DMT theory, the forces within the contact area are considered to be identical to the Hertz theory. Outside the contact area attractive van der Waals interactions are taken into account, which decrease with increasing distance from the border of the contact area (Fig. 2.6b). The JKR theory considers attractive forces within the contact area, which cause an additional deformation of sample and probe, resulting in an increased contact area compared to Hertz theory. This, however, results in repulsive forces towards the border of the contact area (Fig. 2.6c). If equations (2.1), (2.5) and (2.8) are compared, it is obvious that the JKR addition to the Hertzian contact area is larger than the DMT addition, and thus $a_{Hertz} < a_{DMT} < a_{JKR}$ is valid.

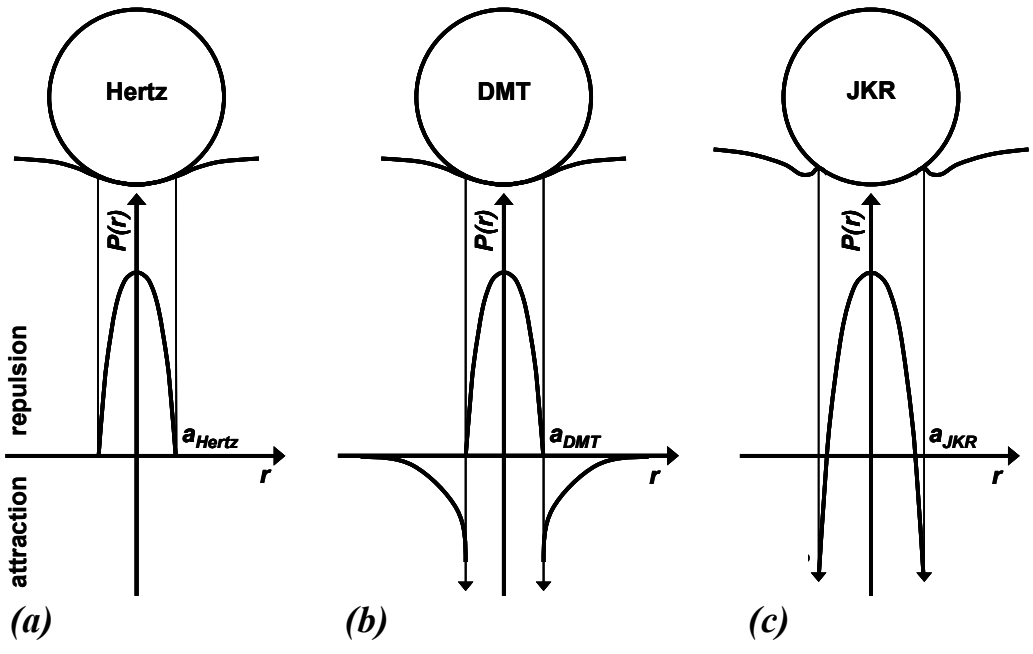

Figure 2.6: Comparison between Hertz, DMT and JKR theories. The Hertz theory results in repulsive forces throughout the contact area (a). The DMT theory assumes Hertzian behavior within the contact area and attractive forces outside the contact area (b). For the JKR theory the contact area is increased due to attractive forces within the contact area (c).

2.4.2 Flat punch contacts

Besides contact mechanics of spherical contacts, flat punch contacts were treated theoretically as well. *Kendall* solved the problem of adhesion between a rigid flat punch and an elastic half-space for the first time in 1971 by energy balancing [131]. Based on strain energy release rate calculations, he calculated the pull-off force P_c to be

$$P_c = \sqrt{6\pi a^3 K\omega} \qquad (2.11),$$

where ω is the work of adhesion and the contact area is now defined by the dimensions of the flat punch. Thus, we find a deviating proportionality of the pull-off force for different contact geometries. While $P_c \sim \omega$ for spherical contacts (JKR and DMT), we get $P_c \sim \sqrt{\omega}$ for a flat punch contact. This indicates that the adhesion does not only depend on the surface energy, but also on the probe geometry and probably other geometrical parameters like testing angle. Note further that the pull-off force is not proportional to the contact area. Thus, the size of the punch matters as well.

In 1973, *Kendall* noted that the problem of a flat punch adhering to a flat half space is similar to a deeply notched bar and thus proposed a treatment of the problem from a linear elastic fracture mechanics point of view. Based on calculations on this fracture mechanics problem [132], he calculated the pull-off force P_c to be

$$P_c = K_I 2a\sqrt{\pi a} \qquad (2.12),$$

where K_I is the stress intensity factor in *mode I* displacement [133].

2.4.3 Contacts of bioinspired surface patterns

The adhesion of a patterned surface on a flat one can be higher than the adhesion between two flat surfaces, as shown e.g. in [1,95,108]. To explain this behavior, a categorization of effects due to surface patterning was recently proposed [134]:

- It is more difficult to peel off a patterned surface, as the strain energy stored in an individual pillar is not available for the neighboring pillars for pull-off.
- A long pillar can adapt better to surface roughness, because the stored elastic energy for deformation is reduced due to additional bending modes.
- With decreasing pillar size, the surface energy (area term, increases adhesion) is increased more than the stored elastic energy (volume term, decreases adhesion).
- Pillars below a critical dimension develop a uniform stress distribution before pull-off, thereby reaching the theoretical adhesion strength.
- If the adhesion is defect controlled, large defects will lead to an easier detachment. As defects in smaller pillars are also smaller, size reduction will increase adhesion [108,136]. Further, smaller pillars are more tolerant to defects [135].

Note that there exist several attachment systems in nature, which are not based on “hairy” surface patterns, but have an extremely soft and compliant surface. These systems can adapt to surface roughness with low storage of elastic energy during deformation, and energy dissipation during pull-off is increased by viscoelastic effects. Such adhesion systems will not be discussed here.

Contact splitting principle – An important corollary of the JKR theory with regard to fibrillar attachment systems is the principle of contact splitting, introduced in 2003 by *Arzt et al.* [137]. This principle states that the pull-off force is increased by splitting up one contact into

several smaller contacts while the total contact area stays constant (Fig. 2.7a). Splitting up one contact into n contacts leads to an increase in pull-off force P_C by the factor n^s. The value of the exponent s, called "splitting efficiency", depends on the shape of the contacts. For a flat contact shape (flat punch), the exponent s equals 0.5, while hemispherical contact shapes result in a value of 1. This leads to the conclusion that a patterned attachment system becomes the more effective, the smaller the contacts are and the more contacts are present. Furthermore, the effect of contact splitting can be increased by changing the geometry of the contact. This principle has been supported experimentally, both in natural and artificial systems. In nature, animals of different species have developed hairy systems with several tip shapes, such as flat punches, spherical tips, suction cups or spatula-like shapes [138]. With increasing body mass of an animal, the density of the fibers increases while their dimensions are reduced (Fig. 2.7c). This holds true for six orders of magnitude in animal body weight [137,139]. Experiments on artificial attachment systems showed that adhesion increases with decreasing radii and that the contact shape of the pillars strongly influences the splitting efficiency [44,51]. Both findings support the contact splitting principle.

All results presented above suggest that an ideal attachment system should consist of very fine hairs, packed as densely as possible. However, there are limitations to the packing density and the fiber radii. The attractive forces are not only present between a counter surface and the attachment system, but between the single pillars as well. Very small dimensions lead to a low bending modulus of the single pillars. At a certain critical dimension the attractive forces between the pillars outweigh their elastic restoring forces. This leads to "condensation", where several pillars stick together. This formation of larger contacts is believed to cause a significant drop in adhesion force [142] (Fig. 2.7b).

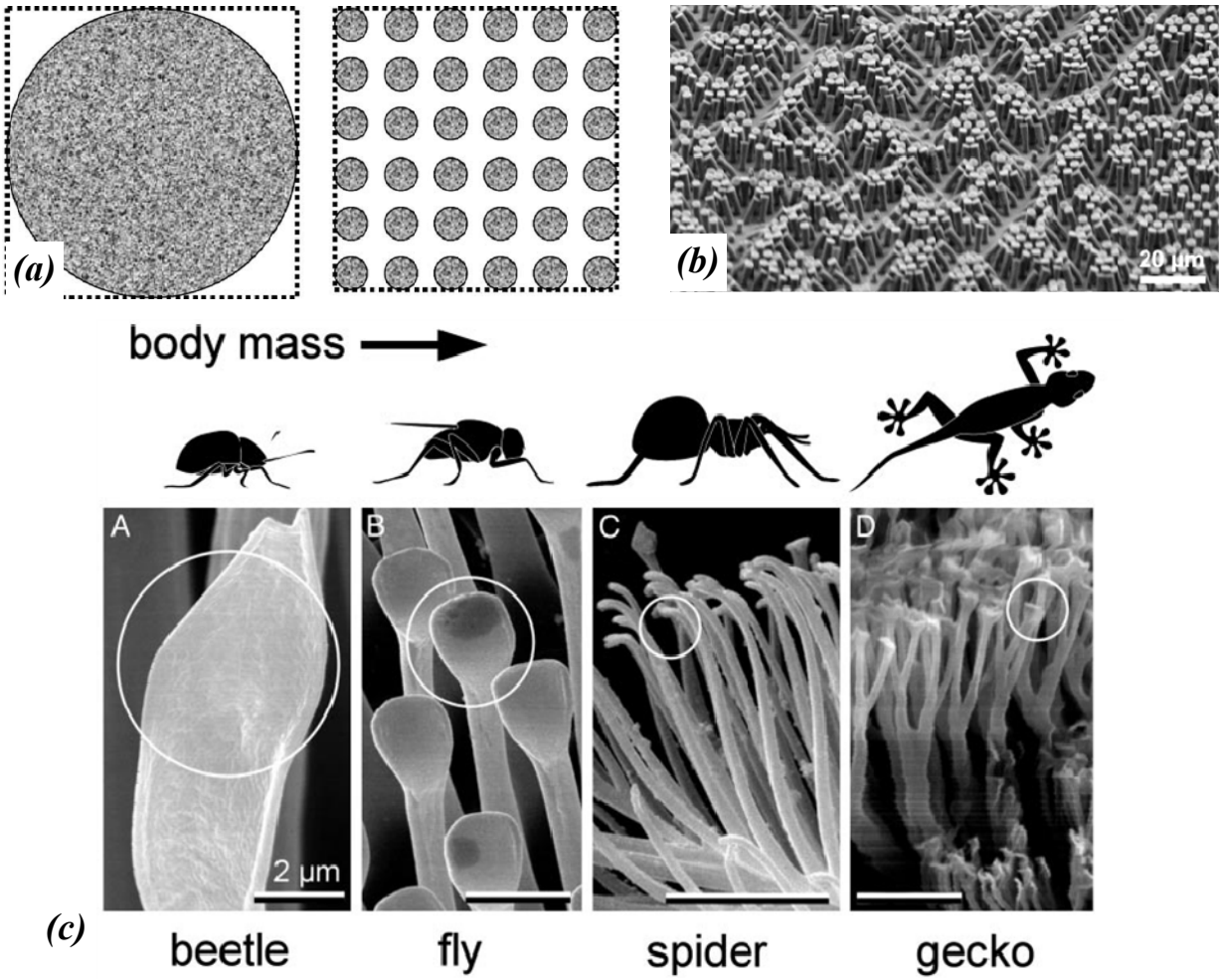

Figure 2.7: Principle of contact splitting: the adhesive force increases with the number of contacts. (a) "Condensed" artificial adhesive pillars [140] (b). The feature dimensions decrease with increasing body weight of the animal [137] (c). Pictures were taken with kind permission of E. Arzt.

Spring model for bioinspired surfaces – As patterned samples attach with multiple contacts to a probe, an obvious way to model the contact behavior is to assume the pillars as individual springs. This has been done by *Schargott et al.* [143], resulting in an increasing pull-off force with increasing preload, until a plateau is reached. The model fits qualitatively to experimental data [51]. However, it does not take into account any interactions between the springs through the backing layer of the sample. *Kim et al.* [59] provided experimental data which show a strong increase of adhesion with decreasing backing layer thickness. They

proposed a model, which explains the difference of the adhesive properties by an adhesion promotion for thin backing layer thickness due to equal load sharing. Thick backing layers, however, lead to stress concentration on the contact edges. This model considers a deformation of the backing layer, resulting in pillars which are not perpendicular to the probe surface anymore. Unfortunately, they did not consider any effects of probe geometry, which would lead to a similar problem, as schematically shown in Figure 2.8.

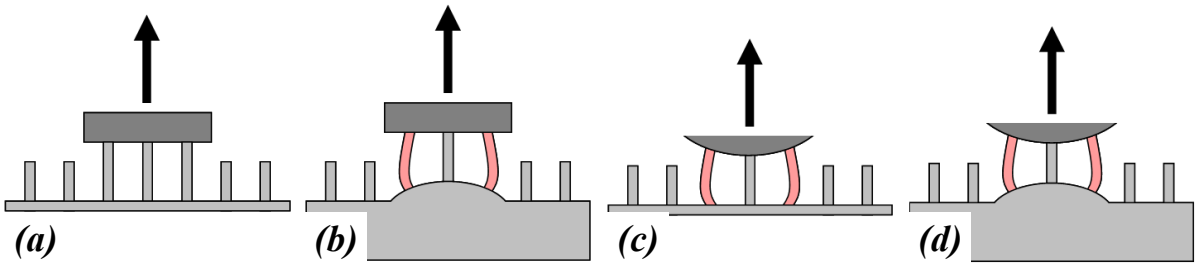

Figure 2.8: Stress concentration in pillars due to curvature. In case of a thin backing layer the stress is distributed homogeneously in the pillars (a). Deformations in thick backing layers lead to stress concentration in pillars near the periphery of the contact area (b) [59]. Similar phenomena may occur for contact with spherical probes (c,d).

Adhesion design maps – The limitations of bioinspired attachment systems have shown the need of a more specific prediction for the fabrication of "successful" adhesion systems. In order to fulfill these requirements, so-called "adhesion design maps" have been developed. The adhesion design maps introduced by *Spolenak et al.* [142] in 2005 are double logarithmic plots, where the x-axis reflects the Young´s modulus and the y-axis the fiber radius, resulting in a two dimensional space of material and pillar size. Into these charts, several limiting criteria can be plotted, for example the theoretical contact strength (the maximum strength provided by van der Waals forces), different fiber condensation criteria, the limit of fiber fracture (which occurs, if the adhesion strength for a single contact exceeds the fracture

strength of the pillar itself) or the influence of roughness on the adhesion performance. Adhesion design maps can be modified for several purposes and help design bioinspired patterns which are likely to provide high adhesion.

2.5 Discussion and aim of this thesis

Various geometries for adhesive surfaces were fabricated during the last several years and led to complex bioinspired adhesive systems. Lately, the focus of sample preparation shifted strongly to fabrication of even more complex geometries rather than understanding simple ones. The fabrication techniques have become extremely complicated, often consisting of many fabrication steps including sacrificial templates [96-98], or techniques where the pillar geometry is difficult to control like inking and printing processes [44]. Such fabrication processes result in sample geometries which are difficult to reproduce. As the geometry of the pillars greatly influence their adhesive properties [44], it is necessary to develop a fabrication method, which allows a reproducible sample fabrication with well controlled geometric parameters. Furthermore, besides few systematic studies on geometry-adhesion relationships [44,51,71], there is a gap in studying pillar geometry effects by consequently varying single parameters to identify their influence on adhesion.

Besides fabrication of bioinspired adhesion systems, the evaluation of their adhesive properties is one of the most important points in designing new dry adhesives. For adhesion measurements, spherical probes have been used for one major reason: the alignment of sample and probe is not necessary due to the geometric isotropy of the sphere. Otherwise, the problem of controlled alignment is – from the experimental point of view – difficult to solve. There are some publications where experimental set-ups with a self-alignment mechanism were used [48,122], but a self-alignment system does not provide control over the experiment

during the two most important events of the adhesion measurement: the contact formation and the detachment phase. Moreover, there is no possibility to control alignment during the adhesion measurement. To avoid a complex adhesion measurement system, it is common to use spherical probes and to choose large probe radii to approximate a flat probe. However, in some publications it can be read in between the lines that the issue of probe geometry is a troublesome one that would need a closer investigation of probe geometry effects. For example, in several publications from the research group of *M. Sitti* the spherical probe is considered as an idealized roughness with one big asperity. This clearly shows that the problems of spherical probes are known. But instead of designing a new adhesion tester to solve the problem, the *disadvantages* of spherical probes are converted into a *benefit* of a more "close to reality" testing method, as adhesion to surfaces with different roughness is an important part of bioinspired adhesives. The fact that a spherical probe has nothing to do with a rough surface (fractal, random, asperities on different length scales, etc.) stays disregarded.

Adhesion tests with spherical probes also result in several problems concerning data analysis. The most obvious problem is the change of contact area with varying preload. The determination of the pull-off force itself does not deliver any data, which allows a comparable evaluation of adhesive properties. More important is the pull-off strength (force per area), which indicates the performance of bioinspired adhesives. The consequence of adhesion tests with spherical probes is that the pull-off force does not increase in the same way as the contact area due to the indentation of the probe into the sample. This results in a decreasing pull-off strength with increasing preload [33,44,51]. In other words: the harder a sample is pressed against a surface, the lower is the adhesion – which physically makes no sense.

Besides the preload dependent contact area, the data analysis is complicated further by the inhomogeneous strain in the pillars due to the curvature of the spherical probe. Figure 2.9

schematically shows the deformation of single pillars during the retraction phase of a measurement with a spherical probe. For simplification, no deformation in the backing layer is assumed. While pillars below the center of the probe are under compression, the pillars on the contact periphery are under tension. Even if all pillars are under tension during pull-off, the tension of the pillars differs depending on their position compared to the center of the contact area. This will result in stepwise detachment, as found e.g. in [33,39,47,51,72]. To overcome these problems, measurements with a flat probe are necessary. This presupposes a measurement set-up with controllable alignment, which is not yet available.

Figure 2.9: Schematic of a spherical probe contact with a patterned surface. Pillars below the center of the probe are compressed while those near the edge of the contact area are under tension. This leads to an inhomogeneous strain for the individual pillars and causes stepwise detachment. Red indicates compressed and dark green elongated pillars.

The goal of this thesis is to gain a deeper understanding of adhesion phenomena of patterned surfaces. By comparison of different probe geometries it is possible to distinguish between "true" effects due to the patterned surface and measurement effects, which originate from the probe and thus from the chosen set-up for acquisition of adhesion data. Adhesion measurements with non-spherical probes, e.g. flat probes, require a new measurement set-up which allows contact experiments with defined probe tilt angle. Based on flat probe measurements a new data analysis approach will be possible due to the preload independent

contact area. Based on this new measurement set-up, patterned samples will be investigated with focus on probe dependent effects. For this, a new sample fabrication approach was developed, which allows the fabrication of robust, durable templates and patterned samples with well controlled geometry.

In Chapter 3 a sample fabrication process based on photo lithography and reactive ion etching is presented. Chapter 4 shows the development process of a new adhesion measurement device. The effect of repeated contact formation on adhesion will be discussed in Chapter 5. In Chapter 6, adhesion experiments on patterned surfaces using flat probes and controlled alignment will be compared to experiments using spherical probes. Chapter 7 focuses on the angle dependent adhesion and the deformation behavior of single macroscopic pillars with defined tip geometry. Finally, all chapters will be summarized in Chapter 8.

2.6 References

[1] Yurdumakan, B.; Raravikar, N. R.; Ajayan, P. M.; Dhinojwala, A. *Chem. Commun.* **2005**, 3799-3801.

[2] Zhao, Y.; Tong, T.; Delzeit, L.; Kashani, A.; Meyyappan, M.; Majumdar, A. *J. Vac. Sci. Technol. B* **2006**, *24*, 331-335.

[3] Qu, L.; Dai, L.; Stone, M.; Xia, Z.; Wang, Z. L. *Science* **2008**, *322*, 238-242.

[4] Maeno, Y.; Nakayama, Y. *Appl. Phys. Lett.* **2009**, *94*, 012103.

[5] Sethi, S.; Ge, L.; Ci, L.; Ajayan, P. M.; Dhinojwala, A. *Nano Lett.* **2008**, *8*, 822-825.

[6] Manciula, J. D. *Ph. D dissertation: Nano- and micro-structured polymer surfaces* (Fakultät für Chemie und Geowissenschaften, University of Heidelberg, Germany) **2007**.

[7] Chung, J. Y.; Chaudhury, M. K. *J. R. Soc. Interface* **2005**, *2*, 55-61.

[8] Ghatak, A.; Mahadevan, L.; Chung, J. Y.; Chaudhury, M. K.; Shenoy, V. *Proc. R. Soc. London, Ser. A* **2004**, *460*, 2725-2735.

[9] Glassmaker, N. J.; Jagota, A.; Hui, C. Y. *Acta Biomater.* **2005**, *1*, 367-375.

[10] Fu, Y.; Bryan, N. K. A. *J. Vac. Sci. Technol. B* **2005**, *23*, 984.

[11] Fujii, T.; Iwasaki, K.; Munekane, M.; Takeuchi, T.; Hasuda, M.; Asahata, T.; Kiyohara, M.; Kogure, T.; Kijima, Y.; Kaito, T. *J. Micromech. Microeng.* **2005**, *15*, 286.

[12] Vasile, M. J.; Nassar, R.; Xie, J. S. *J. Vac. Sci. Technol. B* **1998**, *16*, 2499-2505.

[13] Despont, M.; Drechsler, U.; Yu, R.; Pogge, H.; Vettiger, P. *J. Microelectromech. Syst.* **2004**, *13*, 895-910.

[14] Minne, S. C.; Manalis, S. R.; Atalar, A.; Quate, C. F. *J. Vac. Sci.Technol. B* **1996**, *14*, 2456-2461.

[15] Bertsch, A.; Lorenz, H.; Renaud, P. *Sens. Actuators, A: Phys.* **1999**, *A73*, 14.

[16] Sun, H.-B.; Kawata, S. *Ad*V. *Polym. Sci.* **2004**, *170*, 169.

[17] Houbertz, R.; Schulz, J.; Froehlich, L.; Domann, G.; Popall, M.; Serbin, J.; Chichkov, B. *Mater. Res. Soc. Symp. Proc.* **2003**, *780*, 175.

[18] Juodkazis, S.; Mizeikis, V.; Seet, K. K.; Miwa, M.; Misawa, H. *Nanotechnology* **2005**, *16*, 846.

[19] LaFratta, C. N.; Baldacchini, T.; Farrer, R. A.; Fourkas, J. T.; Teich, M. C.; Saleh, B. E. A.; Naughton, M. J. *J. Phys. Chem. B* **2004**, *108*, 11256.

[20] Pan, E. Y.; Pu, N. W.; Tong, Y. P.; Yau, H. F. *Appl. Phys. B* **2003**, *77*, 485.

[21] Teh, W. H.; Durig, U.; Salis, G.; Harbers, R.; Drechsler, U.; Mahrt, R. F.; Smith, C. G.; Guntherodt, H. J. *Appl. Phys. Lett.* **2004**, *84*, 4095.

[22] Tormen, M.; Businaro, L.; Altissimo, M.; Romanato, F.; Cabrini, S.; Perennes, F.; Proietti, R.; Sun, H.-B.; Kawata, S.; Di Fabrizio, E. *Microel. Eng.* **2004**, *73-74*, 535.

[23] Bilenberg, B.; Scholer, M.; Shi, P.; Schmidt, M. S.; Boggild, P.; Fink, M.; Schuster, C.; Reuther, F.; Gruetzner, C.; Kristensen, A. *J. Vac. Sci. Technol. B* **2006**, *24*, 1776.

[24] Elsner, H.; Meyer, H. G. *Microelectron. Eng.* **2001**, *57-58*, 291.

[25] Yamazaki, K.; Namatsu, H. *Microelectron. Eng.* **2004**, *73-74*, 85.

[26] Geim, A.K.; Dubonos, S.V.; Grigorieva, I.V.; Novoselov, K. S.; Zhukov, A. A.; Shapoval, S. Y. *Nature Mater.* **2003**, *2*, 461-463.

[27] Soh, H. T.; Guarini, K. W.; Quate, C. F. *Scanning Probe Lithography*; Kluwer Academic Publishers: New York, **2001**.

[28] Ansari, K.; van Kan, J. A.; Bettiol, A. A.; Watt, F. *Appl. Phys. Lett.* **2004**, *85*, 476.

[29] Munnik, F.; Benninger, F.; Mikhailov, S.; Bertsch, A.; Renaud, P.; Lorenz, H.; Gmur, M. *Microelectron. Eng.* **2003**, *67-68*, 96.

[30] Osipowicz, T.; van Kan, J. A.; Sum, T. C.; Sanchez, J. L.; Watt, F. *Nucl. Instrum. Methods B* **2000**, *161*, 83.

[31] van Kan, J. A.; Bettiol, A. A.; Ansari, K.; Teo, E. J.; Sum, T. C.; Watt, F. *Int. J. Nanotechnol.* **2004**, *1*, 464.

[32] Wohlfart, E. Doctoral thesis (University of Stuttgart and Max-Planck Institute for Metals Research, Stuttgart, Germany) **2009**.

[33] Aksak, B.; Murphy, M. P.; Sitti, M. *Langmuir* **2007,** *23,* 3322-3332.

[34] Burton, Z.; Bhushan, B. *Nano Lett.* **2005**, *5*, 8.

[35] Chandra, D.; Taylor, A. J.; Yang, S. *Soft Matter*, **2008**, *4*, 979–984.

[36] Cheung, E.; Sitti, M. *J. Adhes. Sci. Tech.* **2008**, *22*, 569–589.

[37] Cheung, E.; Sitti, M. *Langmuir* **2009**, *25,* 6613–6616.

[38] Cho, W. K.; Choi, I. S. *Adv. Funct. Mater.* **2008**, *18*, 1089–1096.

[39] Crosby, A. J.; Hageman, M.; Duncan, A. *Langmuir* **2005,** *21,* 11738-11743.

[40] Davies, J.; Haq, S.; Hawke, T.; Sargent, J. P. *Int. J. Adhes. Adhes.* **2009**, *29*, 380–390.

[41] Daltorio K. A.; Gorb, S.; Peressadko, A.; Horchler, A. D.; Wei, T. E.; Ritzmann, R. E.; Quinn, R. D. *MRS Bulletin* **2007**, *23*, 504-508.

[42] del Campo, A.; Álvarez, I.; Filipe, S.; Wilhelm M. *Adv. Funct. Mater.* **2007**, *17*, 3590-3597.

[43] del Campo, A.; Greiner, C.; Álvarez, I.; Arzt, E. *Adv. Mater.* **2007**, *19*, 1973–1977.

[44] del Campo, A.; Greiner, C.; Arzt, E. *Langmuir* **2007,** *23,* 10235-10243.

[45] Glass, P.; Chung, C.; Washburn, N. R.; Sitti, M. *Langmuir* **2009**, *25*, 6607–6612.

[46] Glassmaker, N. J.; Jagota, A.; Hui, C.-Y.; Kim, J. *J. R. Soc. Interface* **2004**, *1*, 23-33.

[47] Glassmaker, N. J.; Jagota, A.; Hui, C.-Y.; Noderer, W. L.; Chaudhury, M. K. *Proc. Natl. Acad. Sci. U. S. A.* **2007**, *104*, 10786.

[48] Gorb, S.; Varenberg, M.; Peressadko, A.; Tuma, J. *J. R. Soc. Interface* **2007**, *4*, 271-275.

[49] Greiner, C.; Arzt, E.; del Campo, A. *Adv. Mater.* **2009**, *21*, 479–482.

[50] Greiner, C.; Buhl, S.; del Campo, A.; Arzt, E. *J. Ahdes.* **2009**, *85*, 646-661.

[51] Greiner, C.; del Campo, A.; Arzt, E. *Langmuir* **2007,** *23,* 3495-3502.

[52] Jagota, A.; Hui, C.-Y.; Glassmaker, N.J.; Tang T. *MRS Bulletin* **2007**, *32*, 492-495.

[53] Jeong, H. E.; Lee, J.-K.; Kim, H. N.; Moon, S. H.; Suh, K. Y. *Proc. Nat. Acad. Sci.* **2009**, *106*, 5639-5644.

[54] Jeong, H. E.; Lee, S. H.; Kim, J. K.; Suh, K. Y. *Langmuir* **2006,** *22,* 1640-1645.

[55] Kim, D. S.; Lee, H. S.; Lee, J.; Kim, S.; Lee, K. H.; Moon, W.; Kwon, T. H. *Microsyst. Technol.* **2007**, *13*, 601-606.

[56] Kim, S.; Aksak, B.; Sitti, M. *Appl. Phys. Lett.* **2007**, *91*, 221913.

[57] Kim, S.; Cheung, E.; Sitti, M. *Langmuir* **2009**, *25*, 7196-7199.

[58] Kim, S.; Sitti, M. *Appl. Phys. Lett.* **2006**, *89*, 261911.

[59] Kim, S.; Sitti, M.; Hui, C.-Y.; Long, R.; Jagota, A. *Appl. Phys. Lett.* **2007**, *91*, 161905.

[60] Kim, S.; Sitti, M.; Xie, T.; Xiao, X. *Soft Matter*, **2009**, *5*, 3689–3693.

[61] Kim, T.-I.; Pang, C.; Suh, K. Y. *Langmuir* **2009**, *25*, 8879-8882.

[62] Kim, T.; Jeong, H. E.; Suh, K. Y.; Lee, H. H. *Adv. Mater.* **2009**, *21*, 2276–2281.

[63] Kustandi, T. S.; Samper, V. D.; Ng, W. S.; Chong, A. S.; Gao, H. *J. Micromech. Microeng.* **2007**, *17*, 75–81.

[64] Lamblet,, M.; Verneuil, E.; Vilmin, T.; Buguin, A.; Silberzan, P.; Léger, L. *Langmuir* **2007,** *23,* 6966-6974.

[65] Lee, H.; Lee, B. P.; Messersmith, P. B. *Nature* **2007**, *448*, 19.

[66] Lee, J.; Bush, B.; Maboudian, R.; Fearing, R. S. *Langmuir* **2009**, *25*, 12449–12453.

[67] Lee, J.; Fearing, R. S. *Langmuir* **2008,** *24,* 10587-10591.

[68] Mahdavi, A.; Ferreira, L.; Sundback, C.; Nichol, J. W.; Chan, E. P.; Carter, D. J. D.; Bettinger, C. J.; Patanavanich, S.; Chignozha, L.; Ben-Joseph, E.; Galakatos, A.; Pryor, H.; Pomerantseva, I.; Masiakos, P. T.; Faquin, W.; Zumbuehl, A.; Hong, S.; Borenstein, J.; Vacanti, J.; Langer, R.; Karp, J. M. *Proc. Nat. Acad. Sci.* **2008**, *105*, 2307-2312.

[69] Majidi, C.; Groff, R. E.; Maeno, Y.; Schubert, B.; Baek, S.; Bush, B.; Maboudian, R.; Gravish, N.; Wilkinson, M.; Autumn, K.; Fearing, R. S. *Phys. Rev. Lett.* **2006**, *97*, 076103.

[70] Murphy, M. P.; Aksak, B.; Sitti, M. *J. Adhes. Sci. Technol.* **2007***, 21,* 1281–1296.

[71] Murphy, M. P.; Aksak, B.; Sitti, M. *small* **2009**, *5*, 170–175.

[72] Murphy, M. P.; Kim, S.; Sitti, M. *Appl. Mater. Interface* **2009**, *1*, 489-855.

[73] Parness, A.; Soto, D.; Esparza, N.; Gravish, N.; Wilkinson, M.; Autumn, K.; Cutkosky, M. *J. Roy. Soc. Interface* **2009**, *6*, 1223-1232.

[74] Peressadko, A.; Gorb, S.; *J. Adhes.* **2004**, *80*, 1–15.

[75] Pokroy, B.; Epstein, A. K.; Persson-Gulda, M. C. M.; Aizenberg, J. *Adv. Mater.* **2009**, *21*, 463–469.

[76] Pokroy, B.; Kang, S. H.; Mahadevan, L.; Aizenberg, J. *Science* **2009**, *323*, 237-240.

[77] Reddy, S.; Arzt, E.; del Campo, A. *Adv. Mater.* **2007**, *19*, 3833–3837.

[78] Sameoto, D.; Menon, C. *J. Micromech. Microeng.* **2009**, *19*, 5.

[79] Santos, D.; Spenko, M.; Parness, A.; Kim, S.; Cutkosky, M. *J. Adhes. Sci. Technol.* **2007**, *21*, 1317-1341.

[80] Schubert, B.; Majidi, C.; Groff, R. E.; Baek, S.; Bush, B.; Maboudian, R.; Fearing, R. S. *J. Adhes. Sci. Technol.* **2007**, *21*, 1297-1315.

[81] Thomas, T.; Crosby, A. J. *J. Adhes.* **2006**, *82*, 311–329.

[82] Vajpayee, S.; Long, R.; Shen, L.; Jagota, A.; Hui, C.-Y. *Langmuir*, **2009**, 25, 2765-2771.

[83] Varenberg, M.; Peressadko, A.; Gorb, S.; Arzt, E. *Appl. Phys. Lett.* **2006**, *89*, 121905.

[84] Yoon, H.; Jeong, H. E.; Kim, T.-I.; Kang, T. J.; Tahk, D.; Char, K.; Suh, K. Y. *Nano Today* **2009**, *4*, 385-392.

[85] Jung, G. Y.; Li, Z. Y.; Wu, W.; Chen, Y.; Olynick, D. L.; Wang, S. Y.; Tong, W. M.; Williams, R. S. *Langmuir* **2005**, *21*, 1158.

[86] Keil, M.; Beck, M.; Frennesson, G.; Theander, E.; Bolmsjo, E.; Montelius, L.; Heidari, B. *J. Vac. Sci. Technol. B* **2004**, *22*, 3283.

[87] Turner, R.; Desta, Y.; Kelly, K.; Zhang, J.; Geiger, E.; Cortez, S.; Mancini, D. C. *J. Micromech. Microeng.* **2003**, *13*, 367.

[88] Campolo, D.; Jones, S.; Fearing, R. S. *IEEE-NANO 2003.* (San Francisco, CA, U.S.A.) **2003**, 856-859.

[89] Jin, M. H.; Feng, X. J.; Feng, L.; Sun, T. L.; Zhai, J.; Li, T. J.; Jiang, L. *Adv. Mater.* **2005**, *17*, 1977-1981.

[90] Majidi, C.; Groff, R.; Fearing, R. *ASME Intern. Mech. Eng. Cong. & Exp.* (Anaheim, CA, U.S.A.) **2004**, 1-6.

[91] Menon, C.; Murphy, M.; Sitti, M. *IEEE Intern. Conf. on Robotics and Biomimetics (ROBIO)* (Shenyang, China) **2004**, 431-436.

[92] Shah, G. J.; Sitti, M. *IEEE Intern. Conf. on Robotics and Biomimetics (ROBIO)* (Shenyang, China) **2004**, 873-878.

[93] Sitti, M. *ASME Congress* (Washington D.C., U.S.A.) **2003**, 42787-42792.

[94] Sitti, M.; Fearing, R. S. *IEEE Intern Conf on Robotics and Automation* (Taiwan) **2003**, 1164-1170.

[95] Sitti, M.; Fearing, R. S. *J. Adhes. Sci. Technol.* **2003**, *17*, 1055-1073.

[96] Northen, M. T.; Greiner, C.; Arzt, E.; Turner, K. L. *Adv. Mater.* **2008**, *20*, 3905.

[97] Northen, M. T.; Turner, K. L. *Nanotechnology* **2005**, *16*, 1159.

[98] Northen, M. T.; Turner, K. L. *J. Sens. Actuator A-Phys.* **2006**, *130*, 583.

[99] Ge, L.; Sethi, S.; Ci, L.; Ajayan, P. M.; Dhinojwala, A.; *P. Natl. Acad. Sci. USA* **2007**, *104*, 10792.

[100] Lee, J.; Fearing, R. S.; Komvopoulos, K. *Appl. Phys. Lett.* **2008**, *93*, 191910.

[101] Lee, J.; Majidi, C.; Schubert, B.; Fearing, R. *J. Roy. Soc. Interface* **2008**, *5*, 835-844.

[102] Schubert, B.; Lee, J.; Majidi, C.; Fearing, R. *J. R. Soc. Interface* **2008**, *5*, 845.

[103] Tian, Y.; Pesika, N.; Zeng, H.; Rosenberg, K.; Zhao, B.; McGuiggan, P.; Autumn, K.; Israelachvili, J. N.; *P. Natl. Acad. Sci. U.S.A.* **2006**, *103*, 19320.

[104] Yao, H.; Della Rocca, G.; Guduru, P. R.; Gao, H.; *J. R. Soc. Interface* **2008**, *5*, 723.

[105] Zeng, H.; Pesika, N.; Tian, Y.; Zhao, B.; Chen, Y.; Tirrell, M.; Turner, K. L.; Israelachvili, J. *Langmuir* **2009**, *25*, 7486.

[106] Zhao, B. X.; Pesika, N.; Rosenberg, K.; Tian, Y.; Zeng, H. B.; McGuiggan, P.; Autumn, K.; Israelachvili, J. *Langmuir* **2008**, *24*, 1517.

[107] Zhao, B. X.; Pesika, N.; Zeng, H. B.; Wei, Z. S.; Chen, Y. F.; Autumn, K.; Turner, K. L.; Israelachvili, J. *J. Phys. Chem. B* **2009**, *113*, 3615.

[108] Hui, C. Y.; Glassmaker, N. J.; Tang, T.; Jagota, A. *J. R. Soc. Interface* **2004**, *1*, 35.

[109] Kustandi, T. S.; Samper, V. D.; Yi, D. K.; Ng, W. S.; Neuzil, P.; Sun, W. *Adv. Funct. Mater.* **2007**, *17*, 2211.

[110] Liu, J.; Hui, C. Y.; Shen, L.; Jagota, A. *J. R. Soc. Interface* **2008**, *5*, 1087.

[111] Lu, H.; Goldman J.; Ding, F.; Sun, Y.; Pulikkathara, M. X.; Khabashesku, V. N.; Yakobson, B. I.; Lou, J. *Carbon* **2008**, *46*, 1294.

[112] Northen, M. T.; Turner, K. L. *Curr. Appl. Phys.* **2006**, *6*, 379.

[113] Peressadko, A.; Hosoda, N.; Persson, B. N. J. *Phys. Rev. Lett.* **2005**, *95*, 124301.

[114] Verneuil, E.; Ladoux, B.; Buguin, A.; Silberzan, P. *J. Adhes.* **2007**, *83*, 449.

[115] Yoon, E. S.; Singh, R. A.; Kong, H.; Kim, B.; Kim, D. H.; Jeong, H. E.; Suh, K. Y. *Tribol. Lett.* **2006**, *21*, 31.

[116] Chan, E. P.; Ahn, C. H.; Crosby, A. J. *J. Adhes.* **2007**, *83*, 473.

[117] Majumder, A.; Ghatak, A.; Sharma, A. *Science* **2007**, *318*, 258.

[118] Autumn, K. *MRS Bulletin* **2007**, *23*, 473-478.

[119] Autumn, K.; Dittmore, A.; Santos, D.; Spenko, M.; Cutkosky, M. *J. Exp. Biol.* **2006**, *209*, 3569-3579.

[120] Aksak, B.; Sitti, M.; Cassell, A.; Li, J.; Meyyappan, M.; Callen, P. *Appl. Phys. Lett.* **2007**, *91*, 061906.

[121] Varenberg, M.; Gorb, S. *J. R. Soc. Interface* **2007**, *4*, 721.

[122] Varenberg, M.; Peressadko, A.; Gorb, S.; Arzt, E.; Mrotzek, S. *Rev. Sci. Instrum.* **2006**, *77*, 066705.

[123] Hertz, H. *J. reine angew. Math.* **1881**, *92*, 156-171.

[124] Maugis, D. *Contact, Adhesion and Rupture of Elastic Solids* Springer, Heidelberg **2000**, 203-343.

[125] Kendall, K. *Ph. D. dissertation* Cambridge University (UK) **1969**.

[126] Roberts, A. D. *Ph. D. dissertation* Cambridge University (UK) **1968**.

[127] Johnson, K. L.; Kendall, K.; Roberts, A. D. *Proc. R. Soc. Lond. Ser. A.* **1971**, *324*, 301-313.

[128] Maugis, D.; Barquins, M.; Courtel, R. *Métaux, Corrosion, Industrie* **1976**, *605*, 1.

[129] Derjaguin, B. V.; Muller, V. M.; Toporov, Y. P. *J. Colloid Interface Sci.* **1975**, *53*, 314-326.

[130] Tabor, D. *J. Colloid Interface Sci.* **1977**, *58*, 2-13.

[131] Kendall, K. *J. Phys. D: Appl. Phys.* **1971**, *4*, 1186.

[132] Paris, P. C.; Sih, G. C. *Fracture toughness and testing applications*, ASTM, Philadelphia **1965**, 30-83.

[133] Irwin, G. R.; Kies, J. A.; Smith, H. L. *ASTM Proc.* **1958**, *58*, 640.

[134] Kamperman, M.; Kroner, E.; del Campo, A.; McMeeking, R. M.; Arzt, E. *Adv. Eng. Mater.* **2010**, *12*, 335-348.

[135] Gao, H. J.; Yao, H. M.; *Proc. Natl. Acad. Sci. U. S. A.* **2004**, *101*, 7851.

[136] McMeeking, R. M.; Arzt, E.; Evans, A. G. *J. Adhes.* **2008**, *84*, 675.

[137] Arzt, E.; Gorb, S; Spolenak, R. *Proc. Natl. Acad. Sci. U. S. A.* **2003**, *100*, 10603-10606.

[138] Spolenak, R.; Gorb, S.; Gao, H. J.; Arzt, E. *Proc. R. Soc. London, Ser. A* **2004**, *461*, 305-318.

[139] Scherge, M; Gorb, S. N. *Biological Micro and Nanotribology: Nature´s Solutions* (Springer Verlag, Berlin) **2001**, 141-145.

[140] Greiner, C. *Ph. D. dissertation* (University of Stuttgart and Max-Planck Institute for Metals Research, Stuttgart, Germany) **2007**.

[141] Arzt, E. *Mater. Sci. and Eng. Ser. C* **2006**, *26*, 1245-1250.

[142] Spolenak, R., Gorb, S.; Arzt, E. *Acta Biomater.* **2005**, *1*, 5-13.

[143] Schargott, M.; Popov, V. L.; Gorb, S. *J. Theor. Biol.* **2006**, *243*, 48-53.

3. Sample Fabrication

Abstract – A new fabrication process to obtain micropatterned surfaces was developed. The process is a combination of three fabrication steps: photo lithography, reactive ion etching and two-step molding. With this fabrication approach it is possible to obtain pillars with dimensions on the micrometer length scale and below. Further, the geometry of the pillar sidewalls can be modified in a controlled way without an additional sample preparation process such as inking and printing.

3.1 Introduction

The investigation of biological attachment systems has shown that several animals possess patterned surfaces on their toes [1-21]. These attachment systems usually have a complex geometry and exhibit a hierarchical design. The tokay gecko as the largest and heaviest animal supporting a patterned attachment surface, shows the most complex geometries. This suggests that a good adhesion performance requires an optimized geometry of the adhesive pillars. To mimic these complex geometries, several fabrication methods were developed. Simple patterns, e.g. containing cylindrical pillars, can be fabricated quite easily. However, more complex pillars with modified tip geometries or hierarchical systems require a complicated fabrication process. These processes are either hard to reproduce or contain fabrication steps with sacrificial templates, which makes the process both time consuming and expensive. A thorough overview of current fabrication methods was given in Chapter 2. In the following sections, a new fabrication method consisting of photo lithography, reactive ion etching (RIE) and two-step molding is presented.

3.2 Experimental

The method for fabrication of micropatterned surfaces is based on molding of photo lithographically patterned templates, but differs from current processes in the template fabrication and an additional molding step. Conventional molding of lithographically patterned templates contains two fabrication steps; photo lithography is used to fabricate a patterned template and molding to transfer the pattern from the template to the sample material. The complete process of this conventional process is described in the following.

First, a silicon wafer is coated with a photo resist. This resist is UV-exposed through a lithographic mask. Depending on the chemical properties of the photo resist, the pattern on

the mask is transferred to the photo resist as a positive or a negative pattern. After several heat treatments, the resist is developed. This results in a patterned template that can be used as a mold. An optional step is a surface modification of the template after lithography, e.g. silanization with a fluorosilane, to prevent sticking of the sample material to the template during the following molding step. The liquid sample material is then poured onto the template and cured to form a solid. After careful removal of the cured material from the template, a patterned surface is obtained which can be processed further.

This conventional molding process allows the control of the template top view within the resolution of photolithography and of the aspect ratio (AR) by changing the thickness of the photo resist. By tilting the wafer during the exposure step it is possible to obtain tilted pillars as well. However, the sidewalls of the pillars will always be straight. To fabricate for example defined tip geometries, an additional modification step is necessary. Even with modification processes it is not possible to control the whole pillar shape completely, because only the geometry of the very ends of the pillars can be modified. Moreover, the template is made out of a polymeric photo resist material which may be damaged during demolding, and cleaning with aggressive chemicals is not possible.

To fabricate durable templates with controlled geometry a new fabrication approach based on RIE was developed. Wafers were patterned by photo lithography as described above. The photo lithography process for the new fabrication method, however, differed slightly from the usual process, as the photo resist was used as an etching mask. Thus, a thin photo resist layer was sufficient. Depending on the chosen template geometry (positive or negative), an additional molding step was necessary. Figure 3.1 shows the process schematically.

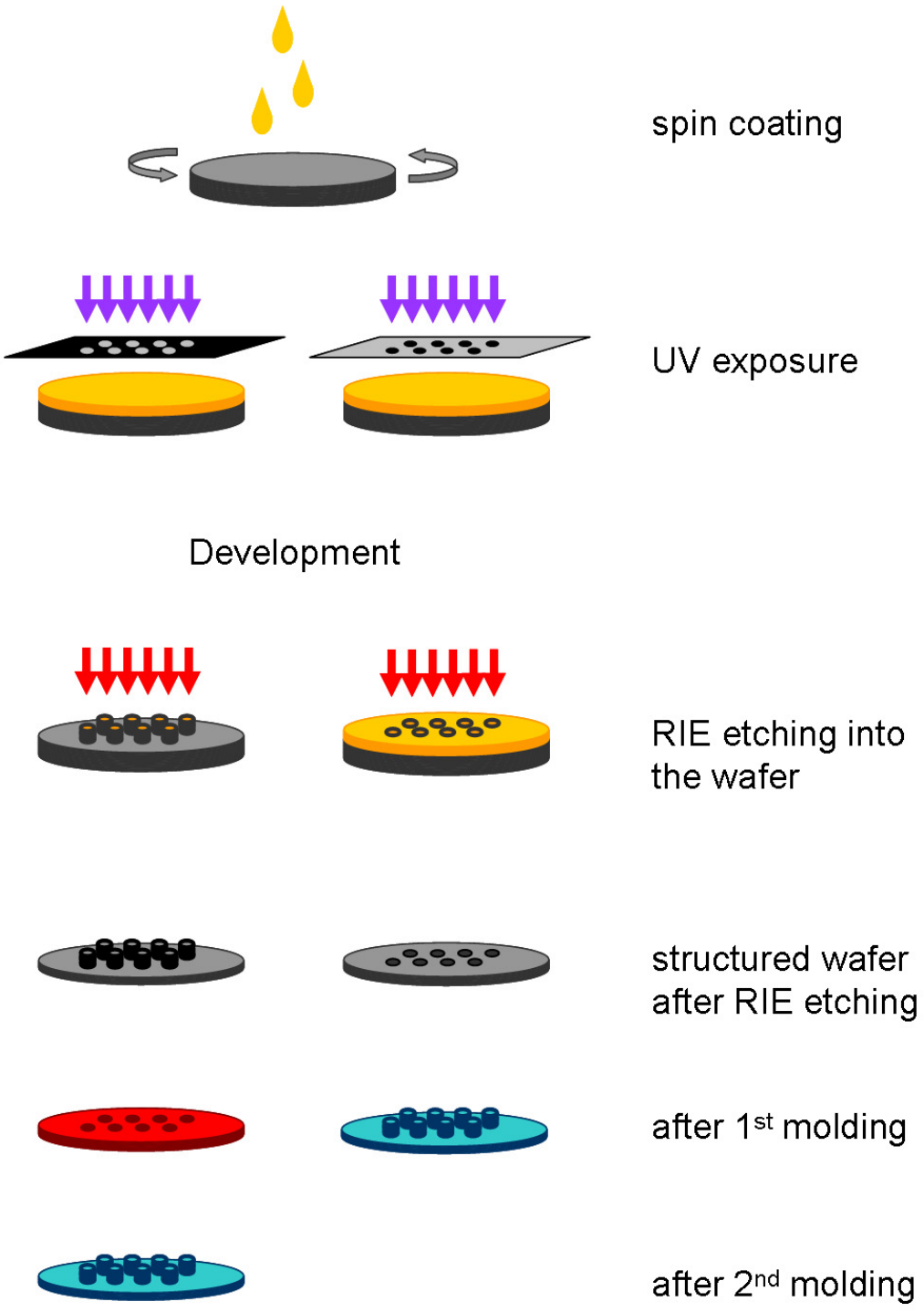

Figure 3.1: Fabrication steps of the developed molding process. A wafer is spin-coated with a photo resist and exposed to UV light through a lithography mask. After development, an RIE process is performed to etch the pattern into the wafer. Depending on the chosen template geometry, the sample can be molded directly from the template (left path) or indirectly (right path) by performing a soft template first.

3.2.1 Photo lithography

Photo lithography was performed in the clean room (class 1000/100) of Mitranz, Saarland University, Germany. The negative photo resist SU8-2 and the developer mr-600-dev were purchased from Micro Resist Technology GmbH, Germany. The SU8 was spin-coated onto polished silicon wafers (provided by CrysTec GmbH, Germany) in a spin-coater from Carl Süss MicroTec AG, Germany. After thermal evaporation of the solvent in the resist, the coated wafers were exposed through a mask in a Mask-Aligner (Carl Süss MicroTec AG, Germany) using a broad band UV-source with a sub-365 nm UV-filter. The photolithographic mask was purchased from MC&L GmbH, Germany. After another heat treatment the samples were developed and rinsed in isopropanol. All thermal treatments were performed on a contact heating plate.

3.2.2 Reactive ion etching

The patterned wafers were etched using an inductively coupled plasma (ICP) RIE device with a so-called gas chopping process. To control the etching process and to obtain perpendicular side walls or controlled non-perpendicular side walls, several etching and passivation steps were performed. After the etching, the remaining photo resist and other organic material were removed by applying oxygen plasma, or alternatively heating the etched wafers in an oven above 600°C. The RIE etching was performed at the Max Planck Institute for Metals Research in Stuttgart, Germany. For the etching process a PlasmaLab 80 (Oxford Instruments) was used with SF_6, HCF_3 and O_2 as process gases and N_2 for chamber venting. The RIE process is a combination of physical and chemical dry etching. In the reaction chamber, plasma containing different ions and radicals is generated. The ions are accelerated perpendicular to the sample and cause a sputter effect. The produced radicals react chemically with the sample. In Figure 3.2 a schematic of an RIE machine is shown.

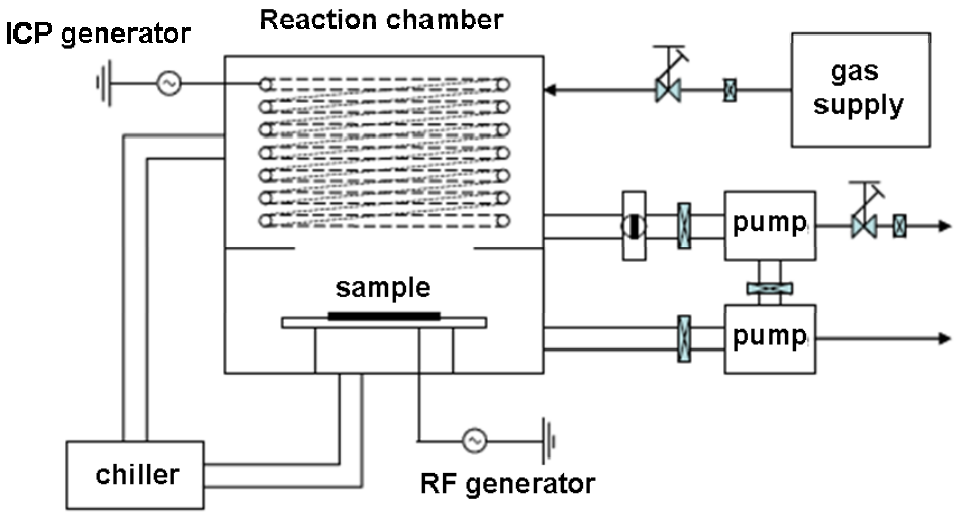

Figure 3.2: Schematic of an ICP-RIE device, containing RF generator, ICP generator, reaction chamber, chiller, gas supply, pumps and the valve system.

The RIE contained a Radio Frequency (RF) generator, an ICP generator, a chiller for sample temperature control, a pumping and valve system and a gas supply. The process gases were pumped into the reaction chamber, where both generators created plasma by applying an AC voltage with a frequency of 13.56 MHz. The pressure in the reaction chamber was controlled by the valve system. Depending on RF power, ICP power, gas flow, gas mixture, process temperature and chamber pressure, both the physical and the chemical etching were controlled. Under certain process conditions the ICP-RIE device allowed the deposition of thin films by plasma polymerization using CHF_3 process gas. The reaction products were deposited on the sample, forming a fluorocarbon layer.

The radicals in the plasma, mainly fluorine radicals, had a different selectivity for etching silicon and the photo resist. While the silicon was etched by the radicals, the photo resist remained stable. Thus, the photo resist mask on the wafer protected the silicon underneath, while accessible silicon was etched by the process. This allowed the transfer of the photo lithographic pattern to the wafer.

To achieve a controlled side wall profile, a gas chopping protocol was used. This method contained a passivation and an etching step. For passivation a thin fluorocarbon layer was deposited on the sample. During the following etching step the passivation layer was sputtered off areas parallel to the wafer surface only, which was then etched chemically by the radicals. Areas perpendicular to the wafer surface remained passivated and were not etched by the fluorine radicals. These two steps were repeated several times, each time etching deeper into the sample. The etching depth was controlled by changing the number of etching and passivation cycles.

3.2.3 Two-step molding

To obtain a template for adhesive patterns, two approaches were possible. Either, the template was fabricated as a negative or as a positive, in this case a silicon template with holes, or pillars. The etching of holes, however, had two main drawbacks; the shape of the sidewalls was not easily controllable, as the gas transport into the holes during the ICP-RIE process became more difficult with increasing etching depth. Further, the bottoms of the holes which became the tips of the pillars were not well defined. The etching always induced a certain roughness and the bottom edges in the holes were not sharp. In the case of silicon pillars, these problems did not occur. The gas transport around free standing pillars was not affected by the etching depth. Removing the photo resist exposed the original wafer surface at the tip of the silicon pillars and led to a very low roughness. However, to obtain the final pattern from a template with free standing pillars, an additional molding step was necessary.

For the first molding, the polyurethane (PU) PolyOptic 14-70, purchased from PolyConform, was chosen. This two component system was mixed with 5:4 ratio of a dialcohol and a diisocyanate component (no chemical composition availabe). After mixing, the viscous liquid

was poured onto the template and hardened for 48 hours at room temperature. The resulting soft polymer was de-molded from the silicon template. A silanization of the silicon template was not necessary. The PU template was then used for the preparation of patterned polydimethylsiloxane (PDMS) samples.

3.2.4 Fabrication of PDMS samples

PDMS samples were fabricated using two different types of templates. To obtain patterned samples, the fabrication procedure was performed as described above. After the fabrication of the PU template, the two component PDMS kit Sylgard 184 (Dow Corning, UK) was mixed in a 10:1 ratio of pre-polymer and cross-linker (no chemical composition available). Air bubbles due to mixing were eliminated by evacuating in a desiccator. The viscous liquid was then poured onto the PU template and cross-linked at 75°C for 72 hours in air, which is known to be sufficient to achieve a polymerization state allowing reproducible adhesion measurements [22-23]. Afterwards the PDMS was carefully demolded from the PU template. Some samples were prepared directly on unpatterned silicon wafers to obtain flat PDMS. For these experiments the PDMS sample fabrication was varied by changing curing time, pre-polymer to cross-linker ratio, sample cleaning and several other parameters, see Chapter 5.

3.3 Results

As the photo resist was used as an etching mask only, a resist thickness of 1 to 5 µm was sufficient. The process optimization for a 2 µm thick resist layer led to the following parameters used for the structuring of all wafers.

1. Thermal pre-treatment of the wafer at 200 °C for 5 minutes in air
2. Pouring ~ 3.5 ml of degassed SU8-2 photo resist onto the wafer
3. Spin-coating with 3000 rpm spin speed and acceleration of 100 rpm/s for 1 minute
4. 10 minutes waiting time for resist re-flow
5. Pre-bake: heating ramp (up to 95 °C, 3 minutes) and holding at 95°C for 5 minutes
6. UV-exposure for 8 seconds in vacuum-contact mode of the mask aligner
7. Post exposure bake for 1 minute at 65 °C and 1 minute at 95 °C
8. Development for 1.5 minutes in *mr-dev-600* and rinsing with isopropanol
9. 30 minutes hard-bake at 200 °C

The re-flow time was introduced to allow the photo resist to compensate differences in the resist thickness due to the radial symmetric spin coating profile. A detailed description of the influence for each process parameter can be found in [24]. After optimizing the photo lithography process, the masked silicon wafer was etched. A process for perpendicular etching was developed. This process can be used as starting point for controlled variation of the side wall shape. The process parameters are shown in Table 3.1.

Table 3.1: Process for perpendicular etching

gas	RF power	ICP power	pressure	gas flow	step duration	Temperature
etching parameters						
SF_6	30 W	300 W	40 mTorr	15 sccm	5 s	-10°C
CHF_3				18 sccm		
passivation parameters						
CHF_3	30 W	100 W	70 mTorr	50 sccm	8 s	-10°C
oxygen cleaning						
O_2	15 W	300 W	80 mTorr	50 sccm	5 min	-10°C

(Further details of specific influences of each parameter can be found in [24])

Figure 3.3 shows a silicon wafer after photo lithography and ICP-RIE. The cylindrical pillars have a diameter of ~ 1.5 µm and a height of ~ 4 µm. In between the pillars, some needle like artifacts can be seen.

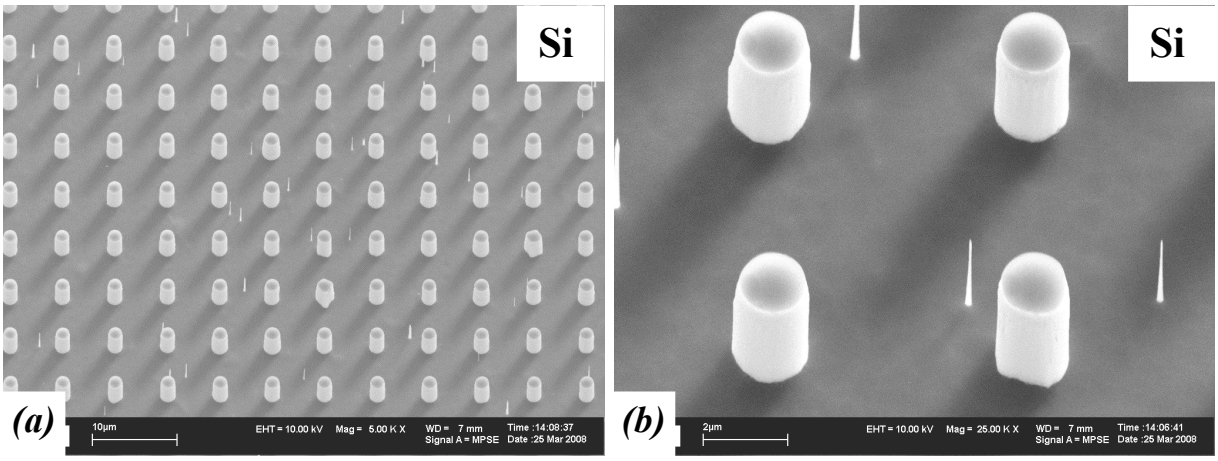

Figure 3.3: Scanning Electron Microscopy (SEM) pictures of a silicon wafer after photo lithography and ICP-RIE. The cylinders have a diameter of ~ 1.5 µm, a center-to-center spacing of ~ 6 µm and a height of ~ 4 µm (a). Fine needles in between the pillars are present (b). Pictures were taken with 30° tilt.

Figure 3.4a shows cylindrical pillars with photo resist on the pillar tip, which was then removed by oxygen plasma or heating above 600°C in air. Light microscopy as well as white light interferometry (ZYGO Corp., USA) and SEM investigation (Zeiss AG, Germany) showed that applying oxygen plasma or heating the silicon wafer above 600°C led to pillar tips with wafer flatness, indicating that the resist was removed completely.

The surface roughness of the sidewalls depended on the etching and passivation time within a cycle and was below 50 nanometers, which equals the etching depth per cycle. By tilting the wafer during the etching process, pillars with a defined tilt angle were produced. The etching grooves on tilted cylinders can be seen in Figure 3.4b.

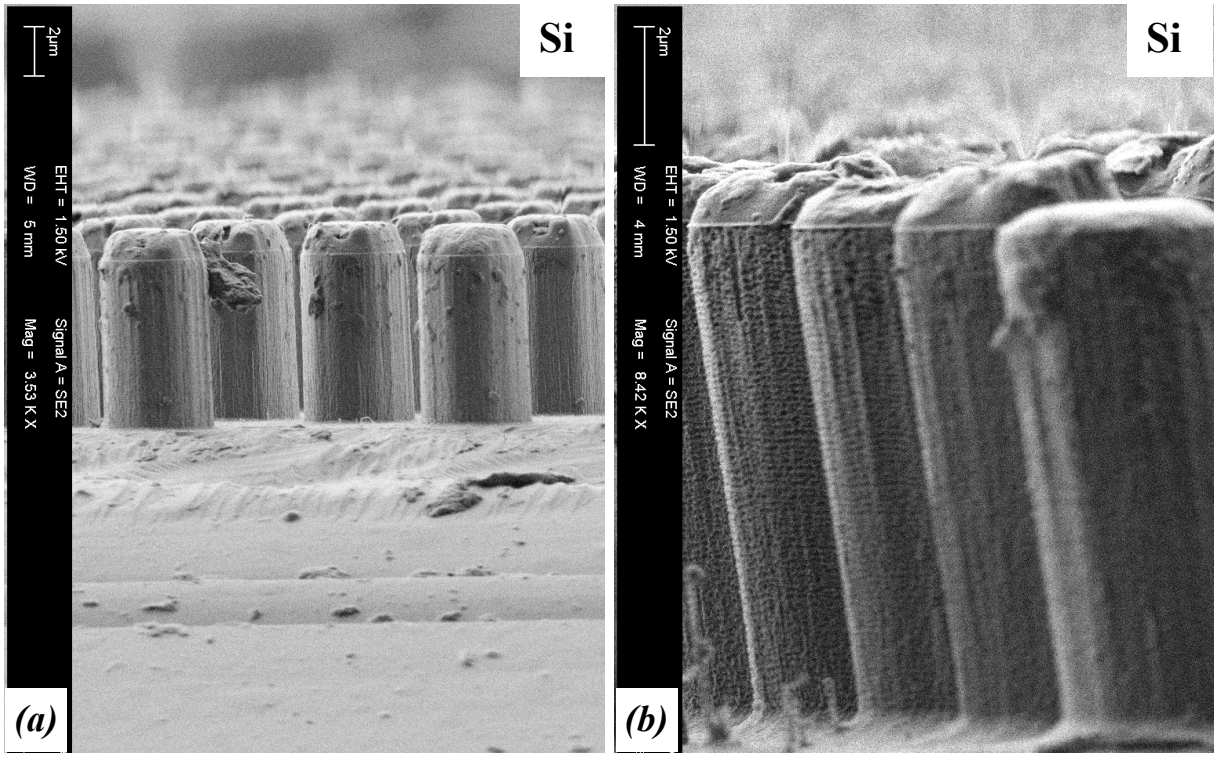

Figure 3.4: SEM picture of silicon wafers after photolithography and ICP-RIE. The photo resist is still located on top of the pillars (a). Tilted pillars with higher magnification are shown in (b). The horizontal etching grooves caused by gas chopping are visible.

By changing the etching and passivation time within the cycles, it was possible to etch mushroom shaped pillars, as shown in Figure 3.5. This was achieved by choosing a longer etching time within one gas chopping cycle. The side wall roughness increased.

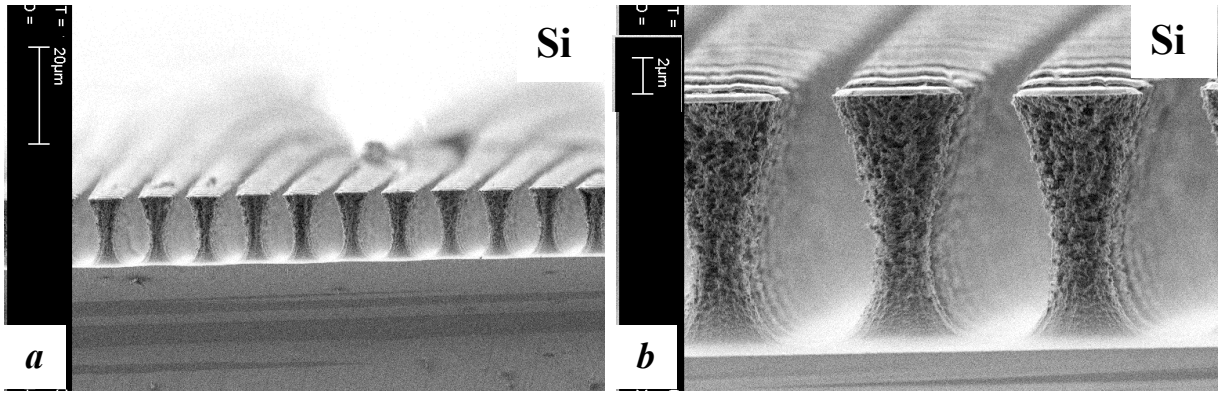

Figure 3.5: SEM pictures of perpendicular silicon pillars with a mushroom-shaped tip (a). A longer etching time increased the surface roughness (b).

The molding process allowed transfer of the pattern from the silicon template to the PDMS sample by the additional PU molding step. Figure 3.6 shows a white light interferometry image of a PDMS pattern in 3D (Figure 3.6a) and as a profile plot (Figure 3.6b). The PDMS pillar height was ~ 6.5 µm and the diameter was ~ 2 µm. Figure 3.6c shows a light microscopy picture of damaged PDMS pillars.

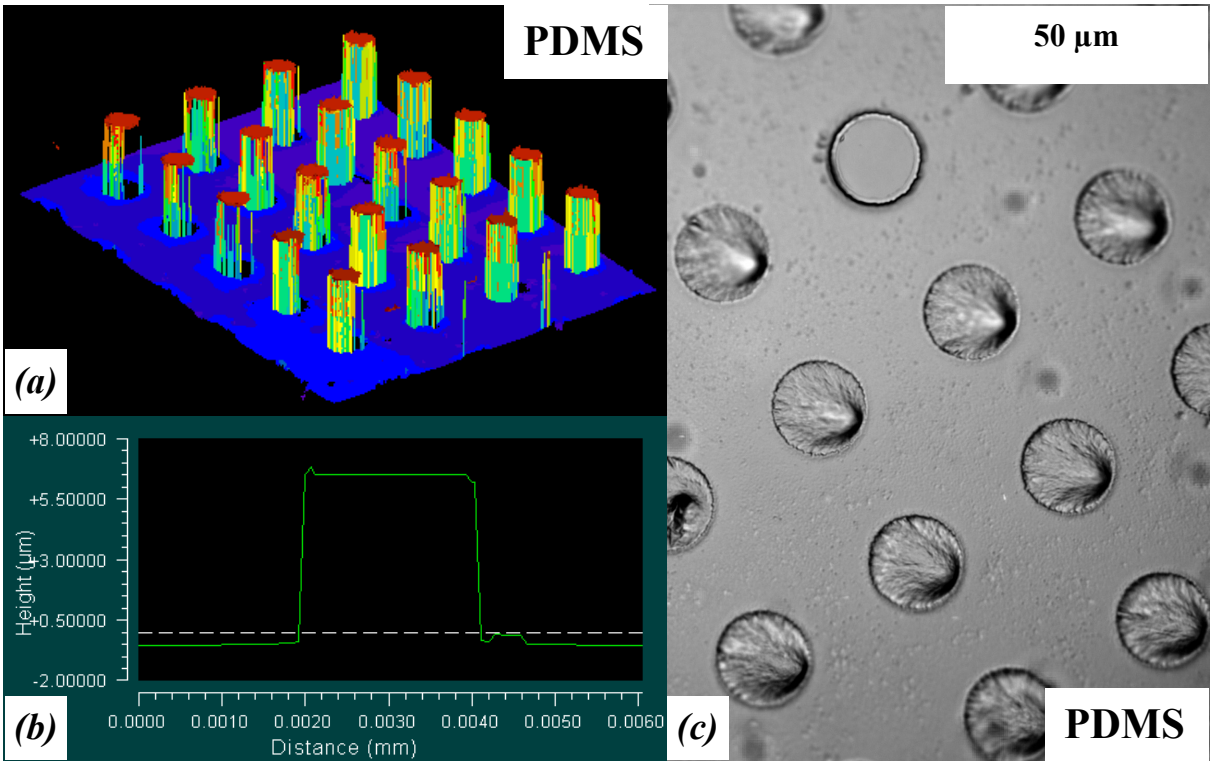

Figure 3.6: Patterned PDMS samples. In (a) and (b), a 3D WLI image and a profile plot of PDMS pillars with ~ 2 µm diameter and ~ 6,5 µm height is shown. Note that the different axes are not scaled identically. Damaged PDMS pillars after demolding, imaged by light microscopy (c).

To avoid effects of physical and chemical change of the PDMS samples due to aging effects during measurements, all samples were left for relaxation for several days.

3.4 Discussion

The new fabrication approach shows several improvements compared to conventional molding of photolithographic templates. The photo lithography process becomes less complicated as several problems are solved by using a thin resist layer. First, the adhesion of a thin resist layer on silicon wafers is very high, while thick resist layers often delaminate during development. Second, the resolution of optical lithography is increased by using thin compared to thick resist layers, as light scattering effects in the mask are generally smaller for thin resist layers. And last, as long as there is no need for high etching depths, all samples can be prepared using the same photo lithography protocol, while the conventional process requires a new protocol for each resist thickness and thus for each pillar height.

The RIE process allows the fabrication of straight geometries such as cylinders as well as more complex geometries with mushroom-shaped tips or tilted pillars, as shown in Figures 3.3 to 3.5. The surface roughness for perpendicular pillars is low, but increases for mushroom shaped pillars. It has to be taken into account that depending on the total amount of photo resist on the wafer surface, the etching process has to be corrected due to slightly differing chemical interactions between resist and plasma, which influences the etching behavior. In addition, mushroom shaped pillars with significantly larger tip radii than the pillar base are likely to damage during demolding (see Chapter 2 Figure 2.2c).

The first molding step of the silicon template with PU and the second molding to achieve the final PDMS samples results in well defined sample patterns and pillars, as can be seen in Figure 3.6. The demolding, especially for PDMS from PU, has to be performed carefully to avoid damage of the pillars. A chemical surface modification of the templates for easy release such as silanization, however, is not necessary for neither of the molding steps.

3.5 Conclusion

The new fabrication process allows accurate control of the pillar geometry for PDMS samples. Compared to conventional molding of photo lithographically patterned templates it has several advantages.

- The lateral resolution for photo lithography, especially for higher ARs is improved, as only thin photo resist layers are exposed.
- Different ARs can be achieved using one photo lithography process because the photo resist serves only as an etching mask.
- The shape of the sidewalls can be modified in a controlled way by changing the ICP-RIE parameters.
- No surface modification of the templates such as silanization is required.

As with RIE etching an additional fabrication step is introduced, compared to direct molding of lithographically patterned templates, the process becomes more complex. However, additional sample modification procedures such as inking and printing are not necessary within the fabrication limits of this new process.

3.6 References

[1] Arzt, E.; Gorb, S.; Spolenak, R. *Proc. Natl. Acad. Sci USA* **2003**, *100*, 10603.

[2] Autumn, K.; Majidi, C.; Groff, R.; Dittmore, A.; Fearing, R. *J. Exp. Biol.* **2006**, *209*, 3558–3568.

[3] Autumn, K.; Peattie, A. *Integr. Comp. Biol*. **2002**, *42*, 1081.

[4] Gorb, S. N. *Attachment devices of insect cuticle* New York, NY: Springer **2001**.

[5] Gorb, S. N.; Beutel, R. G. *Naturwissenschaften* **2001**, *88*, 530–534.

[6] Haase, A. *Archiv für Naturgeschichte* **1900**, *66*, 321-345.

[7] Hiller, U. *Z. Morphol. Tiere* **1968**, *62***,** 307-362.

[8] Hiller, U.; Blaschke, R. *Naturwissenschaften* **1967**, *54*, 344-345.

[9] Irschick, D.J. *Biol. J. Linnaean Soc*. **1996**, *59*, 21.

[10] Maderson, P.F.A. *Nature* **1964**, *203*, 780.

[11] Peterson, J.A.; Williams, E.E. *Bull. Mus. Comp. Zool.* **1981**, *149*, 215.

[12] Roll, B. *J. Zool*. **1995**, *235*, 289.

[13] Russell, A.P. *Can. J. Zool*. **1986**, *64*, 948.

[14] Russell, A.P. *J. Morphol*. **1981**, *169*, 293.

[15] Russell, A.P. *J. Zool. London* **1975**, *176*, 437-476.

[16] Russell, A.P.; Bauer, A.M. *J. Morphol*. **1988**, *197*, 221.

[17] Russell, A.P.; Bauer, A.M. *Mem. Queensl. Mus*. **1990**, *29*, 453.

[18] Ruibal, R.; Ernst, V. *J. Morphol*. **1965**, *117*, 271-294.

[19] Schleich, H.H.; Kästle, W. *Amphibia-Reptilia* **1986**, *7*, 141.

[20] Stork, N. E. *J. Nat. Hist.* **1983**, *17*, 829-835.

[21] Williams, E.E.; Peterson, J.A. *Science* **1982**, *215*, 1509-1511.

[22] del Campo, A.; Greiner, C.; Arzt, E. *Langmuir* **2007**, *23,* 10235-10243.

[23] Greiner, C.; del Campo, A.; Arzt, E. *Langmuir* **2007**, *23,* 3495-3502.

[24] Kroner, E. *Diploma thesis: „Influence of the substrate on the contraction behaviour of heart muscle cells"* (University of Stuttgart and Max-Planck-Institute for Metals Research, Stuttgart, Germany) **2007**.

4. A New Adhesion Tester

Abstract – Current adhesion measurement set-ups, either commercial or home-built, do not allow adhesion measurements with *in situ* visualization, high resolution, high force range and controlled alignment at the same time. Especially the possibility of measuring with controlled alignment is important for adhesion experiments with flat probes. In this chapter a new adhesion tester is presented, which is especially designed for measuring adhesive properties of patterned surfaces. With this new set-up contact experiments with controlled tilt angle (accuracy of +/- 0.02°) can be performed. This allows the use of flat probes, which simplifies determination of experimental parameters such as pull-off strength or Young's modulus. The deflection of a double-clamped cantilever is measured by laser interferometry with an accuracy of ± 60 nm, which yields a precise force measurement over three orders of magnitude force range without changing the cantilever. The cantilever design allows fast exchange between different probes. Contact experiments can be visualized *in situ*. The set-up is easily extended to include temperature and humidity control or friction experiments. The current adhesion tester is designed for force measurements in the range of 1 μN to 1 N and fills the gap between macroscopic tests and atomic force microscopy measurements.

4.1 Introduction

During the last several years, bioinspired adhesives based on patterned surfaces have found much attention due to their unique adhesion performance [1-9]. While there has been great progress in material development and patterning methods to fabricate bioinspired adhesives, methods for adhesion measurements of these surfaces was not developed to the same extent. The most commonly used adhesion test for bioinspired adhesives is the JKR-type experiment [2-3,9-19], named after *Johnson*, *Kendall* and *Roberts* [14]. A spherical probe is brought into contact with a sample and forces are measured as a function of displacement. JKR-type set-ups are robust as misalignment of sample and the spherical probe is not relevant. Sometimes the spherical geometry of the probes was claimed to be a well defined roughness with a single asperity [9,17], thus representing a measurement configuration closer to "real" surfaces. However, such tests suffer from several drawbacks: first, data interpretation may turn out difficult as the contact area depends on preload. For extracting pull-off stresses, the contact area must be calculated [2,4,13] or observed *in situ* [10-12,20-24]. A second complication in JKR-type experiments on patterned samples is that pillars below the center of the spherical probe experience a different deformation than pillars close to the boundary region of the contact area. During detachment, the pillars near the boundary are under tension while pillars below the center of the probe may still be under compression. This leads to a stepwise detachment of sample and probe [9,10-13,17,19,24-25], which complicates data analysis further.

These problems of spherical probe geometries can be avoided by using flat probes instead. This, however, requires minimization of misalignment between probe and specimen. In the past, adhesion measurements were performed using flat probes without attention to alignment [1] or with measurement set-ups exhibiting a "self-aligning" mechanism [3,26]. In both cases

experimental control over contact formation and detachment is insufficient, rendering questionable results. Here, a new adhesion tester is presented which allows high precision flat probe measurements with controlled alignment. First, the experimental set-up will be described, containing the design strategy, the hardware set-up and the software features. In Chapter 4.3 some measurement results will be presented and discussed in Chapter 4.4, finishing with a conclusion in Chapter 4.5.

4.2 Experimental

The main requirement for the adhesion tester, in the following referred as MAD (Macroscopic Adhesion measurement Device), was the possibility to perform measurements with flat probes at controlled tilt angle. Other specifications included high force resolution, high force measurement range and the possibility for further extensions, especially *in situ* visualization and measurements under controlled temperature and relative humidity.

4.2.1 Design strategy

Controlled alignment required either the sample or the probe to be tilted to a prescribed angle. This tilt needed to be controlled to ensure a constant tilt angle during measurement. To maximize force resolution, it was self-evident to fix the probe to a robust measurement system. The sample needed to be positioned with the adhesive surface facing up for practical reasons, as this allowed fast sample exchange without additional fixation. The requirement of sample tilt was achieved by placing the sample on a positioning table which allowed linear movement along and tilt around all geometrical axes. The force sensing system could not be implemented in the sample positioning system, as tilt angles would result in a deviation of the applied and measured forces, as schematically shown in Figure 4.1. The force sensing, therefore, needed to be implemented in the probe part of MAD.

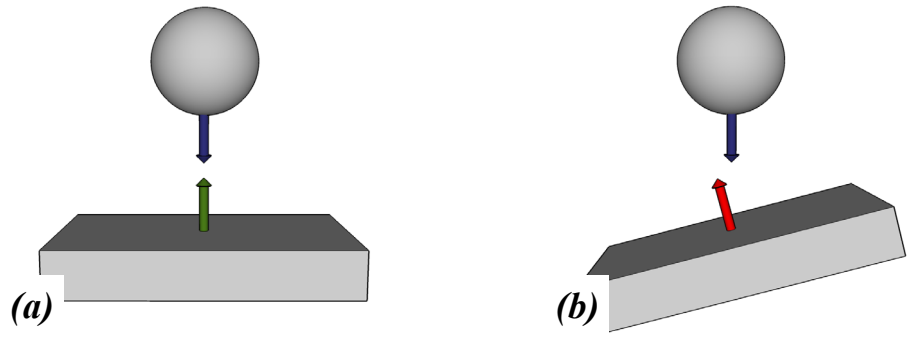

Figure 4.1: Force detection for tilted measurements. The force sensor measures forces perpendicular to its surface. If the force sensor is moved parallel to the force acquisition direction (a), the forces are measured correctly. For tilted measurements (b), only the vertical force component will be measured.

Typical force sensors do not allow control of alignment during the measurement and were therefore not suitable for force measurements in this set-up. A way to measure forces while controlling the alignment passively is a combination of cantilever and laser interferometer. A mirror was mounted to a cantilever, and deflections were measured by the laser interferometer. By calibration of the cantilever, forces could be calculated from the deflections. If the cantilever tilted during the measurement, the laser beam was not reflected back to the interferometer, causing a loss in detected laser intensity and thus in a tilt control (Figure 4.2). The use of a table positioning system and a laser interferometer blocked two optical axes for *in situ* visualization of the contact area. The only possibility to realize *in situ* visualization is using a horizontally positioned optical system. This allowed both detecting the side view directly and the contact area using a mirror system, as shown in Figure 4.3. However, visualization of the contact area was then restricted to transparent samples or to flat and transparent probes, as the contact formation could only be seen through one of them. Further extensions such as an environmental chamber for controlled temperature and relative humidity can be implemented into the measurement set-up.

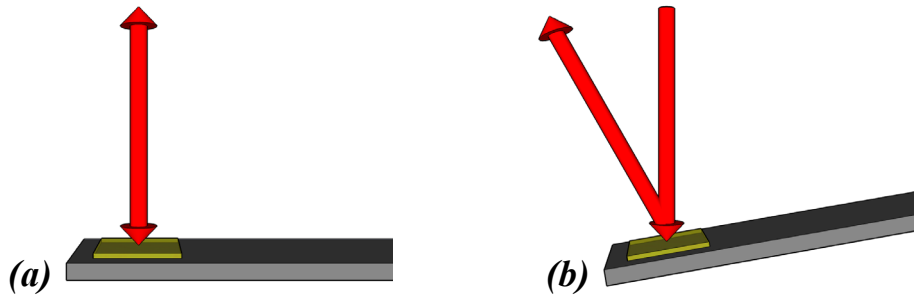

Figure 4.2: Passive alignment control during measurement using a laser interferometer. If the mirror on the cantilever is perpendicular to the laser beam direction, the laser will be reflected back to the interferometer (a). If the cantilever is tilted during measurement, the laser will not be reflected back to the interferometer, causing an intensity change in the detected laser intensity (b).

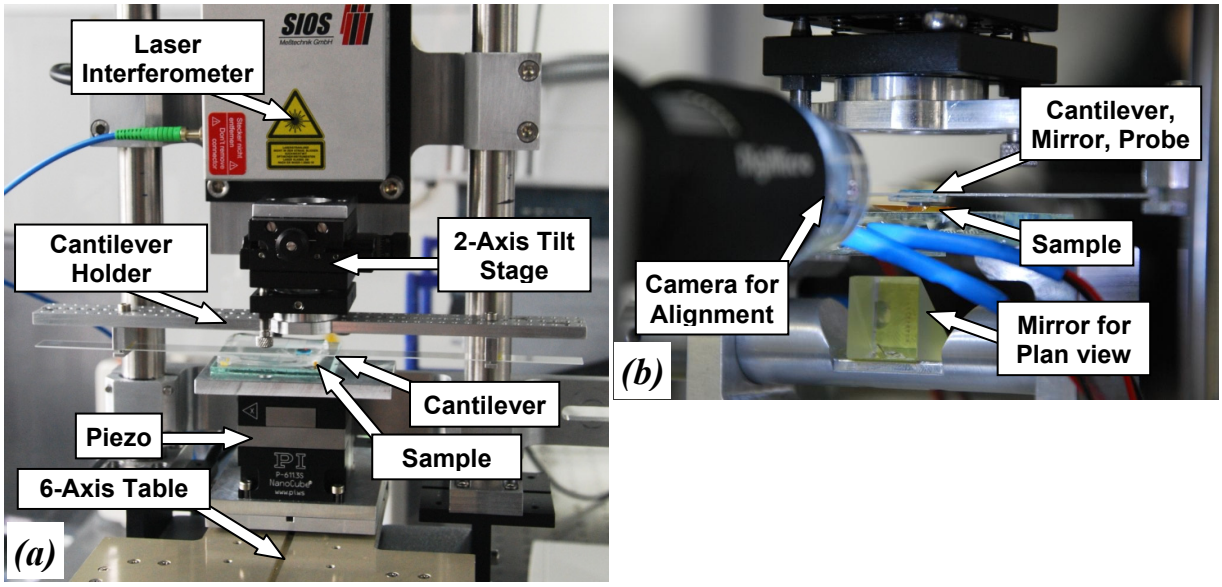

Figure 4.3: Adhesion tester MAD. (a): The lower part of the set-up shows the sample positioning system for displacement and tilt, containing a six-axis table and a three-axis piezo, upon which the sample is placed. The upper part shows the force sensing system containing a laser interferometer, a two-axis tilt stage, the cantilever holder and the cantilever. (b): Close up of the setup. The contact area is monitored with a camera. The side view is imaged directly and the plan view through the sample or probe using a mirror system.

4.2.2 Hardware set-up

For the hardware set-up a high precision six-axis positioning table was purchased from Physik Instrumente Karlsruhe, Germany (Hexapod F.206). This table allowed a positioning accuracy of 100 nm for movement in x, y and z direction as well as rotation along all three geometrical axes. For high-resolution measurements a three-axis piezo stage was purchased from Physik Instrumente Karlsruhe, Germany (Nanocube). This piezo allowed a movement in x, y and z direction with a resolution of 1 nm. The laser interferometer was provided by SIOS Messtechnik, Ilmenau, Germany (miniature interferometer SP 100). Changes in distance were measured with a resolution of 1.2 nm and environmental data (air pressure, temperature, laser wavelength) was acquired. Changes in the laser wavelength due to changing temperature and air pressure were corrected automatically. To add a further alignment possibility of sample and probe, a two-axis tilt stage was purchased from OWIS GmbH, Stauffen, Germany, which was used for mounting the cantilever holder. The whole set-up was installed on an optical table. For further vibration isolation the device was placed upon an active anti-vibration table (TS 150), bought from Technical Manufacturing Corporation, USA.

Figure 4.3 (see previous page) shows an image of the set-up. The piezo was mounted directly to the six-axis table. This allowed sample positioning as well as high-resolution movement from the lower part of the device. However, it had to be taken into account that the piezo tilted with the six-axis stage. Thus, the z-direction of the piezo depended on the tilting of the six-axis stage. For measurement a sample was placed on top of the piezo and positioned below the probe. The laser interferometer was mounted directly to the construction of the six-axis table, to minimize vibrations and to allow high long term stability. The poles on which the interferometer was mounted were made out of invar to minimize thermal expansion and allow maximum stability, which was important especially for long term experiments. The cantilever holder was designed to allow fast cantilever exchange and high calibration stability.

By using several cantilever holders, it was not necessary to remove the cantilever beam from the holder. The cantilever holder could be tilted around and moved along the x and y axis using the two axis stage. With this further possibility of alignment, adhesion tests with non-spherical probes (such as flat probes) and controlled alignment were possible.

Cantilever design – The cantilevers for force measurements had to fulfill three main requirements. First, their spring constant had to be highly stable and independent of temperature to ensure consistent results even for slightly changing temperature. Second, the spring constant had to be independent of the cantilever deflection to simplify data analysis. And third, the cantilever had to deflect without tilt for the complete measurement range. Two cantilever designs were tested for MAD: single-clamped and double-clamped cantilevers (Figure 4.4). For the single-clamped cantilever, a mirror and a probe were fixed to the top and the bottom of the loose end, respectively. In the double-clamped design, the mirror (top) and the probe (bottom) had to be glued exactly in the middle of the cantilever.

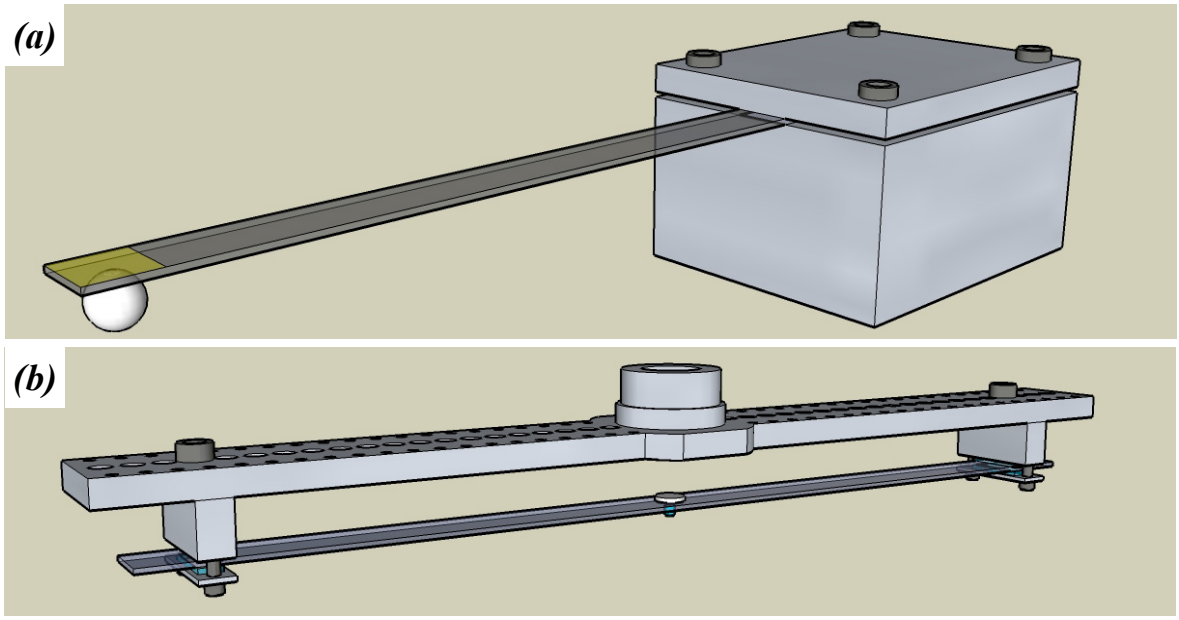

Figure 4.4: Two different cantilever designs for MAD. The cantilever can be clamped either on one end (a) or on both ends (b).

Single-clamped cantilevers had several advantages. The cantilever beam, e.g. a glass plate, could easily be fixed to the cantilever holder and the spring constant was then modified by changing the beam length, width or thickness. However, it had to be expected that at a certain deflection the cantilever would tilt due to the geometric deformation of the beam. In addition, the compliance of the cantilever for torsion around the beam axis was high, which could result in additional tilt.

Double-clamped cantilevers were more complex in their geometry. The laser beam needed to be reflected on a mirror glued to the cantilever. Thus, the cantilever holder needed to have a hole above the mirror. As the beam was fixed to the holder on both ends, the thermal expansion of the beam and the holder either needed to be identical to avoid a change in the tension of the beam and thus in the spring constant, or at least one end of the cantilever had to permit movement along the cantilever axis. Three different cantilever set-ups were designed as shown in Figure 4.5: a metal band cantilever, a glass beam, where on end was not fixed completely, and a glass beam which was clamped between two polydimethylsiloxane (PDMS) pieces. All cantilevers were calibrated using a commercial force transducer. The cantilever was brought into contact with the force sensor and cantilever deflection and force were measured.

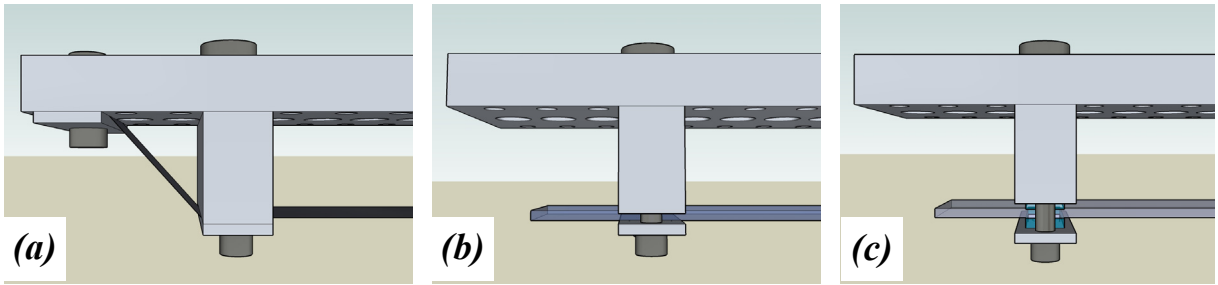

Figure 4.5: Different cantilever fixations for double-clamped cantilevers. A thin metal band under tension (a), a glass cantilever with one slightly loose fixation (b) and a glass cantilever fixed with PDMS between clamps and the glass beam (c).

4.2.3 Software

The software for MAD was written in the graphic program language LabView (Version 8.5, National Instruments). The software allowed the physical channels of the laser interferometer, the piezo and the six-axis table to be transferred into virtual channels and vice versa. The program was designed in a modular way. Each module was a stand-alone function of the whole program. This modular programming allowed easy extension for future applications. The available modules are the following:

- automatic force measurement, displacement by piezo
- automatic force measurement, displacement by table; including low frequency data acquisition for long term measurements and holding time at maximum preload
- preload scan functions for both piezo and table controlled measurements
- six-axis stage control
- automatic surface detection
- acquisition of environmental data; laser wavelength, temperature, air pressure, laser intensity with optic and acoustic output for calibration and cantilever test (control of laser intensity as a function of deflection).
- automatic cantilever tilt test

The automatic force measurement included all data acquisition. The piezo/table and cantilever displacement were recorded and correlated to each other. The number of measurement cycles, measurement velocity and displacement range could be freely chosen within the technical limitations of the hardware. As output data, the program created a header file including all relevant measurement data such as probe geometry, spring constant, measurement parameters and environmental data. The measurement data was saved as a data file for each measurement cycle, which could be directly imported into a spreadsheet program. With the preload scan

function it was possible to automatically perform measurements with varying preload. The six-axis stage control allowed complete control of the six-axis table and accurate sample positioning within the hardware limitations. The automatic surface detection created surface contact rapidly. It shortened the time between sample loading and measurement significantly. The acquisition of environmental data tool recorded temperature, air pressure and wavelength of the laser interferometer as well as all the variables entered by the user. It displayed the intensity of the reflected laser with an additional acoustic output, which simplified laser calibration. Another feature was the cantilever tilt test. Here, the cantilever was deflected within the measurement range while controlling the laser intensity. This allowed qualitative detection of cantilever tilt during a simulated measurement.

4.3 Results

For the single-clamped cantilever, a maximum deflection of ± 45 µm was measured, before the reflected laser intensity became too low for further measurements. This indicated cantilever torsion, which disqualified the use of such cantilevers for measurements with controlled alignment. For this reason, no further tests were performed with single-clamped cantilevers. However, with double-clamped cantilevers deflections of several hundred µm were achieved without significant change in laser intensity. Only above 500 µm deflection did the laser intensity change, indicating cantilever torsion.

The three different fixation systems in Figure 4.5 were tested. The system with a metal band (Figure 4.5a) was calibrated, but the resulting spring constants scattered to great extend, resulting in an error of more than 50%. The system with a glass cantilever, where one end was not fixed completely (Figure 4.5b) showed a lower scattering in the spring constant, although the error was still ~ 10%. The cantilever with PDMS between beam and clamps (Figure 4.5c)

showed reproducible spring constants. An exemplary calibration measurement of the spring constant is shown in Figure 4.6.

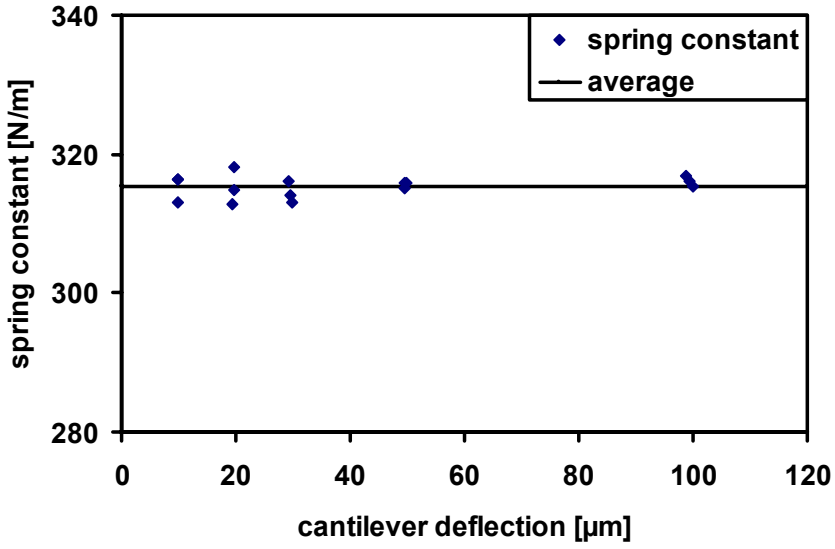

Figure 4.6: Spring constant measurement of a double-clamped cantilever with PDMS between glass beam and clamps. The average spring constant is 315.3 N/m ± 1.6 N/m.

To determine long term stability of the set-up, measurements were performed overnight without movement of the six-axis table or the piezo and without contact of the cantilever. The results are shown in Figure 4.7. To determine the noise of MAD, a measurement was taken for several minutes without contact of the cantilever. An exemplary graph is shown in Figure 4.8.

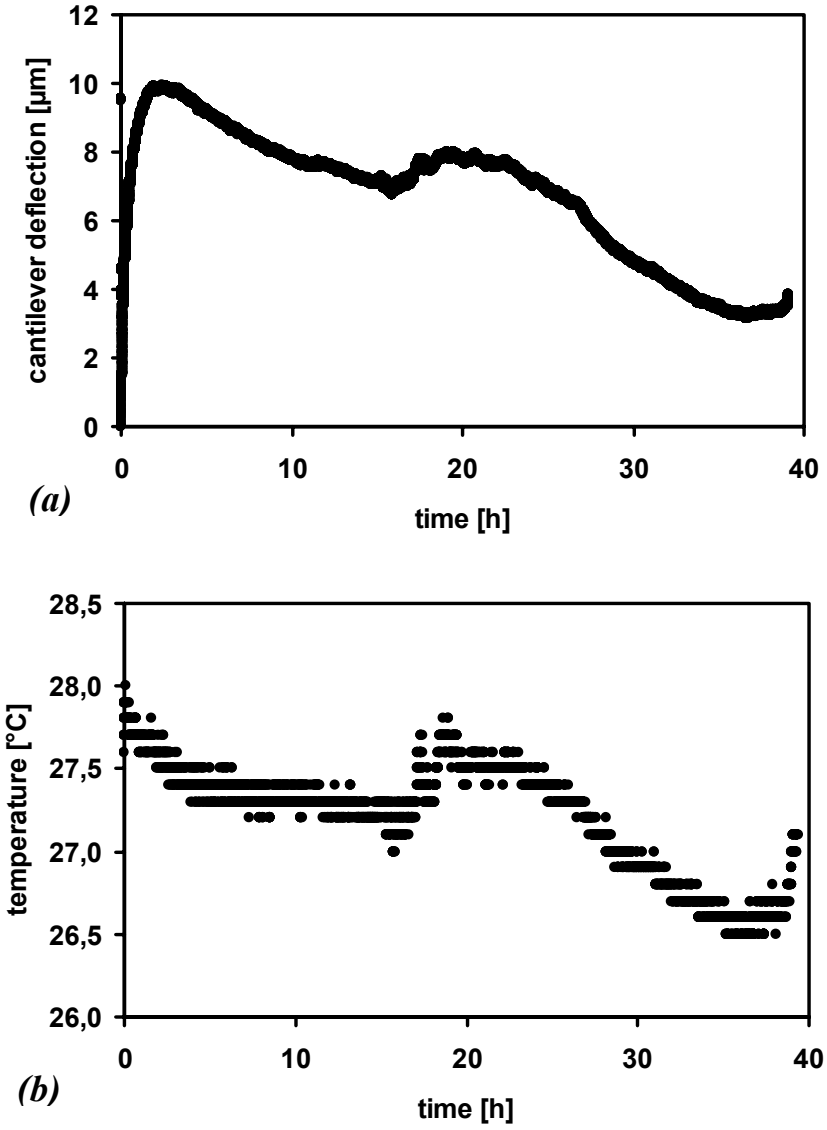

Figure 4.7: Long term experiment for detection of cantilever stability. The cantilever deflection changes significantly after mounting the cantilever holder (a). Afterwards, changes in deflection are detected, which correlate with the temperature (b).

As MAD was designed for flat probe measurements with controlled tilt angle, an angle scan using a flat borosilicate probe with 1 mm diameter on a flat PDMS sample was performed, see Chapter 3 for details of the sample fabrication. The dependences of pull-off force on preload and tilt angle are shown in Figure 4.9. A thorough study of flat probe measurements on flat and patterned PDMS samples is presented in Chapter 6.

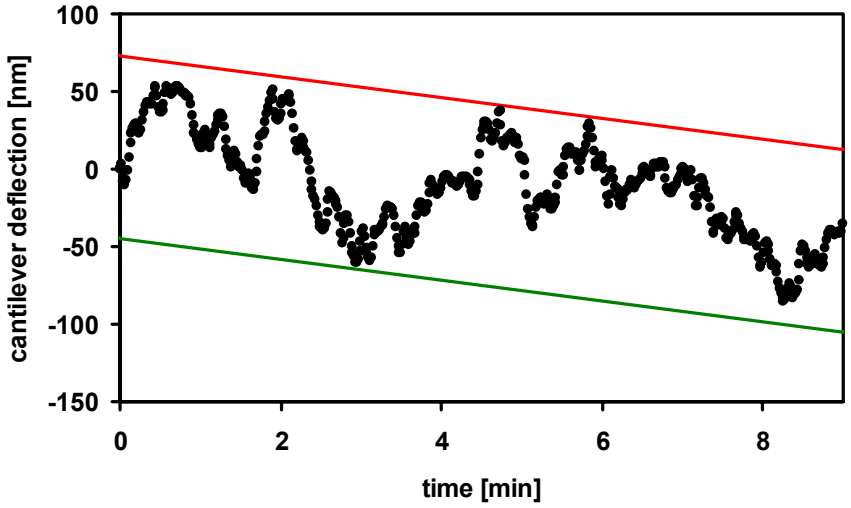

Figure 4.8: Noise of the cantilever during 9 minutes measurement time. The red line shows the upper and the green line the lower limit. The difference between these limits is ~ 120 nm, the slope is ~ 110 nm/h.

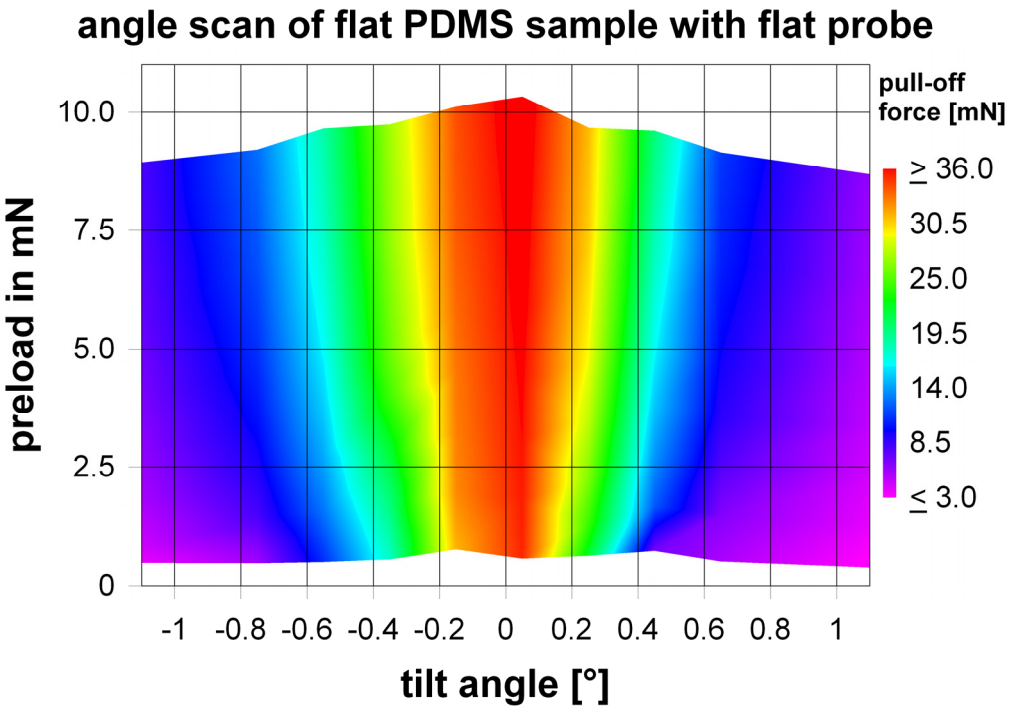

Figure 4.9: Angle scan with a flat probe on a flat PDMS sample. The x-axis shows the tilt angle, the y-axis the applied preload and the pull-off force is color coded.

As measurements with flat aligned probes result in a preload independent contact area, new data analysis procedures are possible. Figure 4.10 shows an exemplary data analysis of an adhesion measurement with an aligned borosilicate glass flat probe (1 mm diameter) on a flat PDMS sample. The values were calculated using cantilever and piezo displacement, probe dimensions, spring constant and sample thickness.

Figure 4.10a shows the original force displacement graph. The velocity of the cantilever during measurement is shown in Figure 4.10b. This graph gives additional information on the contact formation and the pull-off event. During the approach the cantilever velocity shows a slightly positive value (upwards deflection) before a sharp peak is observed at 240 µm displacement. After this peak, the velocity of the cantilever jumps to an almost constant value of ~ 4 µm/s. During retraction a constant velocity is observed until a piezo displacement of approximately 84 µm, where the velocity changes and detachment occurs.

Using force data (Figure 4.10a), indentation depth (difference between piezo displacement and cantilever deflection) and sample thickness, the stress (Figure 4.10c) and strain (Figure 4.10d) and thus, the Young's Modulus (Figure 4.10e) were calculated. All significant data is summarized in Figure 4.10f.

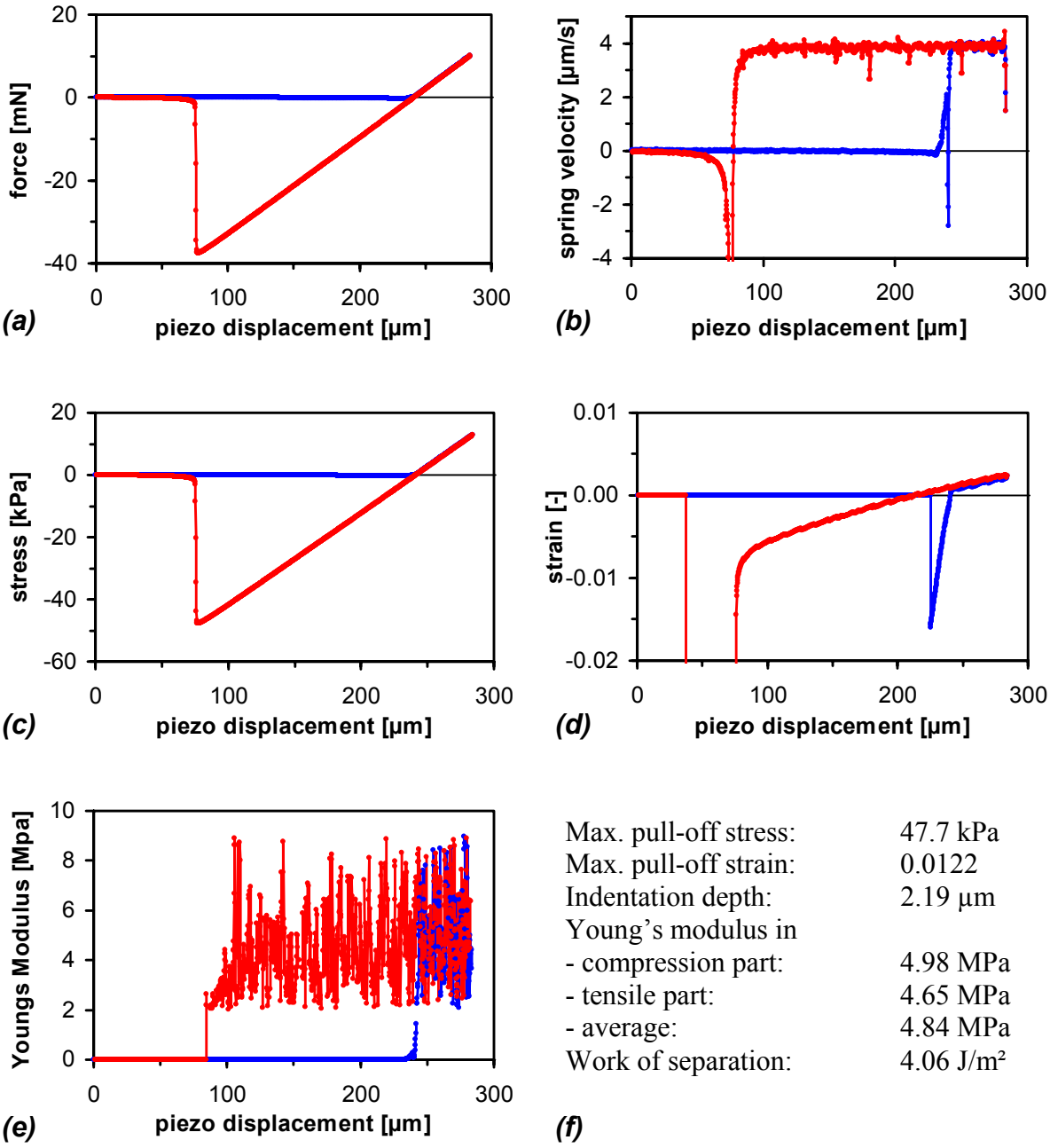

Max. pull-off stress:	47.7 kPa
Max. pull-off strain:	0.0122
Indentation depth:	2.19 µm
Young's modulus in	
- compression part:	4.98 MPa
- tensile part:	4.65 MPa
- average:	4.84 MPa
Work of separation:	4.06 J/m²

(f)

Figure 4.10: Data analysis of an adhesion measurement with a flat probe (1 mm diameter) on flat PDMS at 5 µm/s. The blue and red lines show the approach and retraction phase of the adhesion measurement, respectively. (a) shows the force displacement curve, (b) the cantilever velocity, (c) the stress values (calculated using force and contact area), (d) the sample strain (calculated using indentation depth and sample thickness), and (e) Young's Modulus (using (c) and (d)). (f) gives an overview of significant data obtained from a single measurement.

Figure 4.11 (a-c) shows an *in situ* picture sequence of adhesion measurements with a 1 mm diameter flat borosilicate glass probe on a flat PDMS surface during the retraction phase. The probe was in full contact with the PDMS sample (a). Shortly before detachment occurred, Newton rings were observed (b, indicated by arrows). The detachment was initiated in the middle of the contact area, while an outer ring of the probe was still in contact with the sample (c). The detachment line is traced for better visibility.

Figures 4.11 (d-h) show the retraction phase of a contact experiment performed on a patterned surface with pillars of 10 µm diameter and a center-to-center spacing of 20 µm. In the beginning of the retraction phase the probe was in full contact with the sample (d). As soon as the contact was under tensile force some pillars detached, which can be seen as dark areas in the contact zone (e). With increasing tensile force, more pillars detached (f). Shortly before detachment (h), the adhering pillars exhibit the highest contrast (g).

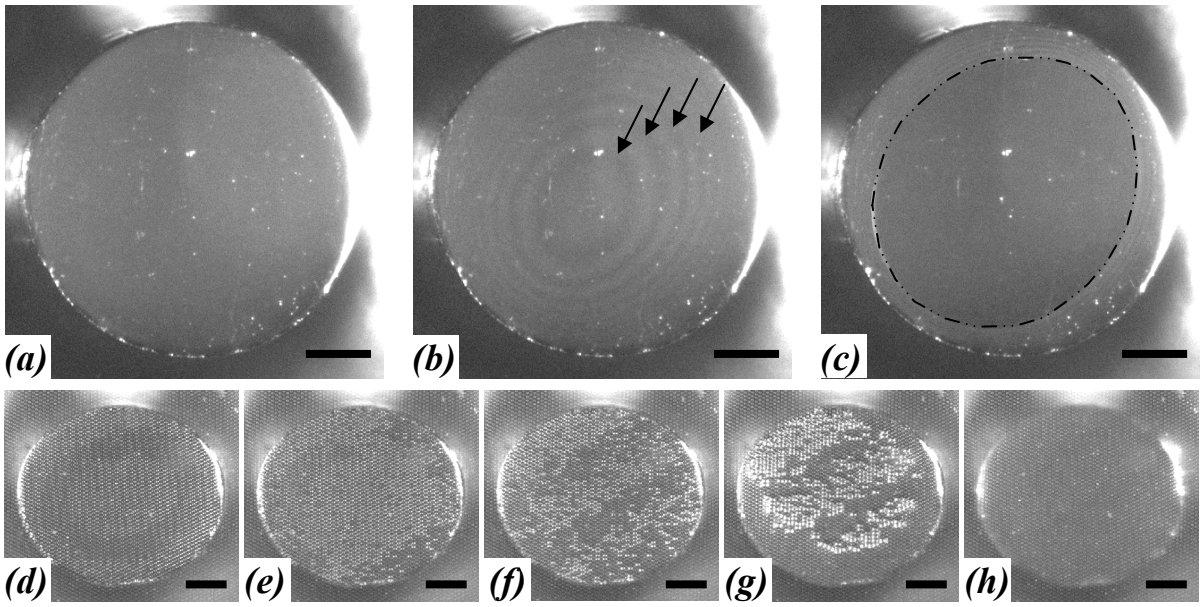

Figure 4.11: Detachment phase of a contact experiment with a 1 mm diameter glass probe on a flat and a patterned sample by viewing through the sample. (a)-(c) show the detachment from a flat PDMS sample and (d)-(h) the detachment from a patterned sample. Pictures were taken by D. Paretkar. The black bar corresponds to 200 µm.

4.4 Discussion

After designing MAD, building up the hardware and programming of the software, the main focus of optimizing the set-up was the development of an optimized cantilever design to ensure a stable system with high resolution and reproducibility.

Although the single-clamped cantilever has many benefits, especially with regard to cantilever mounting, the major drawback of the limited tilt-free deflection of ± 45 µm disqualifies the use of single-clamped cantilevers for measurements with flat probes. However, if small deflections and hence small force ranges are sufficient for the measurements, a single-clamped cantilever may still be utilized.

In the following, the different mounting systems for the double-clamped cantilever are evaluated. As neither the metal band cantilever, nor the glass cantilever with one movable end show a sufficiently stable spring constant, these systems cannot be used for adhesion measurements. The cantilever with PDMS between the clamps has a high tilt-free deflection up to ± 500 µm. Within the standard measurement range of 100 µm the spring constant is very stable as shown in Figure 4.6. The standard deviation for the spring constant lies below ± 0.6%. This guarantees a small experimental error for adhesion measurements.

The long-term stability of the set-up is tested by a 40 hours experiment with a non contact cantilever (Figure 4.7). During the first two hours after mounting, a large deflection can be seen. As the cantilever was not freshly prepared, it can be assumed that it takes several hours to relax stresses in the complete system due to mounting of the cantilever holder. After this period of approximately two hours, a change in height is observed, which correlates with the temperature. In addition, a slight drift can be seen. While the shape of the deflection and the

temperature graph look similar, the deflection value is not identical for identical temperatures. For example, after 16 and after 39 hours, the temperature is nearly the same, but the deflection shows a difference of approximately 2.5 μm. This indicates a general drift of 110 nm/h. The value for the drift and the temperature dependence of the deflection are low and will certainly not affect standard measurements, which take less than a few minutes. However, this change in deflection has to be taken into account for long term experiments or very slow measurements.

To guarantee high resolution, the noise of the set-up was determined for a 9 minute long measurement with a non contact cantilever. The peak to valley value is 120 nm. If this is related to a deflection of ± 300 μm, MAD covers a force range of more than three orders of magnitude without changing the cantilever. Finally, the results in Figure 4.9 demonstrate that angle dependent adhesion measurements can be performed. The results will be discussed in Chapter 6.

Based on measurements with flat aligned probes, new data analysis is possible. Figure 4.10a shows a force displacement graph, which differs from typical measurements obtained by JKR-type experiments; while adhesion measurements with spherical probes usually exhibit a hysteresis in the compressive part of the adhesion measurement and more rounded features during pull-off, the flat punch measurement shows neither of them. This may be explained by the absence of peeling effects, which will always be present for spherical probes.

The velocity data as shown in Figure 4.10b gives deeper insight into contact formation and the pull-off event. The change in velocity during contact formation can be explained as follows. The cantilever approaches the sample and forms contact with it, which will result in a

slightly positive cantilever deflection. However, due to surface roughness or foreign particles, no firm contact will form between the two surfaces. After increasing the pressure slightly, the force is high enough to either compress the roughness or indent the particles into the soft sample. A larger contact area between the two surfaces will form. Then we observe a pull-in, where the probe is sucked into the sample due to adhesive interactions, causing the negative peak in the blue curve of the velocity graph. After this peak, the velocity of the cantilever increases to a constant value, which is lower than the testing velocity (5 µm/s) due to the compression of the sample. Note that following this interpretation we see a "pull into contact" (contact formation before pull-in) of the probe rather than a "jump into contact" (probe jumps into contact due to attractive forces). The constant velocity in the tensile regime of the retraction phase indicates that the sample deforms linear elastically. As soon as the velocity changes, the detachment process begins. Based on the acquired data, many parameters can be determined without applying any contact theories, for example calculation of stress and strain data as well as the Young's Modulus (Figure 4.10f). There exist other testing methods which may allow a more precise measurement of these data. However, the advantage of this procedure is that all data is acquired within a single measurement, which is time saving and leads to an identical experimental error of the results.

An additional comment has to be made about the work of separation. 4.06 J/m² seems to be a large value compared to the surface energy of PDMS, where contact angle measurements and JKR-type experiments usually result in values between 0.042 and 0.044 J/m². (We can assume that the glass surface has the same surface energy as PDMS, because several hundreds of contacts were performed before the measurement (see Chapter 5). However, a similarly high value was observed for a peel-test [27], indicating that the work of separation strongly depends on the measurement method. An explanation of this high work of separation may be

that for a finite flat probe a detachment crack needs to be initiated, while JKR-type experiments as well as contact angle measurements both feature “propagating” cracks. This crack initiation process may lead to high values for the work of separation. This hypothesis is strengthened by the *in situ* observation of the contact, where the detachment occurs in the center of the contact area for a flat aligned probe on flat PDMS (Figure 4.11c). This indicates a different detachment mechanism from crack propagation from the outside of the contact area, which is typically found for spherical contacts. Finally, the picture sequences in Figure 4.11 show that *in situ* visualization allows determination of the real contact area as well as investigating detachment mechanisms.

4.5 Conclusion

A new adhesion tester was designed which has the following measurement properties:

- low noise of ± 60 nm
- high force resolution (dependent on spring constant)
- high maximum deflections of at least ± 300 µm
- over three orders of magnitude force range with one cantilever
- low drift of approximately 110 nm/h
- only slight temperature dependence of the deflection due to thermal expansion
- measurements with controlled alignment

In addition, *in situ* visualization of the contact area and in plan view and side view is possible with a vertically mounted optic system.

4.6 References

[1] Davies, J.; Haq, S.; Hawke, T.; Sargent, J. P. *Int. J. Adhes. Adhes.* **2009**, *29*, 380–390.

[2] del Campo, A.; Greiner, C.; Arzt, E. *Langmuir* **2007**, *23,* 10235-10243.

[3] Gorb, S.; Varenberg, M.; Peressadko, A.; Tuma, J. *J. R. Soc. Interface* **2007**, *4*, 271-275.

[4] Greiner, C.; Arzt, E.; del Campo, A. *Adv. Mater.* **2009**, *21*, 479–482.

[5] Jeong, H. E.; Lee, J.-K.; Kim, H. N.; Moon, S. H.; Suh, K. Y. *Proc. Nat. Acad. Sci.* **2009**, *106*, 5639-5644.

[6] Kim, S.; Sitti, M. *Appl. Phys. Lett.* **2006**, *89*, 261911.

[7] Lee, J.; Bush, B.; Maboudian, R.; Fearing, R. S. *Langmuir* **2009**, *25*, 12449–12453.

[8] Murphy, M. P.; Aksak, B.; Sitti, M. *small* **2009**, *5*, 170–175.

[9] Murphy, M. P.; Kim, S.; Sitti, M. *Appl. Mater. Interface* **2009**, *1*, 489-855.

[10] Aksak, B.; Murphy, M. P.; Sitti, M. *Langmuir* **2007**, *23,* 3322-3332.

[11] Crosby, A. J.; Hageman, M.; Duncan, A. *Langmuir* **2005**, *21,* 11738-11743.

[12] Glassmaker, N. J.; Jagota, A.; Hui, C.-Y.; Noderer, W. L.; Chaudhury, M. K. *Proc. Natl. Acad. Sci. U. S. A.* **2007**, *104*, 10786.

[13] Greiner, C.; del Campo, A.; Arzt, E. *Langmuir* **2007**, *23,* 3495-3502.

[14] Johnson, K. L.; Kendall, K.; Roberts, A. D. *Proc. R. Soc. Lond. Ser. A.* **1971**, *324*, 301-313.

[15] Kim, S.; Aksak, B.; Sitti, M. *Appl. Phys. Lett.* **2007**, *91*, 221913.

[16] Kim, S.; Sitti, M.; Xie, T.; Xiao, X. *Soft Matter* **2009**, *5*, 3689–3693.

[17] Murphy, M. P.; Aksak, B.; Sitti, M. *J. Adhes. Sci. Technol.* **2007**, *21*, 1281–1296.

[18] Peressadko, A.; Gorb, S.; *J. Adhes.* **2004**, *80*, 1–15.

[19] Vajpayee, S.; Long, R.; Shen, L.; Jagota, A.; Hui, C.-Y. *Langmuir* **2009**, 25, 2765-2771.

[20] Glassmaker, N. J.; Jagota, A.; Hui, C. Y. *Acta Biomater.* **2005**, *1*, 367.

[21] Glassmaker, N. J.; Jagota, A.; Hui, C. Y.; Kim, J. *J. R. Soc. Interface* **2004**, *1*, 23.

[22] Hui, C. Y.; Glassmaker, N. J.; Tang, T.; Jagota, A. *J. R. Soc. Interface* **2004**, *1*, 35.

[23] Liu, J.; Hui, C.-Y.; Shen, L.; Jagota, A. *J. R. Soc. Interface* **2008**, *5*, 1087.

[24] Thomas, T.; Crosby, A. J. *J. Adhes.* **2006**, *82*, 311.

[25] Guidoni, G. M.; Schillo, D.; Hangen, U.; Castellanos, G.; Arzt, E.; McMeeking, R. M.; Bennewitz, R. *J. Phys. Mech. Solids* **2010**, *58*, 1571-1581.

[26] Varenberg, M.; Peressadko, A.; Gorb, S.; Arzt, E.; Mrotzek, S. *Rev. Sci. Instr.* **2006**, *77*, 066105.

[27] Thomas, T.; Crosby, A. J. *J. Adhes.* **2006**, *82*, 311.

5. Repeated Adhesion Measurements

Abstract – To mimic the adhesive effects of gecko toes, artificial surfaces have been manufactured recently using polydimethylsiloxanes (PDMS). However, the effects of repeated contacts on the adhesive properties remain largely unexplored. In this paper we report on the effect of repeated pull-off force measurements on the adhesion behavior of PDMS (polymer kit Sylgard 184, Dow Corning). A decrease in pull-off force with increasing number of test cycles is found until a plateau is reached. The initial value and the rate of change in pull-off force strongly depend on the sample preparation procedure, including curing time and cross-linking. It is proposed that the behavior is due to steady coverage of the probe with free oligomers. The results are crucial for developing reusable, durable and residue-free bioinspired adhesives.

This is the pre-peer reviewed version of the following article:

Adhesion Characteristics of PDMS Surfaces During Repeated Pull-Off Force Measurements, Kroner, E.; Maboudian, R.; Arzt, E. *Adv. Eng. Mater.* **2010**, *12 (5)*, 398-404.

5.1 Introduction

For the fabrication of gecko-inspired adhesives different polymers were patterned recently to form complex and sometimes hierarchical geometries [1-11]. Polydimethylsiloxane (PDMS) is one of the most widely used materials for this purpose [1,4,12-21]. Amongst the different PDMS variants, the commercially available kit Sylgard 184 (Dow Corning) is often employed. This polymer deforms elastically with the Poisson number of 0.5, is chemically inert, non-toxic and easy to handle. The Young's modulus of the Sylgard 184 two-component system can be varied over more than 2 orders of magnitude (from below 100 kPa up to more than 10 MPa) by changing the cross-linker to pre-polymer ratio. The viscous mixture allows trapped air to diffuse through the material and hardens within several tens of minutes at elevated temperature, which enables Sylgard 184 usage for fabrication methods such as soft molding.

Adhesion measurements on gecko-inspired adhesives were mostly performed using JKR-type experiments [1-3,5,7-9,12,16]. A probe is pressed onto the sample surface with defined preload and velocity, and retracted while measuring the forces. It is known that some polymers tend to transfer uncured oligomers during a contact event [4,8,22-27]. Although there have been indications for changes in the adhesive properties during repeated loading cycles [4,6,8,19,28], these effects were not studied systematically. For ensuring the reliability of future adhesive devices based on the gecko principle, an understanding of the mechanisms behind repeated contact formation is essential, especially with regard to reusability and residue-free detachment. In this paper, we report on the influence of repeated pull-off force measurements on adhesive properties of PDMS. It is shown that the pull-off force decreases with increasing number of test cycles until a plateau is reached with the rate of change in pull-off force strongly dependent upon the details of sample preparation and testing parameters.

5.2 Experimental

Flat PDMS samples with different curing times and amounts of cross-linker were fabricated by soft-molding on silicon wafers with different surface states. Some samples were cleaned with ethanol and dried shortly before the adhesion testing. After sample preparation the pull-off force was measured upon repeated contact. The next subsection contains the details of the sample fabrication, and in the following subsection the adhesion testing is described.

5.2.1 Sample fabrication

Flat Sylgard 184 PDMS samples were fabricated as follows. The pre-polymer was mixed with the cross-linker in a 10:1 ratio. Gas bubbles due to mixing were eliminated by evacuating the mixture in a desiccator. The viscous liquid was then poured on silicon (100) wafers (provided by Crystec GmbH, Germany), resulting in PDMS samples with a thickness of ~ 1 mm. The silicon wafers were used as purchased with no pretreatment apart from rinsing in acetone for several minutes and drying in air (referred as “fresh” in the following text). To study the effect of the wafer history, some wafers that had been used for sample preparation before were reused without intermediate cleaning.

To ensure identical polymer composition and wafer surface state, pieces of PDMS were demolded from the same wafer after different curing times ranging from 4 to 72 hours at 75°C. Pull-off forces were measured on the sample side facing the wafer immediately after demolding and after ~ 72 hours storage at room temperature. To investigate the effect of cross-linking density, samples were fabricated with pre-polymer to cross-linker ratio of 5:1, 10:1 and 20:1, and cured for 72 hours, which was expected to result in a fully cured polymer according to the data sheet for Sylgard 184.

To examine the effect of uncured oligomers, PDMS samples with 10:1 pre-polymer to cross-linker ratio, prepared as described above and cured at 75°C for 72 hours, were cleaned in a continuous ethanol flow to remove uncured oligomers within the surface region. Ethanol, evaporated in a reservoir, was condensed in a reaction chamber where the sample was positioned. An overflow allowed excess ethanol to flow back to the reservoir. The samples were then dried in a vacuum chamber at room temperature. Ethanol is a poor swelling agent for PDMS and, thus, allows the oligomers within the surface region to be washed off. Some samples were swelled in ethanol overnight and dried at 75°C under vacuum to investigate possible oligomer diffusion from the bulk to the surface due to increased chain mobility at elevated temperatures. All fabrication details are summarized in Table 5.1 (see page 90).

5.2.2 Adhesion measurements

The pull-off force was measured using a home-built adhesion tester, schematically shown in Figure 5.1a. The samples were positioned using a six-axis table (Hexapod, PI Physik Instrumente, Germany). The measurements were performed by moving the samples with a three-axis piezo scanner (Hexapod, PI Physik Instrumente, Germany) which was mounted directly onto the 6-axis table. For the adhesion measurements the sample was brought into contact with a probe which was mounted on a glass cantilever (spring constant 276.9 ± 1.4 N/m). The cantilever deflection was measured using a laser interferometer (Miniatur-Interferometer SP120, SIOS GmbH, Germany) with an accuracy of +/- 50 nm. By calibrating the cantilever, forces were calculated from the deflections due to the linear force-deflection behavior. The systematic error of the adhesion tester lies within the symbols in the graphs.

A representative example of an adhesion measurement is plotted in Figure 5.1b. For all measurements reported here, the probe was a borosilicate glass sphere (J. Hauser & Co. KG,

Germany) with a diameter of 4 mm and a root-mean-square roughness of less than 3 nm. Temperature and humidity were recorded during all measurements and were in the range of 25.5°C to 27.0°C and 27% to 42% relative humidity, respectively. The compressive preload was chosen as 2750 ± 200 µN. The test velocity for all measurements was 2 µm/s.

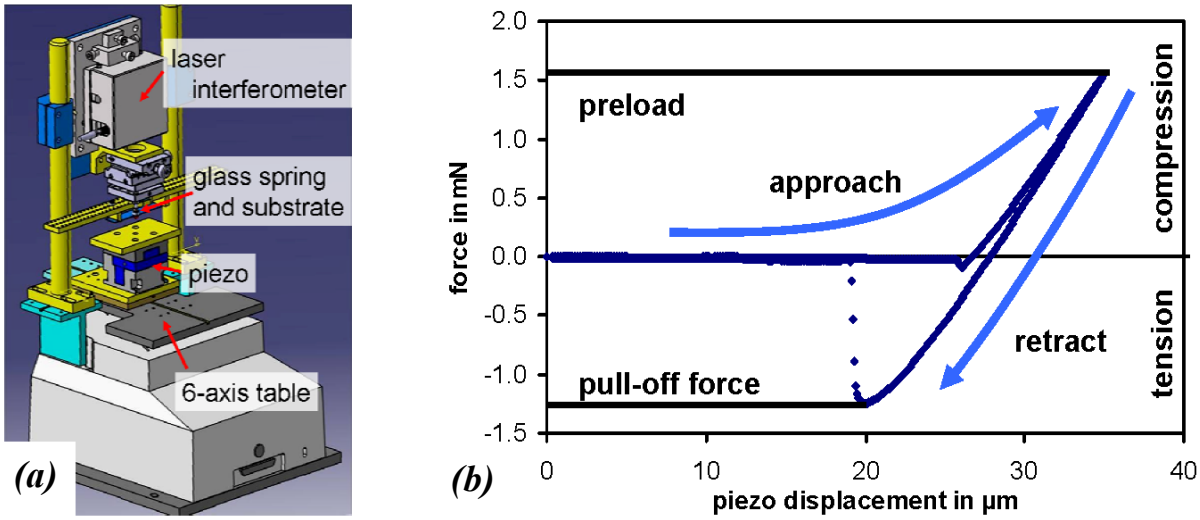

Figure 5.1: (a) Schematic of the home-built adhesion tester. (b) Representative graph of a force-displacement curve. The sample is approached until contact with the probe is formed (pull-in). After applying a preload, the sample is retracted. The probe remains adhered to the sample until a critical force, the pull-off force, is reached and the probe detaches from the sample.

In the following, the term "experiment" is used for a set of measurements performed on the same sample position, while a "measurement" corresponds to one force-displacement curve. Before each experiment, the spherical glass probe was cleaned with ethanol (~96%) and dried in air. Experiments were repeated on the same sample position as well as on different positions.

5. Repeated Adhesion Measurements

The effect of changing the test position on the sample was investigated by first cleaning the glass probe with ethanol and drying, performing several contacts on one position and proceeding to other positions without cleaning the probe in between. On the other hand, experiments were performed on the same sample position but with additional probe cleaning with ethanol and drying after a certain set of measurements. All experimental details are summarized in Table 5.1. Measurements were performed at 2 μm/s testing velocity on flat PDMS samples, which were cured at 75°C.

Table 5.1: Summary of experimental details

experiment	curing time [h]	cross-linker to prepolymer ratio	wafer state	relaxation time [h]
wafer state (Fig. 2c-2d)	4, 8, 16, 24, 48	1:10	fresh [(a)]	0
	4, 8, 16, 24, 48	1:10	used [(b)]	0
curing time (Fig. 2d)	4, 8, 16, 24	1:10	used [(b)]	0
relaxation (Fig. 3a)	72	1:10	fresh [(a)]	0, > 24
cross-linker to prepolymer ratio (Fig. 3b)	72	1:5, 1:10, 1:20	fresh [(a)]	0
cleaning (Fig. 3c)	16, 72	1:10, 1:20	fresh [(a)]	> 24
test position (Fig. 3d)	16	1:10	fresh [(a)]	> 24

(a) fresh = wafer rinsed with acetone for several minutes and dried

(b) used = wafer used for molding before, no cleaning step

5.3 Results

In the next section we present the influence of sample preparation on the adhesive properties, namely the influence of the wafer surface state and the curing time without changing test parameters or material composition. The following section contains results for samples with different time between demolding and adhesion measurement as well as with modified material composition and test parameters, such as changing the pre-polymer to cross-linker ratio, sample cleaning and the dependence of adhesion on test position.

5.3.1 Variations in sample preparation details

Figure 5.2a shows typical graphs for pull-off force vs. number of contact cycles. During the first few contacts, the force dropped significantly and leveled off after several hundreds of contact cycles. Samples with identical pre-polymer to cross-linker ratio but different fabrication histories gave different initial force values. The asymptotic pull-off force value seemed to be the same for these samples, even though the fabrication process differed. Figure 5.2b shows the same data with a logarithmic abscissa, demonstrating linear portions followed by saturation. Figures 5.2c and 5.2d show PDMS samples with 10:1 pre-polymer to cross-linker ratio, cured for different times at 75°C. In Figure 5.2c, the samples were cured on different fresh wafers, while in Figure 5.2d the samples were prepared on wafers that had already been used for several PDMS moldings. The samples cured on fresh wafers showed higher initial pull-off force values and larger force differences between each sample than the samples peeled off from the already used wafers. However, the pull-off forces reached similar values after several hundreds of contacts, independent of the surface state of the wafer.

To ensure identical surface states and thus comparable force values, the PDMS samples in Figure 5.2d were demolded from a single wafer after different curing times. In this case, the

samples which were cured for a short time showed slightly higher forces than the other samples, but the effect was less than 13% for the initial values and within 6% of the values after 250 cycles. As shown in Figure 5.2, all samples displayed a decrease in pull-off force after repeated measurements at the same position. The decrease in pull-off force was less for samples with higher curing times and those prepared on used wafers. The final pull-off force values were comparable in all cases.

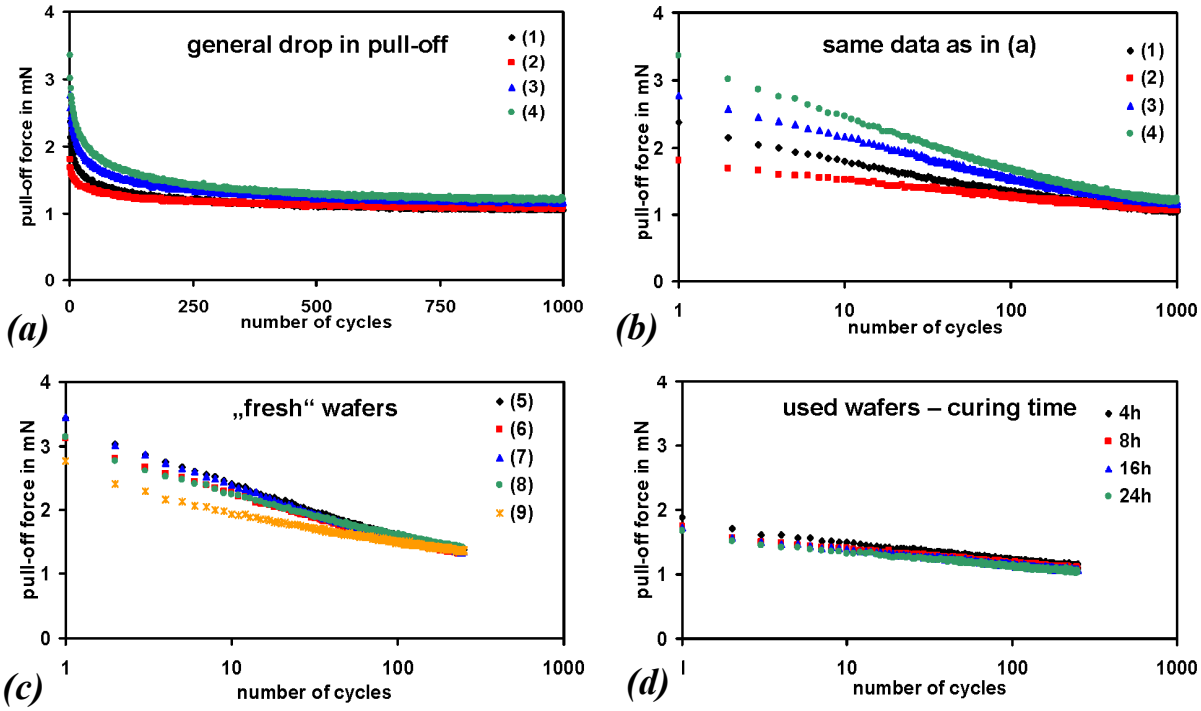

Figure 5.2: Dependence of pull-off force on the number of contact cycles for differently prepared samples, on linear (a) and semi-logarithmic (b-d) plots. All PDMS samples were prepared with 10:1 pre-polymer to cross-linker ratio and cured at 75°C. (a) and (b): different sample preparation lead to differing initial pull-off forces but resulted in comparable forces after ~1000 contacts. (c) and (d): Pull-off forces as a function of measurement cycles for samples peeled off from fresh (c) and already used wafers cured for different times (d) Longer curing times lead to lower pull-off forces. Curing times and wafer history for samples (1) to (9), respectively: 4h, used; 8h, used; 16h, used and cleaned 24h, fresh; 4h, fresh; 8h, fresh; 16h, fresh; 24h, fresh; 48h fresh.

5.3.2 Variations in material and test parameters

Samples which were measured immediately after demolding showed a different adhesive behavior than samples tested after storage at room temperature (Figure 5.3a), namely the initial force values directly after demolding were much higher than those after 72 hours of storage. However, the pull-off forces converged after ~300 cycles (~8 hours) to about the same value. The experiment was repeated after another 72 hours on the same sample, resulting in identical values as after 72 hours of storage.

The effect of pre-polymer to cross-linker ratio was investigated by preparation of PDMS with ratios of 5:1, 10:1, and 20:1, keeping the curing time and temperature fixed at 72 hours and 75°C, respectively. The results are shown in Figure 3b. With increasing cross-linker concentration, the pull-off force was found to decrease. While the 10:1 and 5:1 samples showed similar slopes in the logarithmic plot, the 20:1 sample approached this slope only after ~100 cycles. The force values did not converge to the same value after 1000 cycles, but were higher for lower cross-linker concentrations (Figure 5.3b).

The samples cleaned in a continuous ethanol flow and dried in vacuum at room temperature showed no dependence of the pull-off force on the number of cycles. However, if the samples were swelled in ethanol overnight and dried in an oven at 75°C, a drop in pull-off force was observed, as shown in Figure 5.3c, although the effect was less pronounced than on the sample without this procedure.

Experiments were performed on different sample positions without cleaning the probe in between to investigate whether the observed effects originated from a change in the sample or the probe properties. Figure 5.3d represents an experiment started with a cleaned probe.

During the experiment on the first position the pull-off force dropped. After changing the contact position, the new pull-off force was generally higher than the last measurement point, but lower than the initial pull-off force on the previous position. However, after 1000 contacts no further change in pull-off force was observed by changing the sample position. Both experiments were performed more than 24 hours after demolding and similar effects were measured for all samples tested.

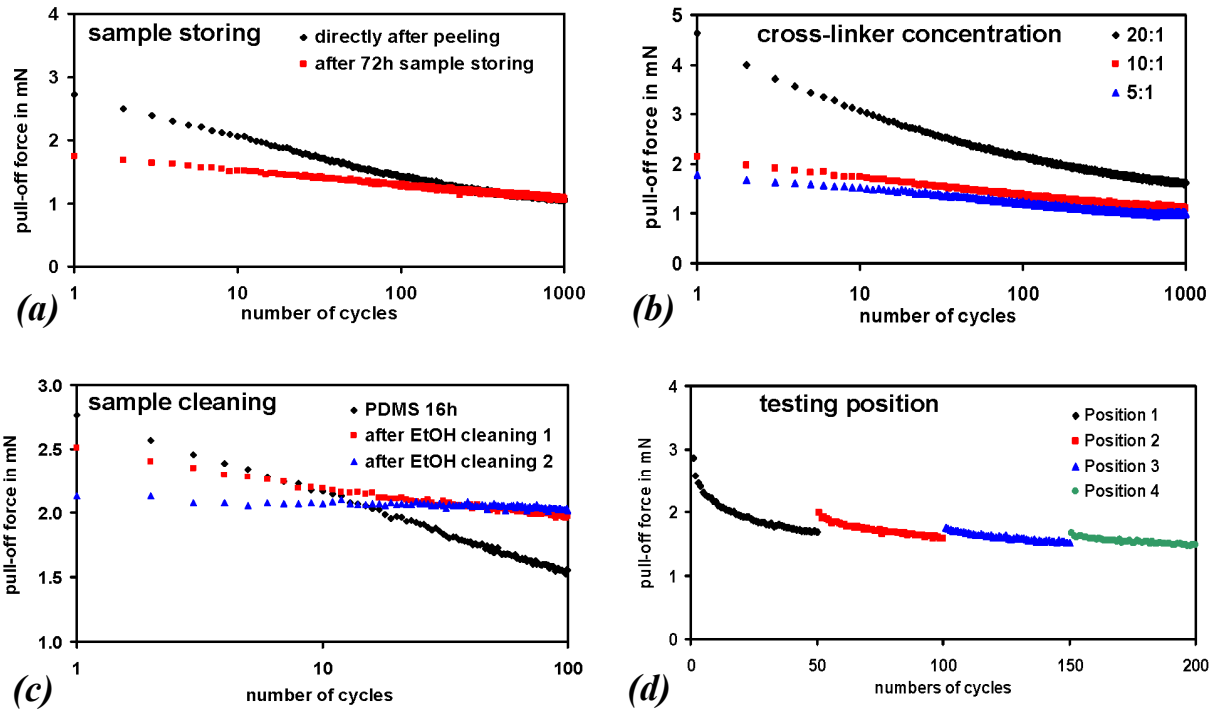

Figure 5.3: Influence of different testing parameters on adhesion. All PDMS samples were cured at 75°C. (a) Pull-off force vs. number of cycles on a sample cured for 72 hours directly after demolding and after a storage time of 72 hours. Measurement velocity was 1 µm/s. (b) Dependence of pull-off force on the ratio of pre-polymer to cross-linker for 20:1, 10:1, and 5:1 mixtures, cured for 72 hours. (c) Pull-off force vs. number of cycles on 10:1 PDMS sample, cured for 16 hours, tested before and after washing in a continuous ethanol flow and drying at 75°C in a vacuum oven. (d) Effect of changing sample position on the pull-off force on a sample cured for 16 hours.

Based on the results presented in this subsection, the pull-off force was found to decrease more strongly for lower cross-linker concentrations and before ethanol cleaning. With change in the measurement location, the pull-off forces recovered, but did not reach the initial value. With increasing number of contacts the force recovering decreased until no effect was measurable.

5.4 Discussion

The results presented above demonstrate that repeated adhesion testing on PDMS (Sylgard 184) influences the pull-off force. If the experiment starts with a cleaned probe, the pull-off force drops significantly during the first few measurements and levels off after several hundreds of contact cycles (Figure 5.2a). If the pull-off force is plotted logarithmically against the number of cycles (Figure 5.2b), a linear decrease is observed initially which eventually reaches a plateau. The y-axis intercept and the slope of the linear portion of the graphs differ depending on the sample preparation details and testing parameters, signaling changes in the surface properties. An important set of questions is whether the probe or the sample properties change, what the nature of the change is and why this effect levels off after a certain number of contacts.

5.4.1 Proposed mechanism for the change in pull-off force

We assume that the probe is well cleaned before the experiment, while the sample contains free oligomers in the surface region (Figure 5.4a). During the first contact, we propose that some free oligomers are pulled out from the sample and transferred to the probe (Figure 5.4b), which is known to raise the pull-off force [29-30]. In some studies it is found that grafted polymers enhance the adhesion as well [31], which could be a similar effect here. The pull-off force for the second contact may differ from the previous one for two possible reasons:

(i) macroscopically, the surface energy of the probe may now be lower due to the coverage with PDMS oligomers (Figure 5.4c); (ii) microscopically, the number of transferable oligomers has changed, influencing their physical interactions. It is expected that new oligomers diffuse from other areas of the surface or from the bulk to the testing position, leading to a time dependent reformation of the original surface state; at the same time, oligomers are transferred from the probe back to the sample. After a certain number of cycles, this exchange may lead to a dynamic equilibrium state and thus, no further change in the pull-off force occurs (Figure 5.4d). If the effect of change in the surface energy of the probe dominates, the pull-off force of the following contacts will be lower; increased force values for subsequent contacts may be expected if the physical oligomer or polymer chain-chain interactions are dominant.

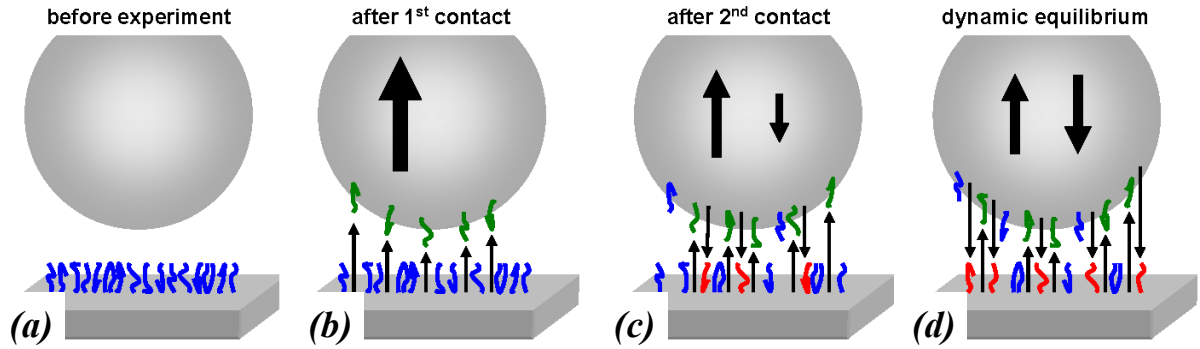

Figure 5.4: Schematics of the proposed mechanism for the decrease in pull-off force upon repeated contact, i. e. oligomer transfer between the sample and probe during contact formation: (a) system before the measurement with a clean probe and a sample covered with free oligomers; (b) situation after the first contact, during which oligomers have been transferred to the probe; (c) after second contact, oligomers have been transferred to the probe and back-transfer to the sample occurs; (d) dynamic equilibrium leading to an adhesion force plateau. The arrows in the probes indicate schematically the extent of transferred oligomers from and to the probe.

5.4.2 Effects of sample preparation on adhesive properties

Figure 5.2c and 5.2d show that the surface state of the wafer used for molding plays an important role. Peeling off the sample from a fresh wafer caused a high initial pull-off force, while samples prepared on used wafers showed lower initial force values and a less pronounced decrease. By placing a droplet of water on the wafers it could be seen that the water contact angle was higher on the used wafer which indicates that some PDMS or uncured oligomers were left behind on the wafer surface upon demolding. The presence of uncured oligomers on the wafer would change the surface properties of the sample after demolding from a used wafer due to a higher concentration of free oligomers and thus the initial force values obtained by the adhesion measurement, as described in the hypothesis above.

The samples cured for short time showed slightly higher pull-off forces than the samples cured for longer time (Figure 5.2d). This is to be expected, as less cross-linking due to incomplete curing leaves a higher concentration of free oligomers; their pull-out may lead to higher initial pull-off force values. This effect was only observed for samples removed at different curing times from the same wafer, as the effect of the wafer surface state overshadows the curing effect.

5.4.3 Effects of Sample Modification and Testing Parameters on Adhesive Properties

Sample storage after demolding strongly decreased the initial pull-off force but gave similar values after several hundred contact cycles (Figure 5.3a). It is likely that demolding creates a "non-equilibrium" surface which undergoes a structural relaxation during storage, influencing the pull-off force values. The larger drop in pull-off force with decreasing cross-linker concentration (Figure 5.3b) is also consistent with our hypothesis. Due to a higher

concentration of free oligomers on the sample surface, the probe coverage would be the dominant process. The high initial force values can be explained by the large number of free oligomers being pulled-out upon contact. Earlier studies have shown similar effects for polyurethane and other materials as well [4,6,8,19].

The hypothesis is also in agreement with the smaller force drop in the pull-off force measured for cleaned samples. Fully cleaned PDMS supposedly does not contain any uncured oligomers in the surface region, resulting in a constant pull-off force. The sample which was left in ethanol overnight and dried in vacuum at elevated temperature, however, still showed a drop in pull-off force, although less pronounced (Figure 5.3c). This suggests that heating may have enhanced the diffusion of oligomers from the bulk to the surface. Therefore, the initial pull-off force was lower followed by a smaller drop in pull-off force upon repeated contact. Cleaning by swelling seems to have removed enough oligomers from the sample surface to affect the surface coverage during measurements as well as the pull-out effects of the free oligomers.

The sample position effect in Figure 5.3d is also consistent with our mechanism. The decrease in the initial pull-off force value for each new position then represents the change in the probe surface properties, while the force values without the position change represent the surface change of both the sample and the probe. After 1000 cycles the pull-off force was insensitive to position changes within the measurement accuracy. This is in agreement with our hypothesis that the probe and the sample have reached equilibrium states.

Overall, the results of this paper highlight that the adhesion forces of PDMS against glass may evolve with repeated cycles. While our hypothesis seems to explain the overall effects, its

exact molecular details still need to be investigated. It is however clear that this effect limits the ability to compare data from different sources. One way to address this issue may be to clean the PDMS samples carefully before measurement to ensure an oligomer-free sample surface. This, however, may lead to different elastic properties due to swelling-induced polymer network damage and a complicated sample fabrication method. Alternatively, the plateau value after several hundred cycles may be taken as a representative value. Ultimately, the specific application envisioned will determine which parameter is more appropriate. This is particularly true for micropatterned surfaces which, based on our preliminary studies, also exhibit an adhesion force evolution and will be the subject of future investigation.

5.5 Conclusion

Our study shows the effects of repeated adhesion measurements on the pull-off force for differently fabricated PDMS samples. It is observed that:

- The pull-off forces decreased with the number of contacts if the experiment started with a cleaned probe.
- The decrease was higher for samples with shorter curing time and if the samples were prepared by molding on fresh wafers.
- With higher cross-linker concentration the drop in pull-off force became less pronounced. The same effect was found for samples cleaned in Ethanol.
- With change in the measurement location, the pull-off forces recovered but to a value lower than the initial one.
- For identical material composition the steady state pull-off force after ~ 1000 cycles was identical, independent on the fabrication details or measurement position.

To help explain these observations, we have proposed a mechanism based on gradual coverage of the probe with free oligomers, resulting in dynamic changes in the surface properties of the probe and the sample.

5.6 References

[1] del Campo, A.; Greiner, C.; Arzt, E. *Langmuir* **2007**, *23*, 10235-10243.

[2] Greiner, C.; Arzt, E.; del Campo, A. *Adv. Mater.* **2009**, *21*, 479–482.

[3] Cheung, E.; Sitti, M. *Langmuir* **2009**, *25*, 6613–6616.

[4] Davies, J.; Haq, S.; Hawke, T.; Sargent, J. P. *Int. J. Adhes. Adhes.* **2009**, *29*, 380–390.

[5] Murphy, M. P.; Aksak, B.; Sitti, M. *small* **2009**, *5*, 170–175.

[6] Murphy, M. P.; Kim, S.; Sitti, M. *Appl. Mater. Interf.* **2009**, *1*, 849-855.

[7] Northen, M. T.; Greiner, C.; Arzt, E.; Turner, K. L. *Adv. Mater.* **2008**, *20*, 3905–3909.

[8] Glass, P.; Chung, H.; Washburn, N. R.; Sitti, M. *Langmuir* **2009**, *25*, 6607–6612.

[9] Vajpayee, S.; Long, R.; Shen, L.; Jagota, A.; Hui, C.-Y. *Langmuir* **2009**, *25*, 2765-2771.

[10] Majidi, C.; Groff, R. E.; Maeno, Y.; Schubert, B.; Baek, S.; Bush, B.; Maboudian, R.; Gravish, N.; Wilkinson, M.; Autumn, K.; Fearing, R. *Phys. Rev. Lett.* **2006**, *97*, 076103.

[11] Chandra, D.; Taylor, A. J.; Yang, S. *Soft Matter* **2008**, *4*, 979–984.

[12] del Campo, A.; Greiner, C.; Alvarez, I.; Arzt, E. *Adv. Mater.* **2007**, *19*, 1973–1977.

[13] del Campo, A.; Alvarez, I.; Filipe, S.; Wilhelm, M. *Adv. Funct. Mater.* **2007**, *17*, 3590–3597.

[14] Crosby, A. J.; Hageman, M.; Duncan, A. *Langmuir* **2005**, *21*, 11738-11743.

[15] Pokroy, B.; Epstein, A. K.; Persson-Gulda, M. C. M.; Aizenberg, J. *Adv. Mater.* **2009**, *21*, 463–469.

[16] Greiner, C.; del Campo, A.; Arzt, E. *Langmuir* **2007**, *23*, 3495-3502.

[17] Hui, C.-Y.; Jagota, A.; Shen, L.; Rajan, A.; Glassmaker, N.; Tang, T. *J. Adhes. Sci. Technol.* **2007**, *21*, 1259–1280.

[18] Lee, H.; Lee, B. P.; Messersmith, P. B. *Nature* **2007**, *448*, 338-341.

[19] Glassmaker, N. J.; Jagota, A.; Hui, C.-Y.; Kim, J. *J. R. Soc. Interf.* **2004**, *1*, 23–33.

[20] Glassmaker, N. J.; Jagota, A.; Hui, C.-Y.; Norderer, W. L.; Chaudhury, M. K. *Proc. Nat. Acad. Sci.* **2007**, *104*, 10786–10791.

[21] Thomas, T.; Crosby, A. J. *J. Adhes.* **2006**, *82*, 311–329.

[22] Hale, P. S.; Kappen, P.; Prissanaroon, W.; Brack, N.; Pigram, P. J.; Liesegang, J. *Appl. Surf. Sci.* **2007**, *253*, 3746–3750.

[23] Andersson, L. H. U.; Hjertberg, T. *J. Appl. Polym. Sci.* **2003**, *88*, 2073-2081.

[24] Kim, J.; Park, M.; Chae, G. S.; Chung, I.-J. *Appl. Surf. Sci.* **2008**, *254*, 5266–5270.

[25] Yunus, S.; de Crombrugghe de Looringhe, C.; Poleunis, C.; Delcorte, A. *Surf. Interf. Anal.* **2007**, *39*, 922–925.

[26] Graham, D. J.; Price, D. D.; Ratner, B. D. *Langmuir* **2002**, *18*, 1518-1527.

[27] Glasmastar, K.; Gold, J.; Andersson, A.-S.; Sutherland, D. S.; Kasemo, B. *Langmuir* **2003**, *19*, 5475-5483.

[28] Kroner, E.; Maboudian, R.; Arzt, E. *IOP Conf. Ser.: Mater. Sci. Eng.* **2009**, *5*, 012004, 1-6.

[29] Galliano, A.; Bistac, S.; Schultz, J. *J. Adhes.* **2003**, *79*, 973-991.

[30] Galliano, A.; Bistac, S.; Schultz, J. *J. Colloid Interf. Sci.* **2003**, *265*, 372-379.

[31] Lèger, L. *Macromol. Symp.* **2000**, *149*, 197-205.

6. Flat and Spherical Probes:

A Comparative Study

Abstract – Adhesion measurements on poly(dimethyl)siloxane samples were performed, for the first time, with flat glass probes under controlled tilt angle and the results were compared to measurements from spherical probes of two different radii. Experiments were made on both flat and patterned samples with pillar diameters of 4.7 μm and heights of 0.82 μm and 1.95 μm, respectively. Pull-off forces measured with spherical probes showed the usual preload dependence and were independent of misalignment angle. On the other hand, pull-off forces measured with aligned flat probes were independent of preload, but dropped significantly and became preload dependent with increasing misalignment. This effect was more pronounced for patterned samples, where a misalignment by 0.2° resulted in a drop of adhesion by more than 30%. The comparison indicates that measurements from spherical probes underestimate adhesive forces for patterned surfaces if compared with aligned flat probes. Finally, we propose a simple model which allows the prediction of angle-dependent plateau values of pull-off forces for measurements with flat probes on flat samples.

This chapter is accepted for publication by The Journal of Adhesion:

Adhesion of Flat and Structured PDMS Samples to Spherical and Flat Probes: A Comparative Study, Kroner, E.; Paretkar, D. R.; McMeeking, R. M.; Arzt, E.

6.1 Introduction

Intense investigation of biomimetic adhesives has occurred over the last several years. Surface patterns of increasing complexity have been fabricated, such as simple cylindrical pillars [1-5], hierarchical geometries [6-11], and pillars with defined tilt angles [8, 12-14] and different tip shapes [10, 13-22]. Besides measurements of friction [3,8-9,14,23] or frictional adhesion [22], the most common method for determining normal adhesion is the so-called JKR-type experiment [1-2,4,6,10-13,18-20,24-25], named after *Johnson*, *Kendall* and *Roberts* [26]. In their original work, two soft elastic spheres were brought into contact and area of contact as well as pull-off force was measured [27-28]. The results led to the now well known JKR theory [26] for contact between soft spheres. For practical reasons, the experimental setup nowadays often consists of a hard, spherical probe pressed against a soft, flat sample, and preload and pull-off force are measured [2,10,13,18].

Measurements with spherical probes are insensitive to misalignment and have been investigated theoretically [29-36]; data interpretation, however, has several problems. One of the main drawbacks is the increase of the contact area with increasing compressive preload, which complicates the determination of the pull-off strength. With regard to adhesion of patterned surfaces, additional problems are encountered. For example, the stress state of individual pillars depends on their position within the contact area: while pillars in the contact boundary region are under tension during pull-off, pillars directly below the center of the probe may still be under compression. This leads to a stepwise detachment of pillars [1,6,10,14], which will influence pull-off force values. A possible way to avoid such problems is to measure adhesion with a stiff flat probe against a larger flat, compliant sample [5]. The contact area is then constant and defined by the probe dimensions. Apart from a small region at the probe boundary, a uniform stress within the sample can be achieved. In contrast to

experiments with spherical probes, the use of flat probes allows direct determination of the pull-off strength by simple division of the pull-off force by the area of the probe. However, adhesion measurements with a flat probe require careful parallel alignment of probe and sample to ensure reproducibility of data.

In this paper we present, for the first time, normal adhesion measurements with flat probes under controlled tilt angle, both on flat and patterned samples. The results of these measurements are compared with adhesion data from spherical probes of two different radii. We then propose a model which predicts the angle dependence of the pull-off force plateau at high preload for measurements from flat probes on flat samples.

6.2 Experimental

6.2.1 Sample preparation

Polydimethylsiloxane (PDMS) samples with a hexagonal pillar pattern were fabricated in three process steps: photo lithography, reactive ion etching and two-step soft molding. For photo lithography, silicon wafers (Crystec GmbH, Germany) were spin-coated with the photo resist SU 8-2 (MicroChem GmbH, Germany) to form a layer of 2 µm thickness. After exposure through a lithography mask (ML&C Jena GmbH, Germany) and treatment of the resist with a developer (mrdev-600, MicroChem GmbH, Germany) cylindrical pillars were obtained.

To improve durability and cleanability of the templates, the patterned wafers were etched in a reactive ion etcher using a gas chopping process with SF_6 and CHF_3 as etching gases and CHF_3 as passivation gas. The remaining photo resist was stripped by heating the wafers to 600°C in air. Silicon cylinders with pillar heights being a function of the etching time were obtained.

The silicon wafers were then used as a mold. Two molding steps were necessary to obtain cylindrical polymer pillars. The first molding was performed with polyurethane (PU) (PolyOptic 1470, PolyConForm GmbH, Germany). After cross-linking at room temperature for 48 hours, the PU was peeled off the wafers resulting in polymer molds with cylindrical holes. In the second step the PU molds were used to fabricate PDMS samples with cylindrical pillars. Sylgard 184 PDMS (Dow Corning, UK) was mixed in a 10:1 (pre-polymer to cross-linker) ratio. After removal of air bubbles formed during mixing in vacuum, the viscous liquid was poured onto the PU template and cross-linked at 75°C for 72 hours. After cross-linking the PDMS samples were peeled off the PU template resulting in patterned PDMS samples. Flat PDMS samples were prepared under identical conditions and were used as a control.

6.2.2 Adhesion measurements

Adhesion measurements were performed on a custom-built apparatus known as the Macroscopic Adhesion measurement Device (MAD), as previously described [37,38], see also Chapter 3. Figure 6.1 shows a schematic of the adhesion tester. A three-axis piezo stage (PI Karlsruhe, Germany) was mounted to a six-axis positioning table (PI Karlsruhe, Germany) for high positioning and measurement accuracy. Forces were measured using a calibrated symmetric glass cantilever with tilt-free deflection up to several hundred micrometers. A mirror and the probe were glued to the top and the bottom of the cantilever, respectively. The cantilever deflection was measured using a laser interferometer (SIOS Messtechnik GmbH, Germany). The interferometer is very sensitive to tilt of the mirror and halts measurement if misalignment exceeds 2 arc minutes. Therefore, the intensity of the reflected laser beam served as an indirect control of cantilever tilt.

The sample was pressed against the probe with a defined preload and retracted in a standard load-displacement experiment. The pull-off force was defined as the maximum tensile force. Three different probes were used for adhesion measurements; two borosilicate glass spheres with 2 mm and 5 mm radius and a borosilicate glass flat-ended cylindrical probe having a diameter of 1 mm (peak to valley roughness <15 nm). All adhesion tests were performed at a velocity of 5 µm/s. The probes were cleaned with ethanol and brought into contact with a PDMS piece 1000 times before starting the measurements to ensure an equilibrium surface state of the probe [37], see also Chapter 5.

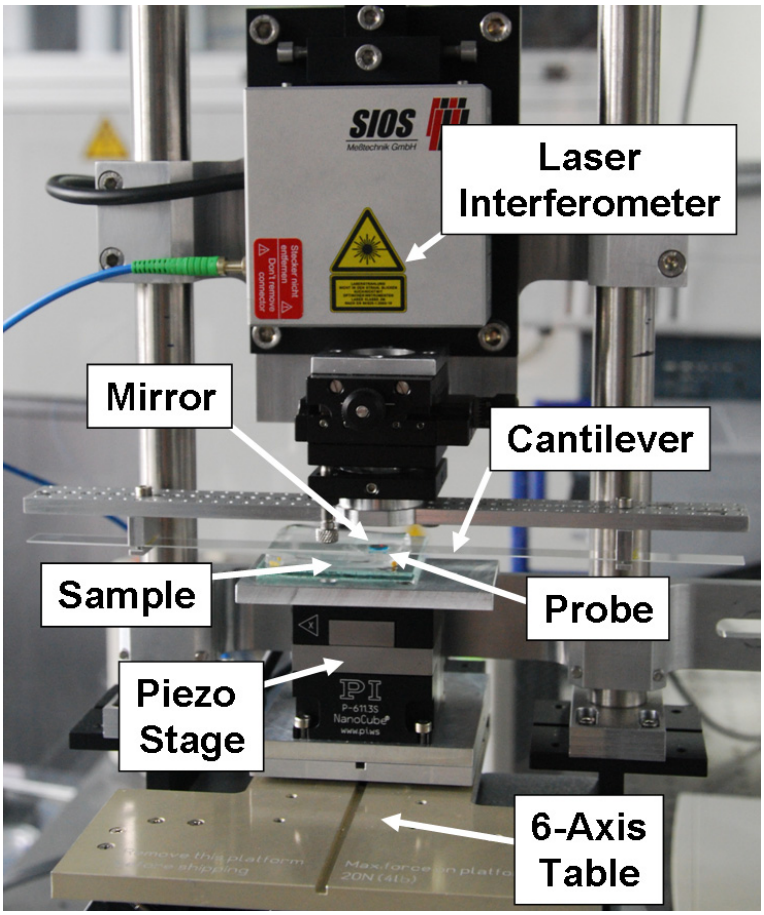

Figure 6.1: Set-up of the adhesion tester MAD. The sample is brought into contact with the probe (glued to the cantilever) using a piezo and a six-axis table. The latter allows high precision tilting. The deflection of the cantilever is continuously measured by laser interferometry. Forces are calculated from the cantilever deflection.

To investigate misalignment effects, the samples tested with the flat probe had to be carefully aligned. Adhesion measurements were performed for different tilt angles with 0.02° accuracy in two axes, resulting in a point symmetric pull-off force profile. The center of the symmetric profile was defined as 0° misalignment. The alignment was then systematically varied from -2° up to +2° in 0.2° steps. Measurements were also performed with spherical probes within ±2° tilt angle, although a definition of 0° misalignment was not possible in this case.

6.3 Results

6.3.1 Sample shape

The patterned PDMS samples were characterized using white light interferometry. The samples consisted of cylindrical pillars with 4.7 ± 0.1 µm diameter and heights of 0.82 ± 0.02 µm (referred as AR0.2) and 1.95 ± 0.02 µm (referred as AR0.4), respectively. These low aspect ratios (AR) were chosen to prevent pillar buckling during loading. The pillars were hexagonally packed with a center-to-center spacing of 10 µm, resulting in a packing density of 20.0%. The sample thickness was ~ 880 µm. The pillars were slightly conical and featured sharp edges. Figures 6.2a and b show a cross section of an AR0.4 pillar measured by white light interferometry and an SEM picture, respectively.

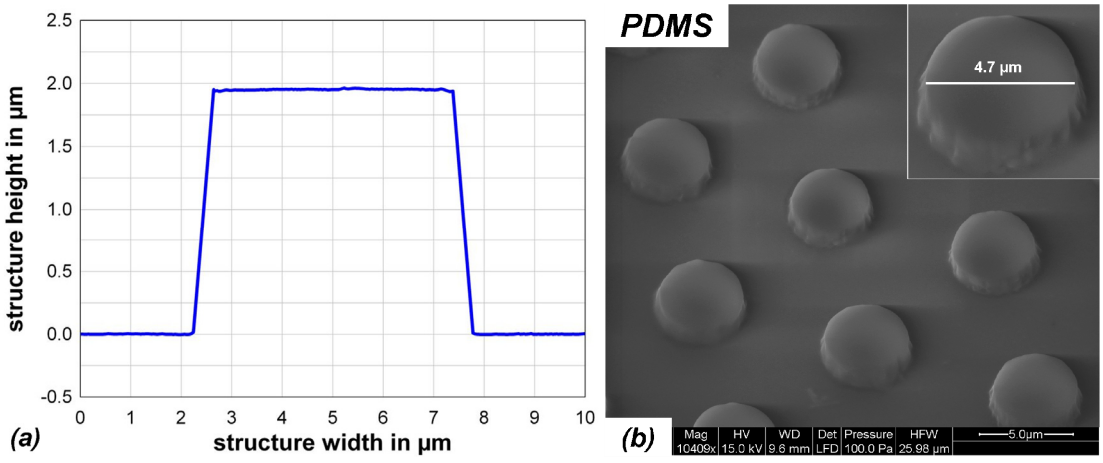

Figure 2: Geometry of pillars with 1.95 µm height and 4.7µm diameter. (a) Cross section measured by white light interferometry of a single pillar. (b) SEM image of the pillars.

6.3.2 Angle dependent adhesion using a flat probe

Adhesion measurements with the flat probe showed a strong dependence of pull-off forces on the tilt angle as shown in Figure 6.3. For measurements in the aligned state, low or no dependence of pull-off force on preload was found for both flat and patterned samples. With increasing tilt angle of the probe, the pull-off force values dropped significantly and became preload dependent. In the case of flat PDMS, 0.2° tilt angle had a negligible preload dependence of the pull-off force but the value of the pull-off force was reduced by ~ 10% compared to aligned measurements (Figure 6.3a). For a misalignment of 0.4°, the pull-off force showed an increased preload dependence. The pull-off force reached ~ 53% for low and ~ 74% for maximum preload, compared to aligned measurements. For a misalignment of 2.0° the pull-off force showed a pronounced preload dependence and constituted less than ~ 10% of the force measured in the aligned state.

The preload and angle dependency of the pull-off force for patterned samples are shown in Figures 6.3b and c. For both aspect ratios the pull-off force dependence on misalignment was higher than for flat control samples. A misalignment of 0.2° was sufficient to result in a significant preload dependence. Compared to force values obtained from aligned experiments, the pull-off forces measured on AR0.2 pillars reached between 16% for low and 64% for high preload (Figure 6.3b). For misalignment > 0.6° the pull-off force did not change further with increasing tilt angle. For AR0.4 pillars the pull-off force showed a similar dependence on misalignment as for AR0.2 pillars, but was less pronounced (Figure 6.3c). A misalignment of 0.2° resulted in pull-off forces between 26% for low and 80% for high preload compared to the value obtained from aligned measurements. In general, the pull-off forces for patterned samples were lower than for flat control samples, as the pillars had relatively large diameters, a low aspect ratio and no adhesion enhancing tip geometry [2,18].

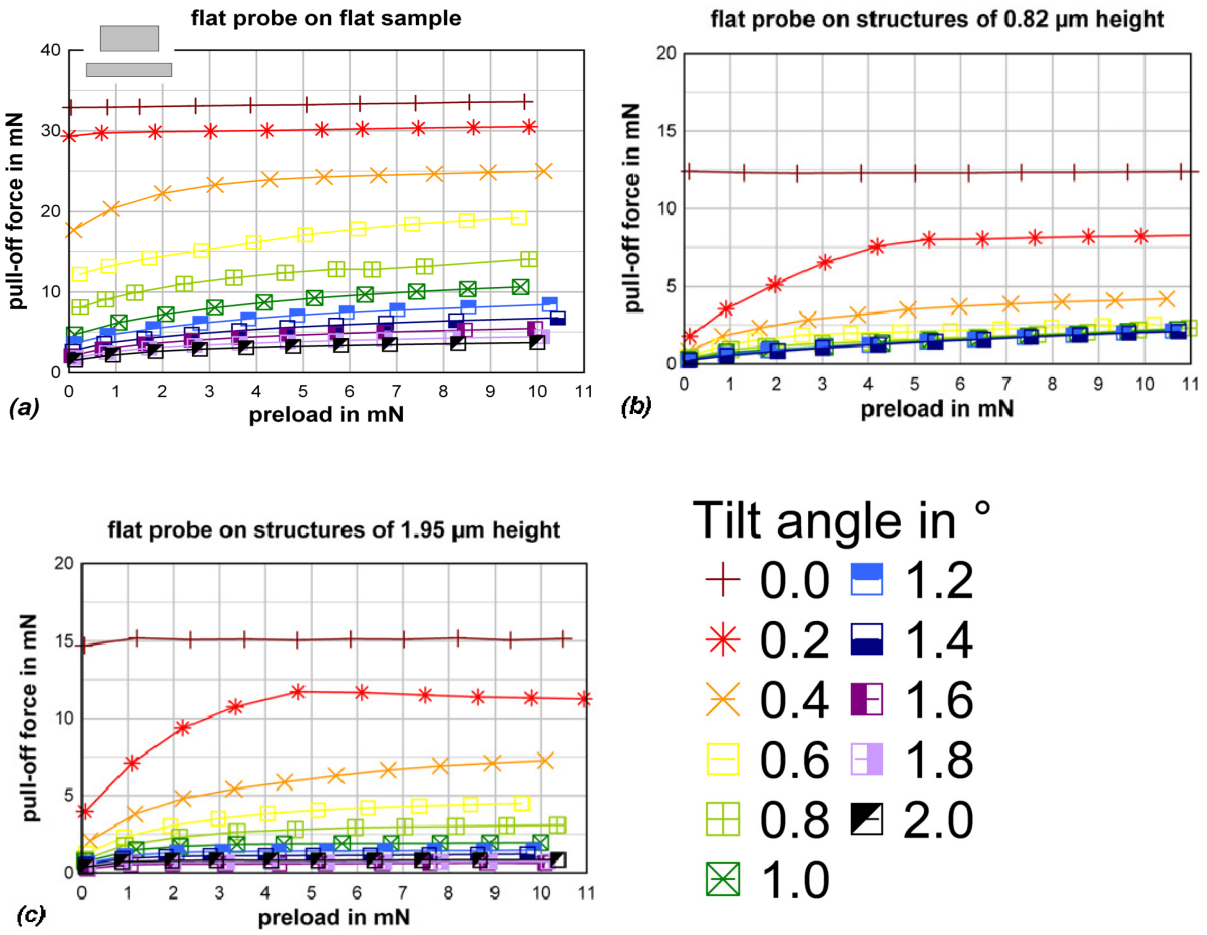

Figure 6.3: Adhesion measurements performed with a flat-ended cylindrical glass probe of 1 mm diameter at different misalignment angles. Angle scans were performed for (a) flat, (b) patterned PDMS samples with a diameter of ~ 4.7 µm and heights of ~ 0.82 µm (AR0.2) and (c) pillars with heights of ~ 1.95 µm (AR0.4).

6.3.3 Comparison between different probe geometries

Figures 6.4a and 6.4b show the results of adhesion measurements from spherical probes (2 mm and 5 mm radii) on flat and patterned PDMS for different tilt angles. For these measurements the tilt angle had no effect on the pull-off force. However, for the 2 mm radius probe a sudden increase in pull-off force was measured for AR0.2 pillars at a preload of ~ 3 mN (Figure 6.4a, green curve). Figure 6.4c shows the results for aligned measurements with a flat probe. Additional measurement graphs are shown in 6.7 Appendix.

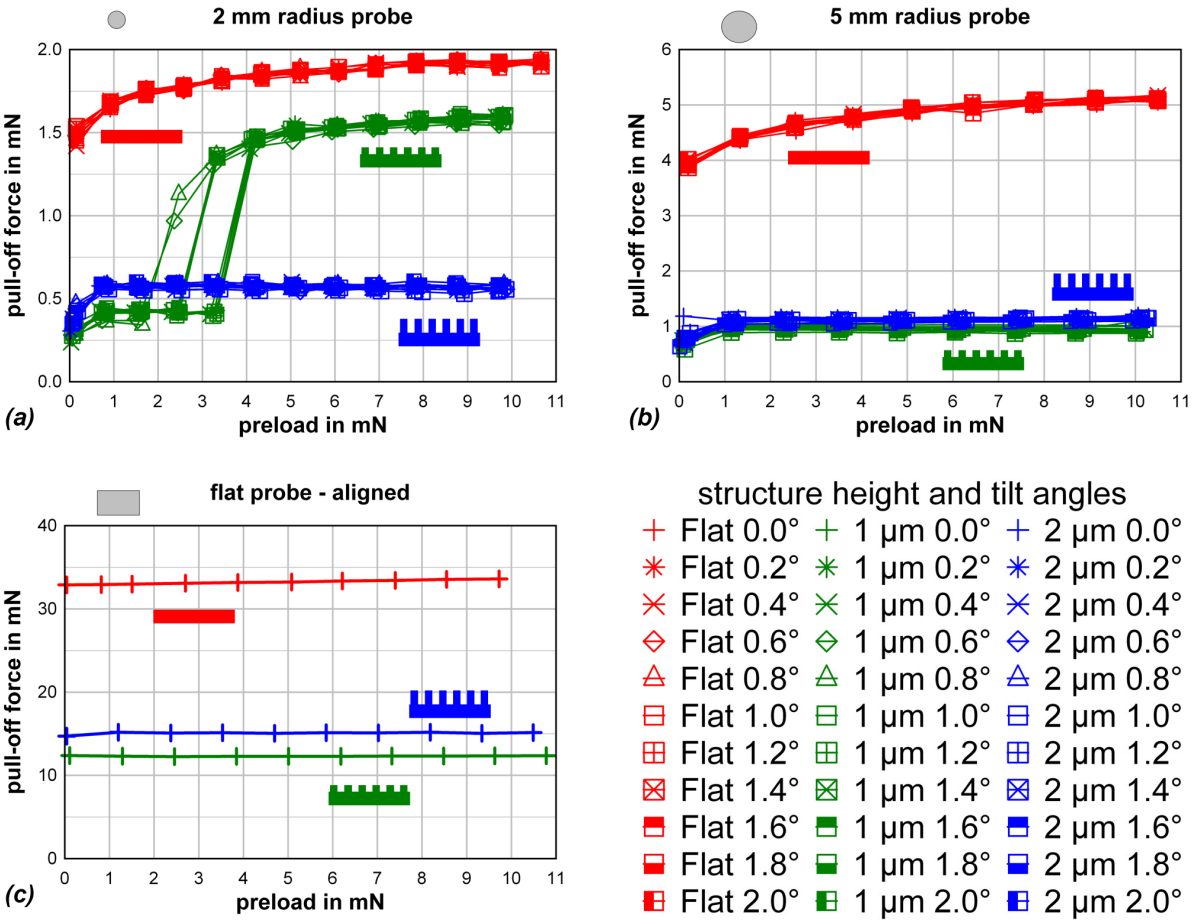

Figure 6.4: Adhesion measurements on flat and patterned samples performed with spherical probes of (a) 2 mm, (b) 5 mm radius, and (c) with a flat-ended cylindrical probe of 1 mm diameter in the aligned state.

Figures 6.5a-c show representative pull-off strength data obtained from Figures 6.4a-c by normalizing the force values with the apparent contact area. For spherical probes, the contact area was calculated from the indentation depth (Figure 6.5d), as was previously done in [2,12,18-19]. The indentation depth itself was calculated from the difference between sample displacement and cantilever deflection. This resulted in graphs, where pull-off strength is plotted against preload pressure. In Figure 6.5b and 6.5d the same jump in adhesive interaction between probe and AR0.2 sample as in Figure 6.4a can be found. While pull-off strength for spherical probes decreased with increasing preload pressure, constant pull-off strength values were found for flat probe measurements.

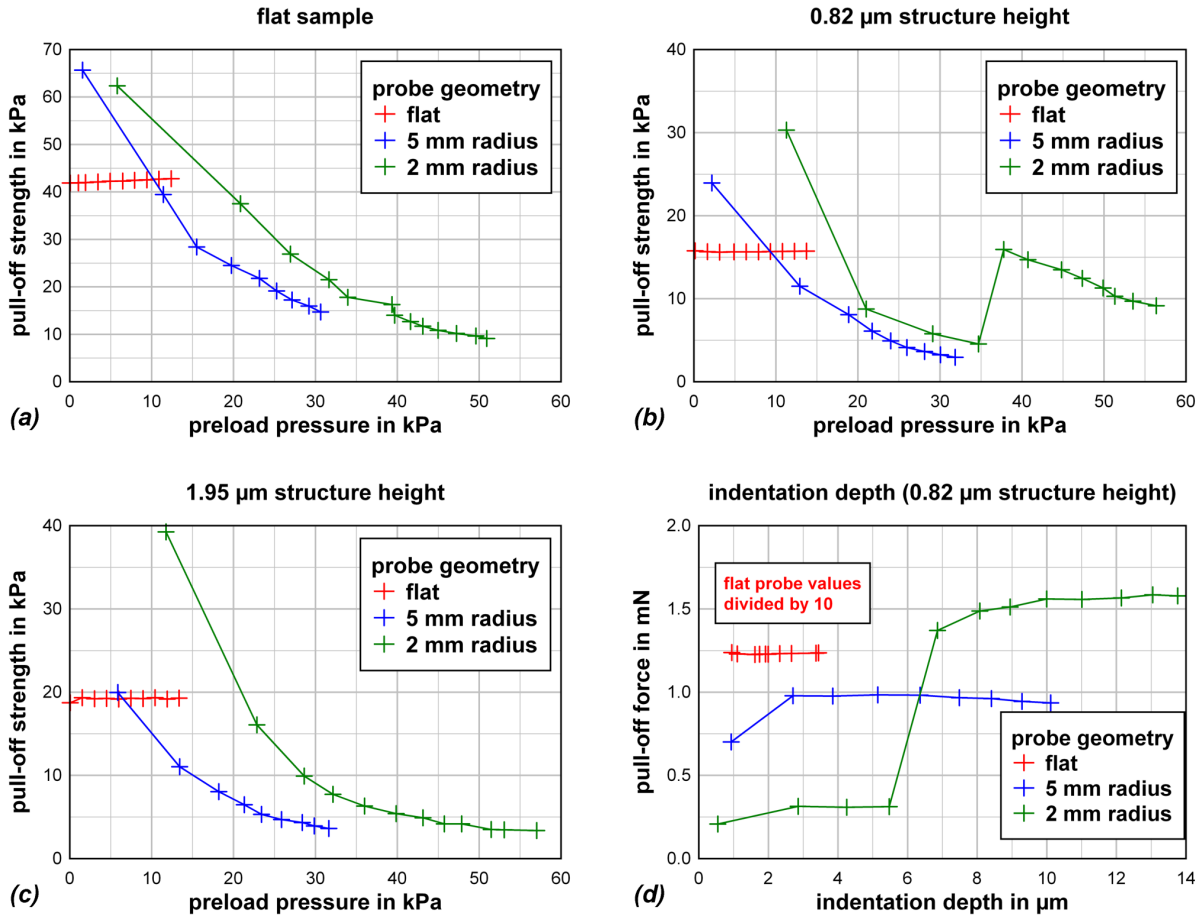

Figure 6.5: Representative adhesion strength curves, where the pull-off force from Figure 6.4 has been normalized by the projected contact area, calculated from the indentation depth and the probe geometry. Preload pressure and pull-off strength is shown for (a) the flat control sample and for (b) the samples with pillar diameters of ~ 4.7 µm and heights of ~ 0.82 µm and (c) heights of ~ 1.95 µm. (d) shows the indentation depth for the AR0.2 sample.

6.4 Discussion

6.4.1 Effect of tilt angle on pull-off forces for flat probe measurements

Figure 6.3 shows that the pull-off force is a function of misalignment and preload if adhesion measurements are performed using a flat probe. The highest pull-off force is found for measurements in the aligned state, and the pull-off force shows little or no preload dependence. A slight preload dependence may be caused by a very small misalignment within

the error tolerance, roughness of the sample or dirt particles on the probe and sample. With increasing tilt angle, the pull-off force decreases and becomes more preload dependent. This behavior is to be expected as the probe needs to indent deeper into the sample to form complete contact with increasing tilt angle. The increased preload dependence is also a consequence of indentation depth; for low preloads and higher misalignment the flat probe cannot form complete contact with the sample, thus reducing the contact area. Both effects are expected to be dependent on the dimension of the flat probe. Figure 6.6 schematically shows a contact with perfect alignment (Figure 6.6a) and with a misalignment angle θ (Figure 6.6b).

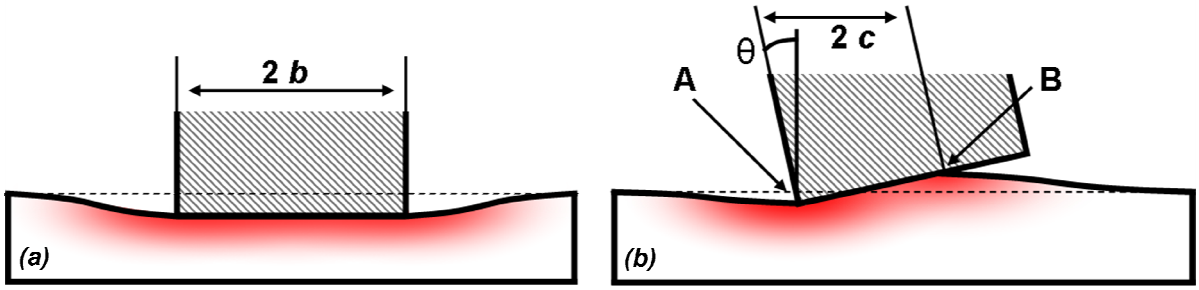

Figure 6.6: Schematic of indentation into a compliant half-space with a hard rigid flat probe in (a) the aligned and (b) the misaligned case. (a) Complete contact between probe and sample is formed at low preloads and with small deformation of the sample, resulting in high adhesion and low preload dependence of the pull-off force. (b) Substantial deformation is required to form complete contact, resulting in a preload dependent and reduced pull-off force. The dashed lines represent the half space before deformation.

Interestingly, the drop in adhesion for increasing misalignment is more pronounced for patterned samples than for flat ones. In particular the AR0.2 pillars seem to be more sensitive to misalignment than AR0.4 pillars as shown in Figure 6.3b and 6.3c. The effect increases with decreasing pillar height. Note that the angle sensitivity of the pull-off forces may depend on the pillar tip geometry as well and will be investigated in further studies, see also Chapter 7.

6.4.2 Effect of probe geometry

The adhesion measurements with spherical probes proved that the pull-off force is independent of the alignment, as expected. For AR0.2 pillars, an abrupt increase in pull-off force was found at a preload of ~ 2.5 mN (see Figure 6.4a). This increase in pull-off force may be caused by contact of the probe with the backing layer, which was visualized in earlier studies for AR0.2 pillars [1]. If a spherical probe is pressed into a patterned sample, it will form contact with the backing layer at a certain preload. This results in a larger area of contact, increasing the released adhesion energy. However, this event is not linked to the indentation depth of the probe. Figure 6.5d shows that the same indentation depth is reached with the 5 mm radius probe, but no increase in pull-off force occurs. If the pull-off strength is plotted vs. preload pressure, however, the jump in pull-off strength occurs at preload pressures which have not been investigated for the 5 mm radius probe in this study.

Figure 6.7 shows the pull-off forces for patterned samples normalized by the values from flat control samples, which allows closer investigation of probe geometry effects. While flat probe measurements result in normalized pull-off force values of ~ 38% for AR0.2 pillars and ~ 43% for AR0.4 pillars (Figure 6.7a), measurements with spherical probes lead to lower relative pull-off forces. Relative pull-off force values of ~ 22% (disregarding the values for preloads larger than 1.5 mN) and ~ 34% were found for AR0.2 and AR0.4 samples using the 2 mm radius probe (Figure 6.7b). Measurements with the 5 mm radius probe resulted in values of ~ 20% and ~ 24% (Figure 6.7c).

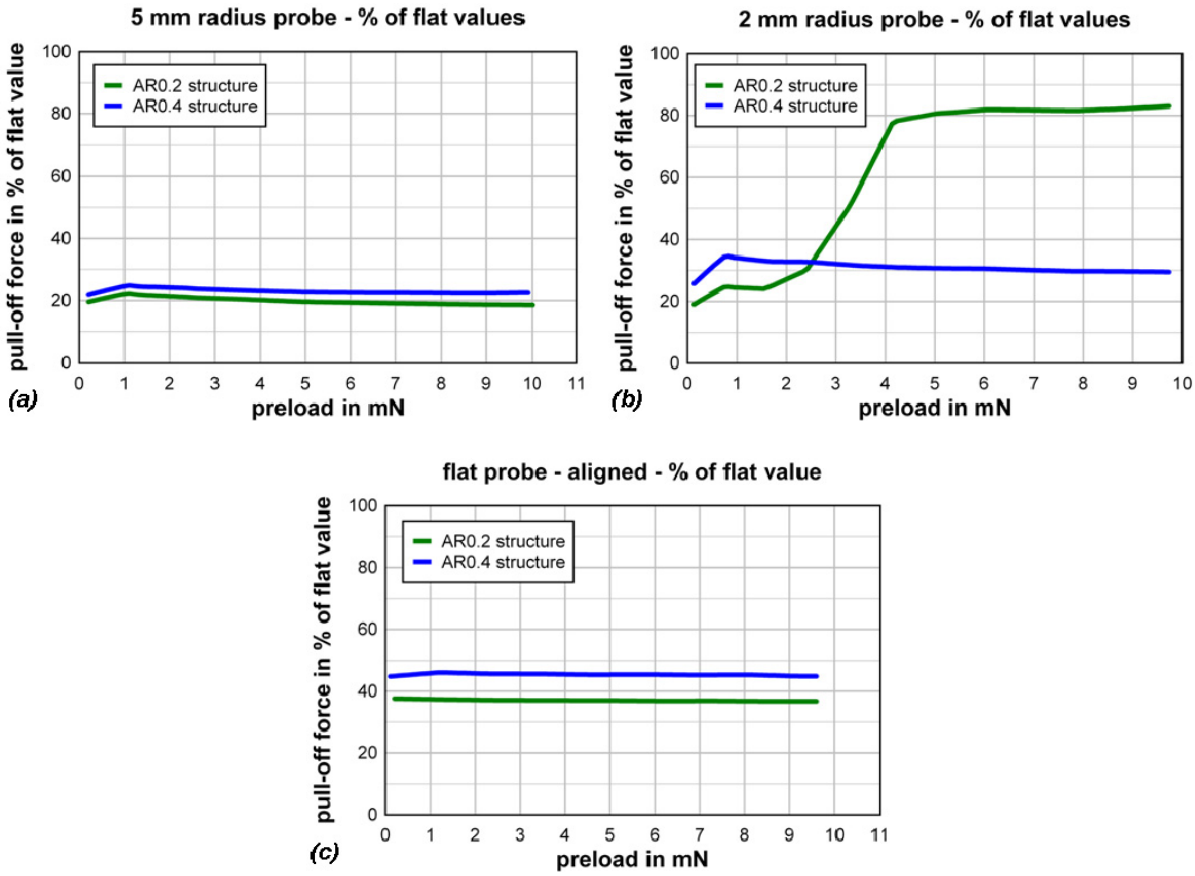

Figure 6.7: Pull-off forces measured on samples with ~ 0.82 µm (AR0.2) and ~ 1.95 µm pillar height (AR0.4). The pull-off forces were divided by pull-off force values obtained for flat PDMS. The graphs show results from measurements with (a) flat probes, (b) spherical probes of 2 mm radius, and (c) 5 mm radius.

The sensitivity of patterned surfaces to misalignment as mentioned in the previous section would explain the discrepancy in pull-off force ratios measured for different probe geometries. Due to the curvature of the spherical probe, pillars directly under the center of the probe are measured in an aligned state, while pillars on the contact periphery will experience a misalignment angle. This misalignment due to probe curvature will result in a lower pull-off force for those pillars. This insight leads to two important points: first, experiments with flat aligned probes show different results than measurements with spherical probes, even if the

probe radius is 3 orders of magnitude larger than the pillar size. And second, the adhesive properties of patterned samples are rather poor when tested with spherical probes.

Another interesting result is the influence of pillar height. Figures 6.3b and 6.3c show that AR0.4 pillars have higher pull-off forces than AR0.2 pillars. We investigated this now well known phenomenon in earlier studies [2]. However, while measurements with flat probes and the 5 mm spherical probe show similar ratios of normalized pull-off force values (~ 1.2 for normalized AR0.4 pillars divided by normalized AR0.2 pillars, see Figures 6.7a and 6.7c), the ratio calculated for measurements with the 2 mm radius probe is higher (~ 1.4 in the preload range from 0 to 1.5 mN). This indicates that pillars with a higher aspect ratio tend to adhere better to spheres with smaller radii. Pillars with higher aspect ratio are easier to bend than those with lower aspect ratio and, therefore, do not store as much elastic energy when adapting to misalignment. These results underline the importance of the pillar aspect ratio for the design of bioinspired adhesive systems.

6.4.3 Model for misalignment effect on pull-off force for a flat probe on a flat sample

To describe the angle dependence of the pull-off force for flat probes on flat samples we propose the following simplified model. We consider a flat, rigid probe with a square contact area of cross-section 2*b* x 2*b*, to be adhered to a compliant, isotropic, linear elastic half-space, and analyze the problem in plane strain. A complete edge, *A*, of the cross section, with length 2*b*, forms perfect contact with the probe as depicted in Figure 6.6, while the tilt angle θ is defined as a rotation around *A*. Let the probe be far away from the sample and then approach it until they touch along *A*. Adhesive interactions will cause the sample to attach to the probe, and an adhered segment will spontaneously generate along the bottom of the probe, extending 2*c* from *A* to *B* (see Figure 6). If the probe is not permitted to move or rotate, the spontaneous

adhesion will cause a tensile load P, and, as in *Kendall*'s problem [39], a square root singularity for stress will appear in the sample at A and B. The stress intensity factors for these singularities at A and B are given by [40]

$$K_I^A = \frac{P}{b\sqrt{\pi c}} - \frac{1}{2}E'\theta\sqrt{\pi c} \quad (1)$$

$$K_I^B = \frac{P}{b\sqrt{\pi c}} + \frac{1}{2}E'\theta\sqrt{\pi c} \quad (2),$$

where $E' = E/(1-\nu^2)$, with E being the Young's modulus of the sample and v its Poisson's ratio. Since θ is positive, $K_I^B > K_I^A$.

For equilibrium, the energy release rate at B, given by $\left(K_I^B\right)^2/2E'$ [41], must equal the adhesive energy, w, from which we find

$$P = b\left(\sqrt{2\pi E' wc} - \frac{\pi}{2}E'\theta c\right) \quad (3).$$

Since the energy release rate $G^A = \frac{K_A^{I\,2}}{2E'}$ at point A is smaller than w, the attachment will attempt to extend around the corner at A and up the side wall of the probe. If the corner is sharp (right angle or very small edge radius) and misalignment is small, the energy release rate will rise very rapidly as the attachment extends due to the severe elastic deformations necessary. As a consequence, the attachment will not extend very far up the side wall of the probe past A. Therefore, we can simply regard the adhesion to terminate at A.

Now consider the misaligned state ($\theta > 0$). If the applied force is zero, the Eq. (3) can be rearranged to predict a value for the half length of the adhesion, c_o, at zero load, namely

$$c_0 = \frac{8w}{\pi E' \theta^2} \quad (4).$$

If $c_o > b$, the entire bottom surface of the probe will attach. It follows that this will occur when $\theta \le \sqrt{8w/\pi E' b}$, and so very small misalignment, or its absence, will lead to full attachment of the probe at zero load.

Now let the probe attach partially at zero load, so that Eq. (4) is valid for the half length of the attachment. To create an attachment for which the half length is larger than c_o, Eq. (3) indicates that a compressive force is required. Conversely, an attachment having a half length shorter than c_o requires a tensile load to be applied. The form of Eq. (3) makes it obvious that $P = 0$ occurs when $c = 0$. It follows that there is a maximum tensile load for a value of c lying between 0 and c_o; this will be the pull-off load, P_c, found to be

$$P_c = \frac{wb}{\theta} \quad (5).$$

When $2w/\pi E' \theta^2 < b \le 8w/\pi E' \theta^2$, the probe will be fully adhered at zero load, but the attached length of the adhesion will reduce stably when a small tensile load is applied. This stable process will continue as larger loads are applied, causing the attached length to reduce, until the applied load equals P_c and the probe detaches. It follows that P_c from Eq. (5) is the pull-off load for all cases, where $\theta > \sqrt{2w/\pi E' b}$.

Now consider cases, where $\theta \le \sqrt{2w/\pi E' b}$. The probe will be fully attached at zero load, but with shrinking attachment length the applied load will diminish. It follows that as soon as a sufficiently high load is applied to cause the attached length to shrink, the probe will detach

unstably. The detachment process will commence when the energy release rate at point *B* equals the adhesion energy. It follows that in this situation the pull-off load will be given by Eq. (3) with *c* replaced by *b*. The complete picture is given by

$$\begin{aligned} P_c &= b\left(\sqrt{2\pi E' wb} - \frac{\pi}{2} E'\theta b\right) && \theta \le \sqrt{\frac{2w}{\pi E' b}} \\ P_c &= \frac{bw}{\theta} && \theta > \sqrt{\frac{2w}{\pi E' b}} \end{aligned} \qquad (6).$$

6.4.4 Comparison with data in Figure 6.3a

If we take the second of the predictions in Eq. (6), valid for larger misalignment, we deduce that the experimental results for the asymptotic behavior for large preload should be inversely proportional to the misalignment angle. In Figure 6.8 the pull-off force at maximum applied preload (~ 10 mN) is plotted versus the inverse tilt angle. As predicted, the pull-off force is proportional to $1/\theta$, restricted to tilt angles larger than 0.4°. According to Eq. (5) the slope of the fit is proportional to the adhesion energy, computed to be 0.46 J/m^2, where we have used the probe radius of 0.5 mm as the value for *b*. According to the model, the y-axis intercept of the linear fit should be zero. The offset apparent in Figure 6.8 may arise for several reasons, ranging from experimental errors due to the small preloads applied, to friction effects that cannot be controlled. In addition, the model presented is based on plane strain calculations, while the results shown in Figure 6.3a are for a three dimensional configuration, introducing further imprecision in the comparison of the model with the experimental results.

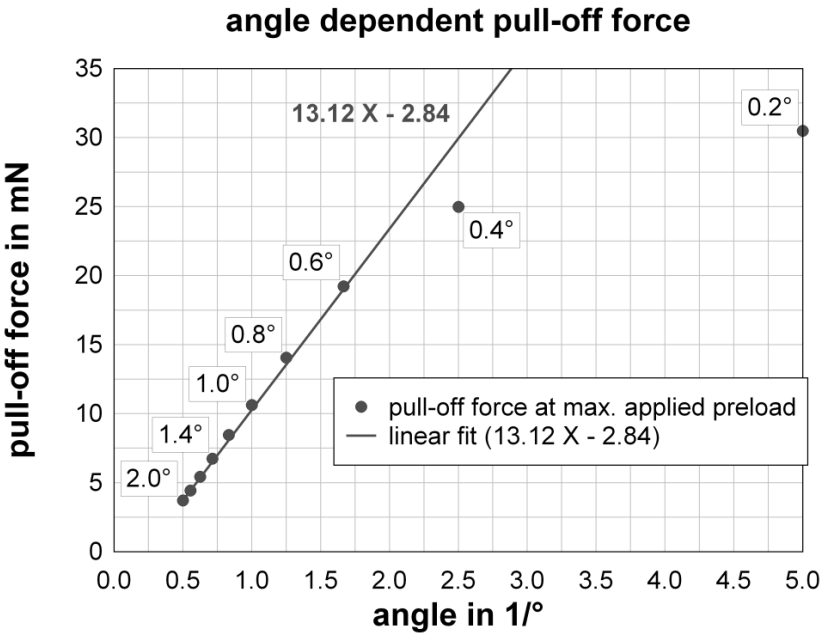

Figure 6.8: Pull-off force at maximum preload versus the inverse tilt angle. A linear fit is drawn for tilt angles larger than 0.4° with a slope of 13.12 mN° and a y-axis intercept of -2.84 mN.

6.5 Conclusion

In this study we compared adhesion measurements on flat and patterned samples using different probe geometries, namely flat probes and spherical probes with 2 and 5 mm radii. The following conclusions can be drawn:

- Adhesion measurements with flat probes strongly depend on the misalignment angle. For measurements in an aligned configuration there is little or no preload dependence of the pull-off forces. Increasing misalignment causes a significant drop in pull-off force and increases its preload dependence.
- Patterned samples with cylindrical pillars are more sensitive to misalignment than flat control samples, if tested with a flat probe. This behavior may differ with varying tip geometry and aspect ratio of the pillars.

- Adhesion measurements with spherical probes are independent of alignment. Tilting the probe +/- 2° does not influence the pull-off force.
- The ratio of pull-off force measured for patterned samples to that for flat samples depends on the probe geometry. Measurements with spherical probes lead to lower values of pull-off forces for patterned samples due to their curvature dependent misalignment.
- Experiments with flat aligned probes show a different adhesion behavior than those obtained with a spherical probe, even if the radius of the spherical probe is 3 orders of magnitude larger than the pillar features.
- For the spherical probe with 2 mm radius, a jump in pull-off force was observed, which may be caused by probe contact with the backing layer. This effect is not linked to indentation depth by the probe but may be a function of preload pressure, pillar aspect ratio and pillar spacing.
- Aligned flat probes do not experience a variation in their contact area, thus resulting in preload independent pull-off strength values, allowing a straight-forward evaluation of adhesion performance.
- We have proposed a simple model describing the effect of probe tilting on the pull-off forces at high preloads.

Spherical probes involve a simple experimental setup. However, aligned flat probes lead to direct acquisition of the pull-off strength, which is of significance in the evaluation of adhesive properties in an engineering context. Furthermore, effects such as the tilt angle dependence of adhesion for patterned samples can be quantified, or – in the case of measurements in the aligned configuration – avoided.

6.6 References

[1] Crosby, A. J.; Hageman, M.; Duncan, A. *Langmuir* **2005**, *21*, 11738-11743.

[2] Greiner, C.; del Campo, A.; Arzt, E. *Langmuir* **2007**, *23*, 3495-3502.

[3] Majidi, C.; Groff, R. E.; Maeno, Y.; Schubert, B.; Baek, S.; Bush, B.; Maboudian, R.; Gravish, N.; Wilkinson, M.; Autumn, K.; Fearing, R. S. *Phys. Rev. Lett.* **2006**, *97*, 076103.

[4] Peressadko, A.; Gorb, S. *J. Adhes.* **2004**, *80*, 1–15.

[5] Varenberg, M.; Peressadko, A.; Gorb, S.; Arzt, E. *Appl. Phys. Lett.* **2006**, *89*, 121905.

[6] Glassmaker, N. J.; Jagota, A.; Hui, C.-Y.; Noderer, W. L.; Chaudhury, M. K. *Proc. Natl. Acad. Sci. U. S. A.* **2007**, *104*, 10786.

[7] Greiner, C.; Arzt, E.; del Campo, A. *Adv. Mater.* **2009**, *21*, 479–482.

[8] Jeong, H. E.; Lee, J.-K.; Kim, H. N.; Moon, S. H.; Suh, K. Y. *Proc. Nat. Acad. Sci.* **2009**, *106*, 5639-5644.

[9] Lee, J.; Bush, B.; Maboudian, R.; Fearing, R. S. *Langmuir* **2009**, *25*, 12449–12453.

[10] Murphy, M. P.; Kim, S.; Sitti, M. *Appl. Mater. Interface* **2009**, *1*, 489-855.

[11] Vajpayee, S.; Long, R.; Shen, L.; Jagota, A.; Hui, C.-Y. *Langmuir* **2009**, *25*, 2765-2771.

[12] Aksak, B.; Murphy, M. P.; Sitti, M. *Langmuir* **2007**, *23*, 3322-3332.

[13] Murphy, M. P.; Aksak, B.; Sitti, M. J. *Adhes. Sci. Technol.* **2007**, *21*, 1281–1296.

[14] Murphy, M. P.; Aksak, B.; Sitti, M. *small* **2009**, *5*, 170–175.

[15] Davies, J.; Haq, S.; Hawke, T.; Sargent, J. P. *Int. J. Adhes. Adhes.* **2009**, *29*, 380–390.

[16] del Campo, A.; Álvarez, I.; Filipe, S.; Wilhelm M. *Adv. Funct. Mater.* **2007**, *17*, 3590-3597.

[17] del Campo, A.; Greiner, C.; Álvarez, I.; Arzt, E. *Adv. Mater.* **2007**, *19*, 1973–1977.

[18] del Campo, A.; Greiner, C.; Arzt, E. *Langmuir* **2007**, *23*, 10235-10243.

[19] Gorb, S.; Varenberg, M.; Peressadko, A.; Tuma, J. *J. R. Soc. Interface* **2007**, *4*, 271-275.

[20] Kim, S.; Aksak, B.; Sitti, M. *Appl. Phys. Lett.* **2007**, *91*, 221913.

[21] Kim, S.; Sitti, M. *Appl. Phys. Lett.* **2006**, *89*, 261911.

[22] Santos, D.; Spenko, M.; Parness, A.; Kim, S.; Cutkosky, M. J. *Adhes. Sci. Technol.* **2007**, *21*, 1317-1341.

[23] Kim, T.; Jeong, H. E.; Suh, K. Y.; Lee, H. H. *Adv. Mater*. **2009**, *21*, 2276–2281.

[24] Kim, S.; Sitti, M.; Xie, T.; Xiao, X. *Soft Matter* **2009**, *5*, 3689–3693.

[25] Reddy, S.; Arzt, E.; del Campo, A. *Adv. Mater.* **2007**, *19*, 3833–3837.

[26] Johnson, K. L.; Kendall, K.; Roberts, A. D. *Proc. R. Soc. Lond. Ser. A.* **1971**, *324*, 301-313.

[27] Kendall, K. *Ph. D. dissertation* Cambridge University (UK) **1969**.

[28] Roberts, A. D. *Ph. D. dissertation* Cambridge University (UK) **1968**.

[29] Derjaguin, B. V.; Muller, V. M.; Toporov, Y. P. J. *Colloid Interface Sci.* **1975**, *53*, 314-326.

[30] Greiner, C.; Spolenak, R.; Arzt, E. *Acta Biomater.* **2009**, *5*, 597-606.

[31] Hertz, H. J. *Reine Angew. Math.* **1881**, *92*, 156-171.

[32] Kim, K. S.; McMeeking, R. M.; Johnson, K. L. *J. Mech. Phys. Solids* **1998**, *46*, 243.

[33] Maugis, D. *J. Colloid Interface Sci.* **1992**, *150*, 243.

[34] Schargott, M.; Popov, V. L.; Gorb, S. *J. Theor. Biol.* **2006**, *243*, 48-53.

[35] Spolenak, R.; Gorb, S.; Gao, H. J.; Arzt, E. *Proc. R. Soc. London, Ser. A* **2004**, *461*, 305-318.

[36] Tabor, D. *J. Colloid Interface Sci.* **1977**, *58*, 2-13.

[37] Kroner, E.; Maboudian, R; Arzt, E. *Adv. Eng. Mater.* **2010**, *12*, 398-404.

[38] Kroner, E.; Blau, J.; Arzt, E. *unpublished*

[39] Kendall, K. *J. Adhes.* **1973**, *5*, 77-79.

[40] Tada, H.; Paris, P. C.; Irwin, G. R. The Stress Analysis of Cracks Handbook (Del Research Corporation: Hellertown, PA, USA, **1973**), 3rd Ed.

[41] Johnson, K. L. Contact Mechanics (Cambridge University Press: Cambridge, UK, **1987**), 9th Ed.

6.7 Appendix

The following Figures show all adhesion measurements as a 2.5 dimensional graph. The x-axis shows the misalignment angle, the y-axis the preload and the color code represents the pull-off force. The headline of each graph indicates the measurement system (probe geometry on sample pattern). AR0.2 indicates pillars with a height of 0.82 ± 0.02 µm and AR0.4 pillars with a height of 1.95 ± 0.02 µm. All pillar diameters were approx. 4.7 µm, hexagonally packed and had a center-to-center spacing of approx. 10 µm.

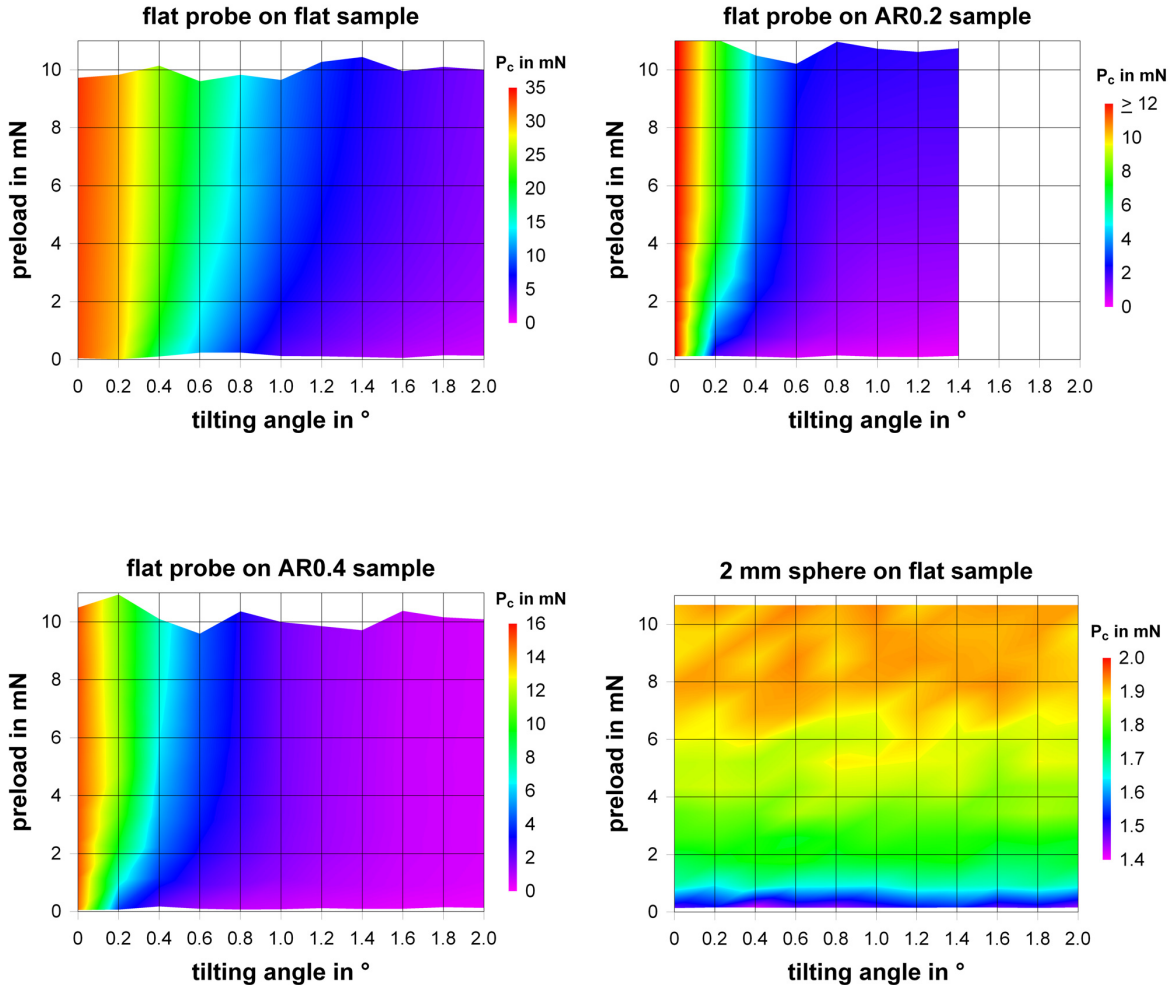

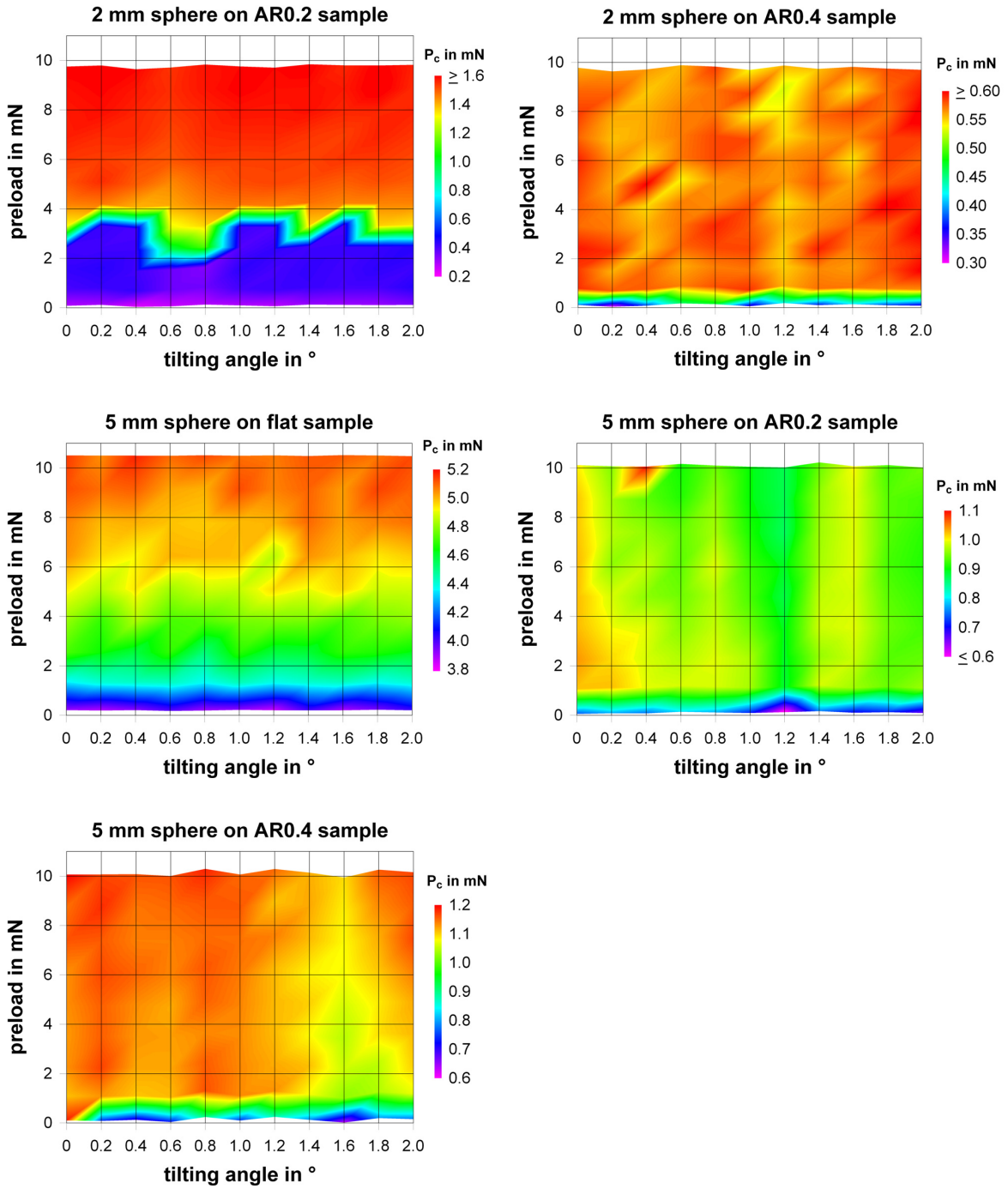

Figure 6.7 Appendix 1: Angle dependent adhesion measurements with flat and spherical probes of 2 mm and 5 mm radius, respectively, on flat PDMS and patterned PDMS with pillars of AR0.2 and AR0.4.

7. Adhesion Measurements on Macroscopic Single Pillars

Abstract – The studies in Chapter 6 indicate that patterned surfaces show a stronger tilt angle dependency of the pull-off force than flat control samples, if measured with a flat probe. However, it was not possible to distinguish between effects related to the pillar geometry and the influence of backing layer deformation. For this reason, adhesion tests were performed on single macroscopic pillars to study the influence of pillar tip shape on angle dependent adhesion and the influence of pillar geometry on the compressive behavior of the sample. Polydimethylsiloxane macropillars with 400 µm diameter and aspect ratios ranging from 1 to 5 were fabricated. The tip geometries were modified to achieve spherical, flat and mushroom shaped tips. While pillars with spherical tips showed no angle dependent pull-off force, flat tip pillars exhibited a strong angle dependence of the pull-off force. For mushroom shaped tips the pull-off force was tilt angle dependent only for low preload, where no complete tip contact was formed. It was possible to identify the contribution of tip geometry, pillar aspect ratio and backing layer deformation to the complete sample compression by analysis of the force displacement curves of the adhesion tests.

7.1 Introduction

The studies presented in Chapter 6 showed that the adhesive properties of patterned surfaces depended on the probe tilt angle when measured with a flat probe. These measurements, however, had several drawbacks; as the pillars were small, the results reflected a combination of angle dependent adhesion of the pillars and of probe indentation into the backing layer. Further, the aspect ratio (AR) of the pillars had to be small to prevent buckling effects, which are known to influence the pull-off force [1]. And finally, the tip geometry of such low AR pillars could not be modified easily. To investigate the influence of tip shape on angle dependent adhesion, it was necessary to design a model system which allows control over tip shape and avoids backing layer indentation of the probe. The goal of this study is to identify the influence of probe tilt of a flat probe on the pull-off force as a function of tip shape by adhesion measurements on macroscopic pillars. Further, the deformation behavior of the pillars will be investigated by adhesion measurements on single macroscopic pillars with different tip shape and AR.

7.2 Experimental

7.2.1 Sample fabrication

To prepare polydimethylsiloxane (PDMS) samples (Sylgard 184, Dow Corning) with single macroscopic pillars, templates were fabricated at the workshop of the INM – Leibniz Institute for New Materials. A cavity of approximately 3 mm depth was milled into an aluminum block. Inside this cavity, a hole was milled as shown in Figure 7.1. Five different templates were fabricated with 400 µm diameter holes and depths of 400 µm, 800 µm, 1200 µm, 1600 µm and 2000 µm, respectively (AR 1 to 5). These templates were then cleaned with ethanol in an ultrasonic bath. To remove aluminum splinters due to the milling process from the holes, uncured PDMS was poured into the cavities. After degassing the PDMS in a desiccator the

polymer was cured at 100°C for two hours. The metal splinters were imbedded into the PDMS and could be removed by carefully demolding the PDMS from the templates. This process was repeated until no further metal splinters were visible by light microscopy in the PDMS samples after demolding.

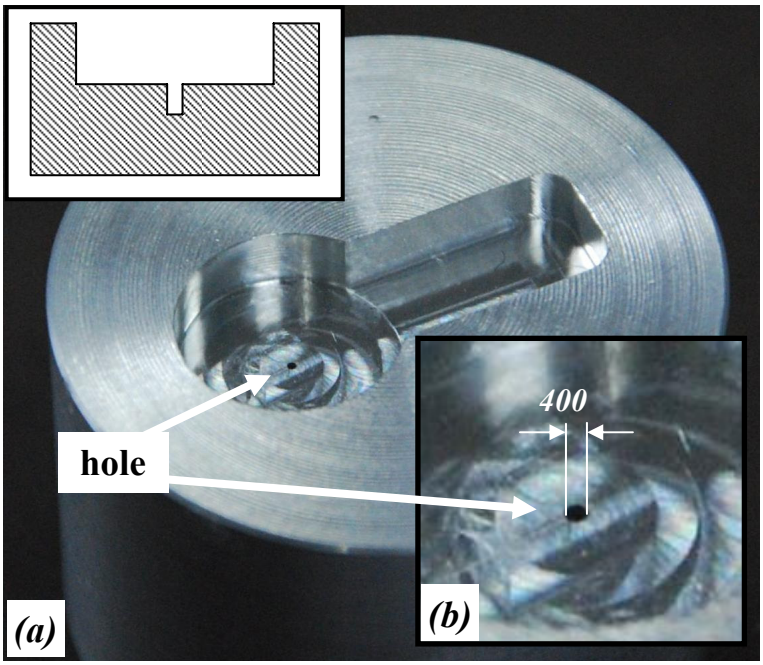

Figure 7.1: Aluminum template for fabrication of single pillar samples. (a) A cavity is milled into the aluminum block with a hole in the middle. (b) Close-up of the milled hole. The inlay in the upper left corner shows a schematic cross section of the mold.

Samples were prepared by filling uncured PDMS into the cavity, degassing in a desiccator until no bubbles formed above the template holes, and curing at 75°C in air for 2 hours. The pillar tips were modified as follows: to achieve spherical tips, a small droplet of uncured PDMS was placed on top of the pillar with a needle. The pillar top was wetted by the droplet, forming a spherical geometry. Mushroom shaped tips were fabricated by placing a droplet onto the pillar top and putting a thin glass piece onto the pillar. The glass piece pressed the liquid PDMS into a mushroom shape. To ensure an identical fabrication process for the flat

tip pillars, e.g. adding additional PDMS on top of the pillar, a droplet of liquid PDMS was placed on the tip and almost completely removed again to obtain flat tips and to flatten out roughness. The samples with modified tips were then cured for 16 hours at 75° in air. After curing, the glass pieces were carefully removed from the mushroom shaped pillars. All samples were then left for relaxation at room temperature for more than 3 days prior to adhesion testing.

7.2.2 Adhesion measurements

Angle dependent adhesion measurements were performed on the adhesion tester MAD (Version 2 with *in situ* visualization), which is described in Chapter 4. A double-clamped cantilever was used for force sensing (see Chapter 4). It had a spring constant of 434 ± 2 N/m. A square piece of silicon wafer with 3 x 3 mm size was glued to the bottom of the cantilever and used as a probe. Prior to measurements the silicon probe was cleaned with ethanol. Thereafter, it was brought into contact for 1000 times with a piece of PDMS to obtain an equilibrium surface state, see Chapter 5.

The aligned state for the experiments was determined by measuring the pull-off force for constant preload as a function of tilt angle. First, an angle scan was performed by tilting the sample around one axis. Then, after identifying the center of the pull-off force symmetry, a second angle scan was carried out by tilting around the other axis. This procedure was repeated until the alignment angle was determined with ± 0.05° accuracy. The pull-off force was measured for different preloads on all samples in the aligned state. The tilt angle was then varied in angle steps of 0.2°, repeating the preload dependent pull-off force measurements. The testing velocity for all experiments was 10 µm/s. Temperature and humidity were acquired before each experiment and were 27.5 ± 0.5°C and ~ 40 ± 5%, respectively.

7.3 Results

7.3.1 Sample geometry

Figure 7.2 shows exemplary scanning electron microscopy (SEM) images for pillars with AR 2 and spherical (a, d), flat (b, e) and mushroom shaped tips (c, f). The pictures were taken in plan view (a)-(c) and with a tilt angle of 30° (d)-(f). Pillars with spherical tips showed a very smooth and homogeneously curved tip. The flat tip pillars exhibited a slight waviness of the tip. Mushroom shaped tips had a flat surface and some small defects on the rim of the tip.

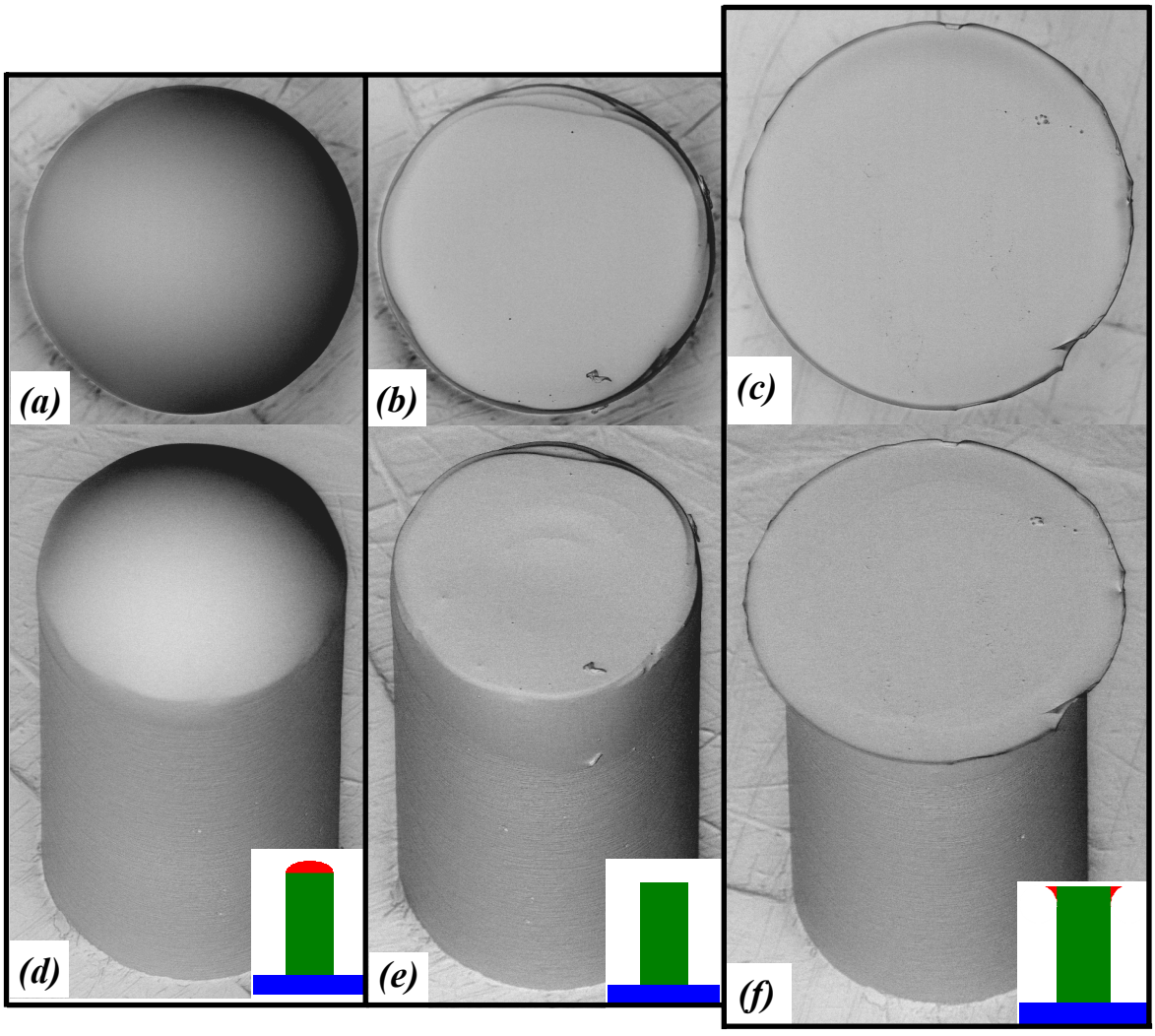

Figure 7.2: SEM images of samples with spherical (a,d), flat (b,e) and mushroom shaped tips (c,f). The scale bar corresponds to 100 µm. (a-c) are plan views of the pillars, (d-f) are tilted by 30°. Pictures were taken by D. Paretkar. The image contrasts were inverted.

The pillar geometry was defined by the pillar height and the tip height (spherical tips) or tip width (mushroom shaped tips). Figure 7.3 shows a schematic of the different geometrical parameters.

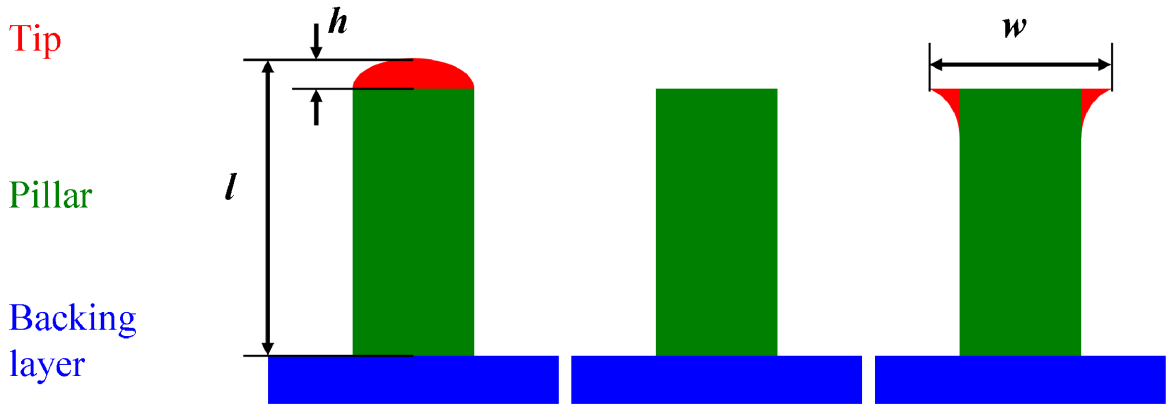

Figure 7.3: Schematic of the geometrical parameters with a spherical, a flat and a mushroom shaped tip. The pillars were characterized by their pillar length l *and their tip height* h *and tip width* w.

The height and diameters of the molded PDMS pillars as well as the tip width of the mushroom shaped pillars were measured using white light interferometry. The pillar diameter for the mushroom tip pillars was determined by measuring the width of the holes in the templates. All diameters were determined to be 402 ± 10 µm. In case of the spherical tip pillars, the tip height was calculated by subtracting the height of flat tip pillars from the height of the spherical tip pillars (see also Figure 7.3). The results are summarized in Table 7.1.

The measured heights were close to the expected heights for AR 1 to 5, namely 400 µm, 800 µm, 1200 µm, 1600 µm and 2000 µm. The height values for the pillars with flat and mushroom shaped tips were identical within the measurement error for the same AR. A significant variability in tip width was found for the mushroom shaped tips, although the same fabrication process was used.

Table 7.1 Pillar height of molded PDMS samples

tip geometry	AR	Pillar length *l* in µm	tip width *w* in µm	tip height *h* in µm
spherical tip pillars	1	492		70
	2	873		110
	3	1214		45
	4	1616		59
	5	2062		115
flat tip Pillars	1	422		
	2	762		
	3	1168		
	4	1557		
	5	1947		
mushroom tip pillars	1	421	525	
	2	763	496	
	4	1561	665	

The diameters of all pillars were 402 ± 10 µm.

7.3.2 Adhesion measurements

Angle dependence of adhesion – Pillars with spherical tips did not show a tilt angle dependent pull-off force. For this reason it was not possible to determine the aligned position by measuring the pull-off force using the angle scan technique. Thus, the samples were aligned by using a vertically mounted camera. Although this alignment is not as precise as the angle scan method it still renders reliable results, especially for samples with low or no tilt angle dependent adhesion.

The results for adhesion measurements on pillars with spherical tips are presented in Figure 7.4. A slight increase in pull-off force with increasing preload was found for all tested samples. The pillars with AR 3 and AR 4 showed a higher pull-off force than pillars with the other tested AR.

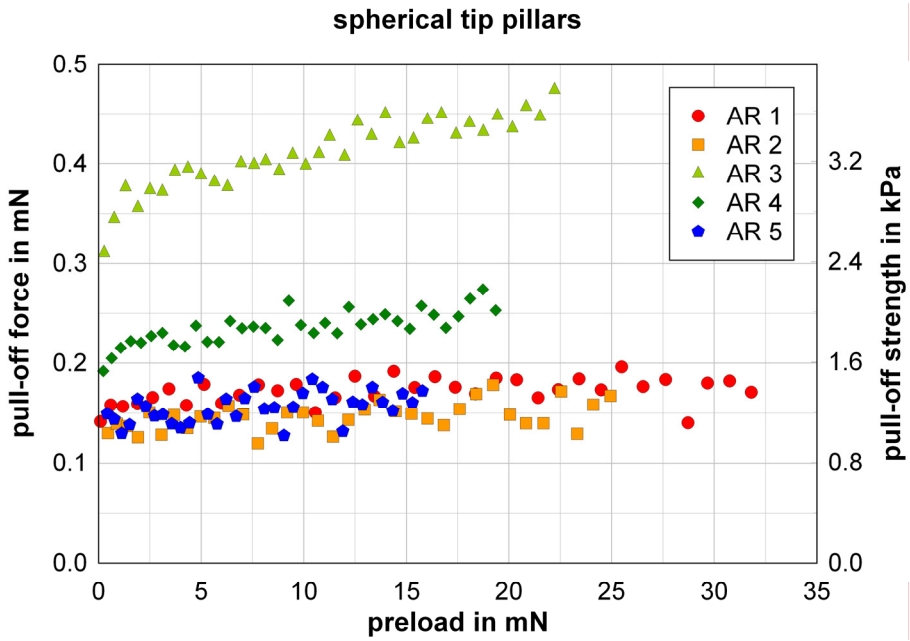

Figure 7.4: Pull-off force for spherical tip pillars with AR 1 to 5. The pull-off strength values were calculated by dividing the pull-off force by the cross-sectional area of the pillar (π (200 μm)²).

In contrast to spherical tip structures a strong angle dependency was found for pillars with flat tips. Figure 7.5 shows the pull-off force as a function of tilt angle at a preload of 15 mN. With increasing tilt angle, the pull-off force decreased for all AR. Samples with AR 2 to 5 showed similar pull-off forces. The flat tip pillar with AR 1 constantly exhibited lower pull-off force values than the pillars with higher AR. The preload dependence of the pull-off force for flat tip pillars in the aligned state is plotted in Figure 7.6. The pull-off strength values were calculated by dividing the pull-off force by contact area.

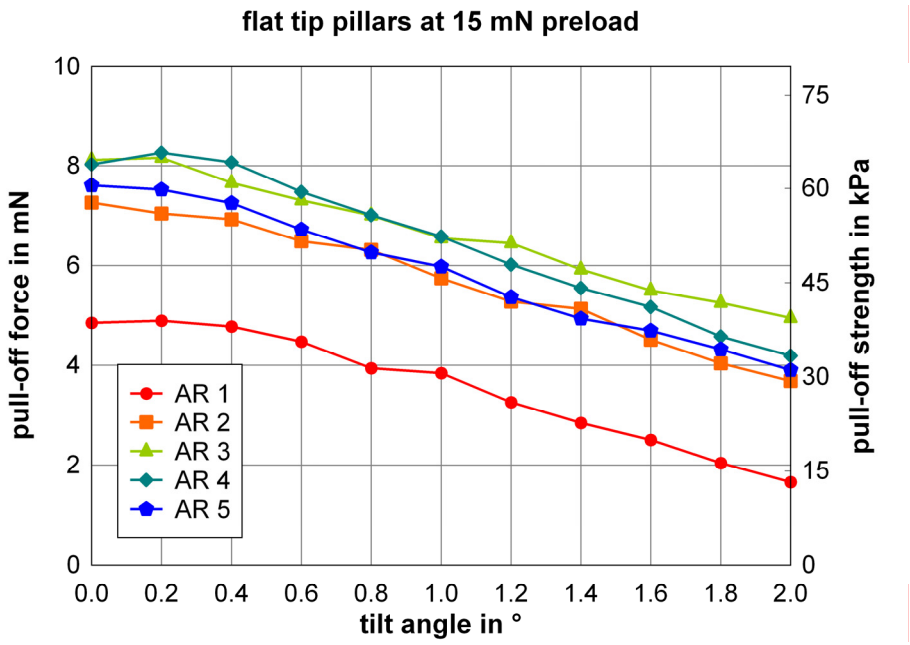

Figure 7.5: Adhesion of pillars with flat tip geometry at 15 mN preload. The data points were interconnected to guide the eye. The pull-off strength values were calculated by dividing the pull-off force by the cross-sectional area of the pillar (π (200 µm)²).

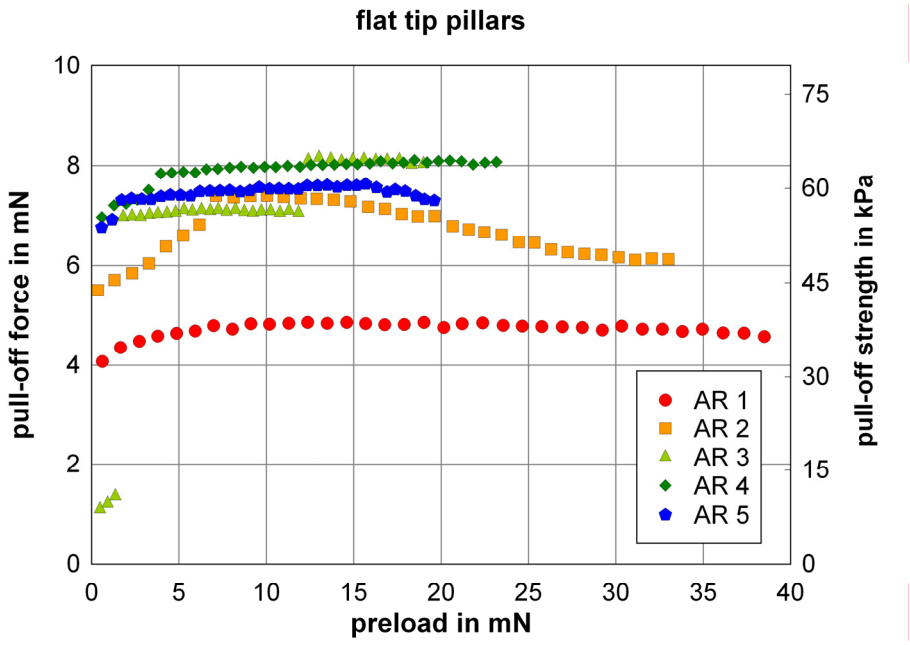

Figure 7.6: Pull-off force measurements for pillars with flat tips and AR 1 to 5 in the aligned state. The pull-off strength values were calculated by dividing the pull-off force by the cross-sectional area of the pillar (π (200 µm)²).

In Figure 7.7 the angle dependent pull-off force (a) and pull-off strength (b) for mushroom tip pillars at 15 mN preload is shown. The pull-off force at this preload was independent of the tilt angle.

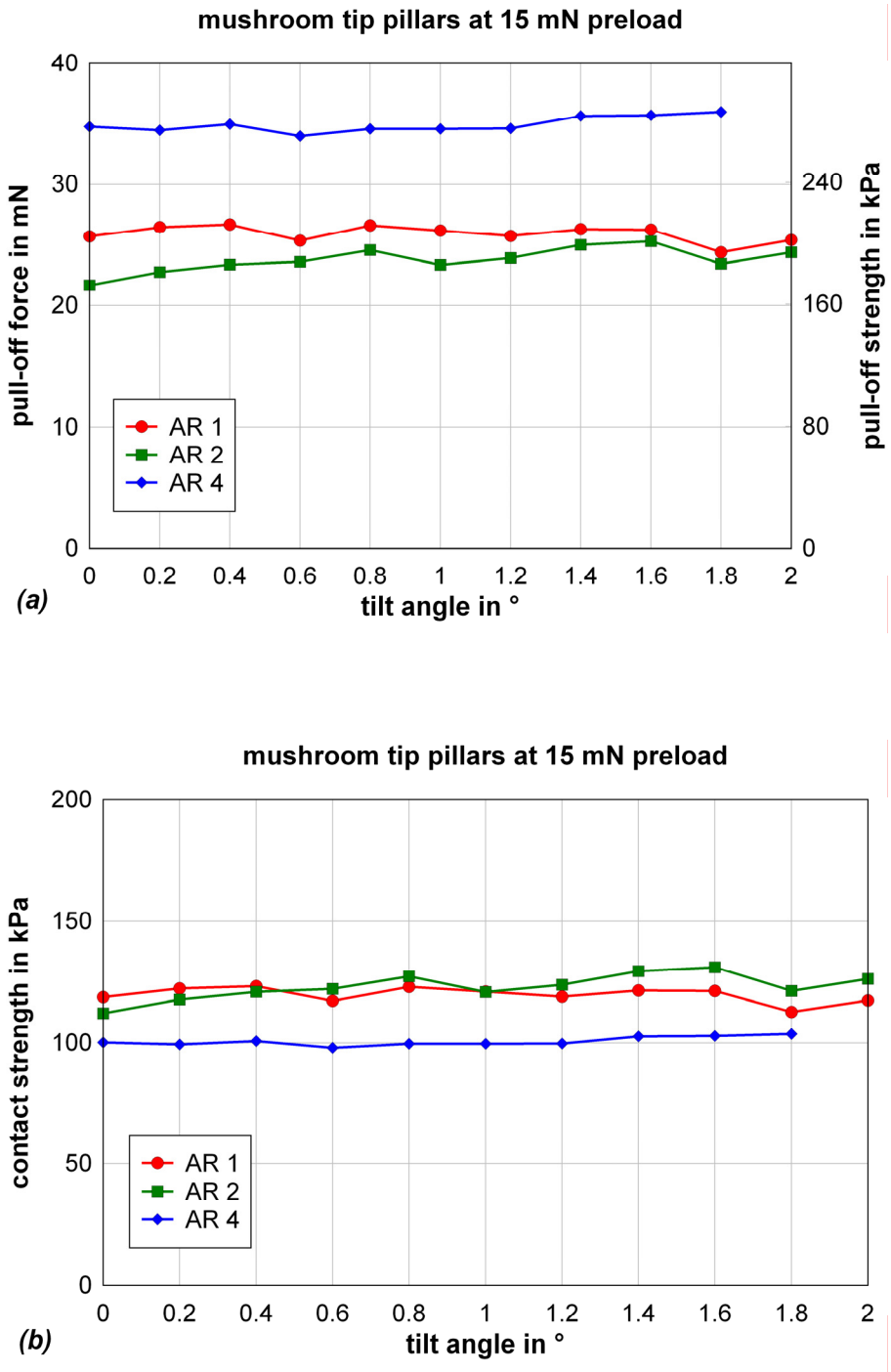

Figure 7.7: Angle dependent adhesion measurements on mushroom tip pillars. In (a), the angle dependent pull-off force is plotted. These values were divided by the tip area A_{Tip} *calculated from width data in Table 7.1 (*$A_{Tip} = w^2\pi/4$*) resulting in the contact strength (b).*

The mushroom tip pillars showed no notable preload dependency of the pull-off force in the aligned configuration, as can be seen in Figure 7.8.

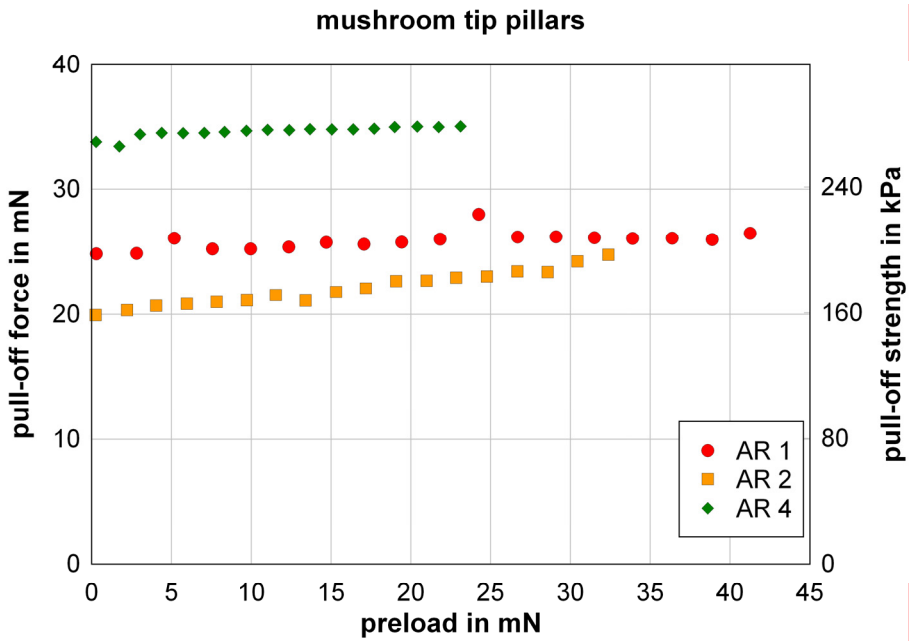

Figure 7.8: Pull-off forces for mushroom tip pillars and with AR 1, 2 and 4. The pull-off strength values were calculated by dividing the pull-off force by the cross-sectional area of the pillar (π (200 µm)²).

However, while the pull-off force for the mushroom tip pillars was constant for almost all tilt angles and preloads, a significantly lower pull-off force was found at very low preload and high tilt angles. Figure 7.9 (next page) shows an exemplary adhesion map for a measurement with a flat probe on a mushroom tip pillar of AR2. The x-axis shows the tilt angle, the y-axis the preload and the pull-off force is color coded. The largest part of the graph is orange and red, showing that a high pull-off force is found for nearly every combination of preload and tilt angle. For low preloads below 5 mN and tilt angles larger than 0.6 the pull-off force values are very low (blue or violet). The transition between the high pull-off force and low pull-off force parameter space is very sharp (see green transition line).

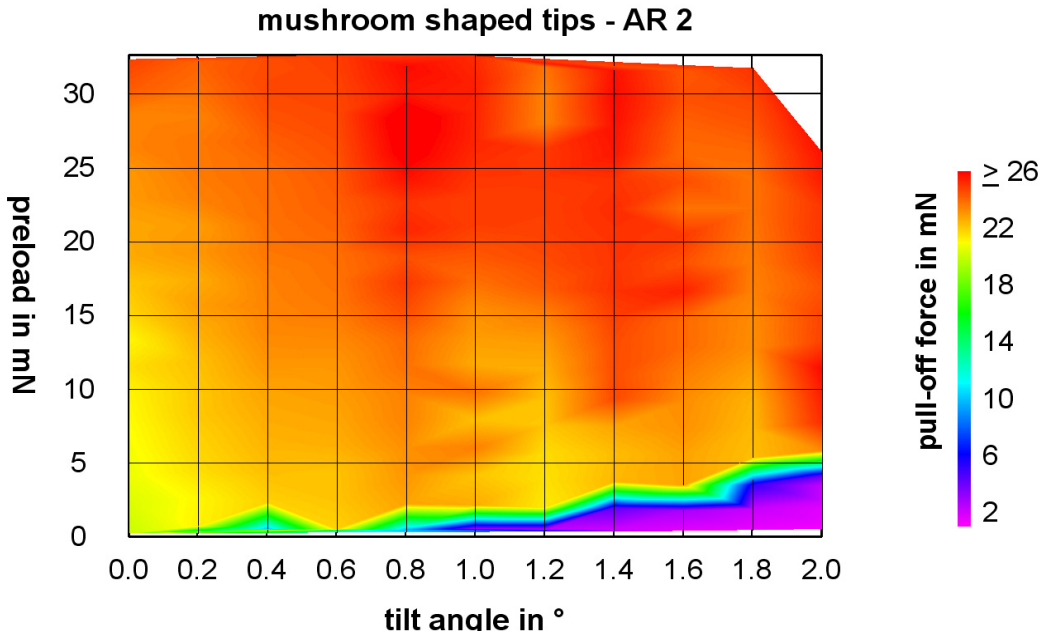

Figure 7.9: Pull-off forces as a function of tilt angle and preload for a mushroom tip pillar with AR 2. For high preload and low tilt angle the pull-off force barely depends on tilt angle and preload. A transition is found for low preload and high tilt angle, where the pull-off force is reduced by approximately one order of magnitude.

Overall, the aligned measurements showed that mushroom tip pillars exhibited the highest adhesion with pull-off forces between 20 and 35 mN, followed by flat tip pillars with pull-off forces between 4 and 8 mN and spherical tip pillars with pull-off forces between 0.1 and 0.5 mN. Figure 7.10 shows the logarithmic plot of the pull-off strength for spherical, flat and mushroom tip pillars as a function of preload. Note that the *pull-off strength* was calculated by dividing the pull-off force by the *cross section* of the pillar and not, like in Figure 7.7b, the *contact strength* (division by the *contact area*). The true contact area for the spherical tip pillars is not available, thus the pull-off strength rather than the contact strength is chosen to be plotted for comparison.

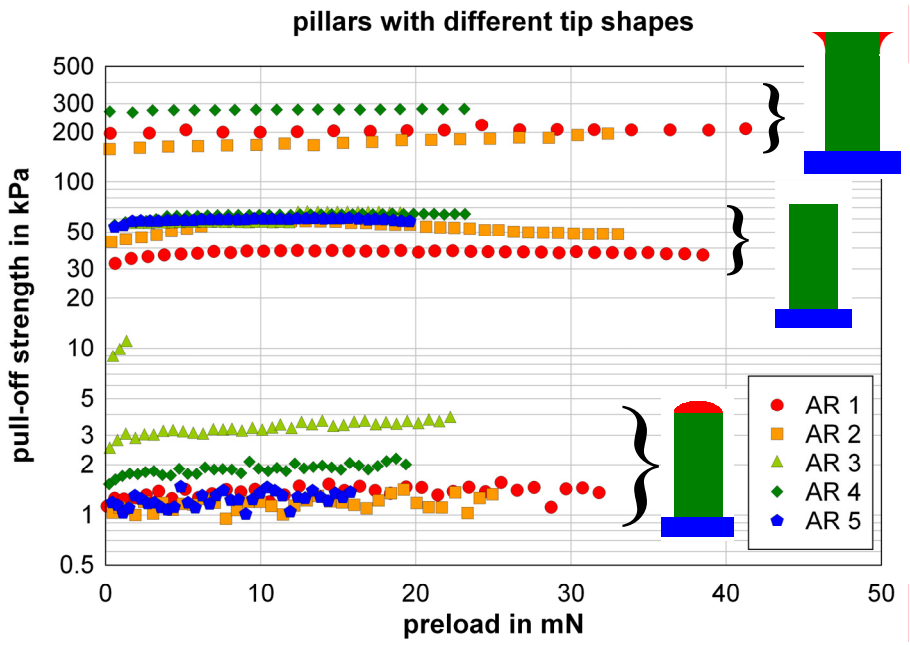

Figure 7.10: Overview of the pull-off strength for mushroom, flat and spherical tip pillars. The mushroom tip pillars adhere best (values between 150 and 300 kPa), followed by the flat tip pillars (values between 30 and 70 kPa) and spherical tip pillars (values between 0.9 and 4 kPa).

Compliance of pillars – In Figure 7.11 the sample compression Δl_{total} is plotted vs. pillar height (including tip height) at 15.5 ± 0.5 mN preload.

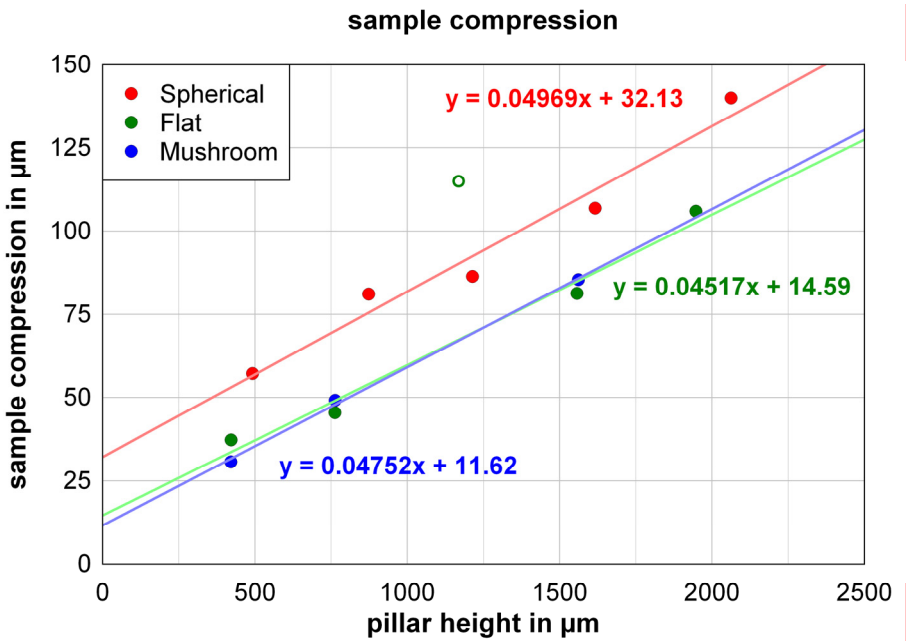

Figure 7.11: Sample compression as a function of pillar height at 15.5 ± 0.5 mN preload. All fits show similar slopes. The y-axis intercept for spherical tip pillars was considerably larger than for flat and mushroom tip pillars.

With increasing pillar height, the sample compression increased linearly. While the slopes of the linear fits were similar for all tip geometries at the same preload, the y-axis intercept for the spherical tip fit was considerably larger than the ones for flat and mushroom shaped tips. The unfilled green data point (Flat AR 3) was not taken into account for the fit as it was most likely a measurement error due to gas bubbles within the pillar.

Figures 7.12a-c show the sample compression as a function of pillar height at different preload for spherical, flat and mushroom shaped tips, respectively. With increasing preload the slope and the y-axis intercept of all linear fits increased.

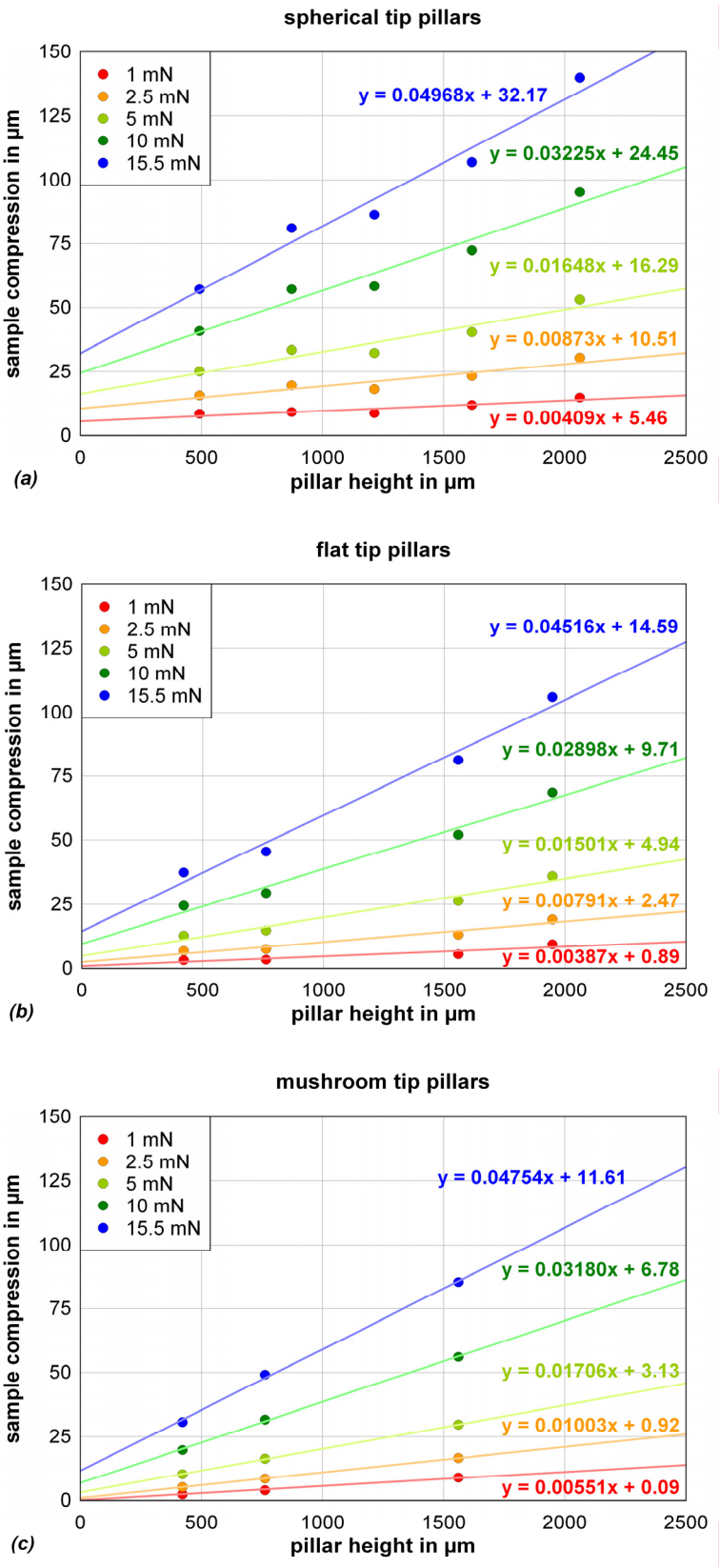

Figure 7.12: Sample compression as a function of pillar height at different preload for spherical (a), flat (b) and mushroom shaped tip pillars (c). With increasing preload the slope and the y-axis intercept of the linear fits increased for all tip geometries.

7.4 Discussion

7.4.1 Tip shape and aspect ratio effect on angle dependent pull-off force

The measurements presented in Figures 7.5 and 7.7 indicate that the angle dependence of the pull-off force is strongly influenced by the tip shape of the tested pillars. As expected, the misalignment has no effect on the pull-off force for pillars with spherical tips. In principle these measurements can be considered as a contact between a soft sphere and a rigid half space, showing the typical preload dependent pull-off force (Figure 7.4). A similar configuration for adhesion measurements is shown in Chapter 6, namely measurements with a rigid spherical probe on a flat PDMS sample (Figure 6.4, Chapter 6.7 Appendix), where no influence of tilt angle on pull-off force was found.

In contrast, the pull-off forces for pillars with flat tips depend on the tilt angle, as can be seen in Figure 7.5. The pull-off force drops with increasing misalignment angle. For tilt angles larger than ~ 0.5°, the pull-off force decreases linearly with increasing tilt angle. This is an interesting result as it differs from the findings in Chapter 6 (see Figure 6.3 and Chapter 6.7 Appendix). There, the pull-off force dropped significantly with increasing tilt angle between 0.5° and 1.0°, while for tilt angles larger than 1.0° the pull-off force values leveled out. This discrepancy can very likely be explained by the probe indentation into the backing layer. For the micropillars tested in Chapter 6 the probe had to indent deeper into the backing layer for larger tilt angles to form complete contact with the sample. Thus, two effects were measured at the same time; the tilt angle dependent pull-off force of the pillars and the angle dependent indentation of the probe into the backing layer. In the measurements presented in this Chapter the probe did not touch the backing layer due to the pillar and probe dimensions. The measured effects therefore can be attributed solely to the pillar geometry. Although the pull-off force is not as strongly angle dependent as shown in Chapter 6, there is still a drop in pull-off force by 40-60% at 2° misalignment for the pillars with a flat tip.

Interestingly, the mushroom shaped pillars reveal tilt angle dependent pull-off forces only for very low preload below 5 mN. For preload larger than 5 mN no tilt angle effect is observed and the transition between low and high pull-off force is very sharp (see Figure 7.9). This can be explained as follows: for low preload (low indentation depth) and high tilt angle, the mushroom tip does not form full contact with the probe. This resembles an opened detachment crack, which will easily propagate and lead to detachment at low tensile forces. If the preload is sufficient for full contact formation between pillar tip and probe, the controlling detachment mechanism changes from crack propagation to crack initiation. Thus, the pull-off force increases significantly.

The influence of AR on the pull-off force for the tested pillars seems to be in contradiction to the results of the up to now most extensive study on aspect ratio effects by *Greiner et al.* [2]. They found that for flat tip pillar arrays the pull-off force and pull-off strength increases with increasing AR. Such a correlation is not found for the data presented in this study. The influence of AR on the pull-off force will now be discussed separately for all tip geometries.

For spherical tip structures, the pull-off force is similar for pillars with AR1, AR2 and AR5, the pull-off force for the AR4 pillar is slightly higher, while the AR3 pillar shows a pull-off force nearly 3 times as high (Figure 7.4). If we consider these circumstances only, the pull-off force would first increase with increasing AR up to a critical value of 3 and then decrease again. However, in the measurements presented above, two parameters were changed at the same time: the AR and the radius of the spherical tip (see Table 7.1). According to the JKR theory the pull-off force depends linearly on the radius of the tip (see Chapter 2, Eq. 2.7). Thus, assuming JKR-type contact for the spherical tip pillars, the effect of tip radius on the pull-off force can be included by dividing the pull-off force by the contact radius. Figure 7.13

shows the normalized pull-off force as a function of preload for the tested spherical tip pillars. The tip radius r was calculated from the tip height h (Table 7.1) and the pillar radius a (200 µm) using $r = \frac{a^2 + h^2}{2h}$.

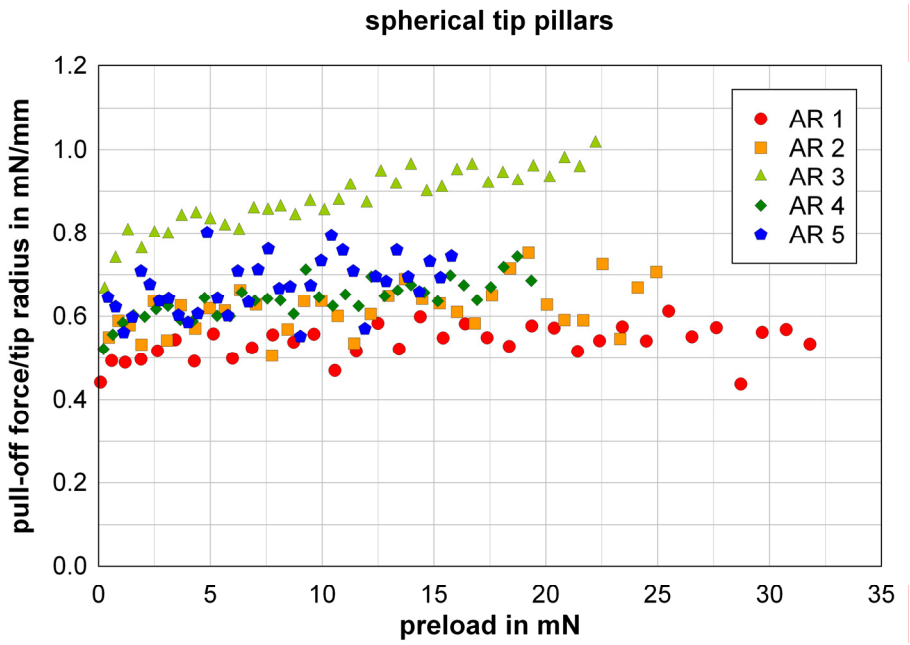

Figure 7.13: Pull-off force normalized by the tip radius as a function of preload for spherical tip pillars of different AR.

This plot shows a significantly decreased difference between the normalized pull-off forces for different AR. The residual difference for the various AR may be explained by small defects on the spherical tips, measurement errors due to the height measurement of the spherical tip and a larger data scattering because of the low pull-off forces. In the light of these considerations it can be concluded that the AR has no measureable influence on the pull-off force for large spherical tip structures. A possible AR dependency of the pull-off force may occur for smaller pillars with higher pull-off stresses, arrays of pillars which interact with each other through the backing layer or for measurements on arrays of pillars

using spherical probes. An additional graph showing the pull-off force as a function of tip radius is shown in 7.7 Appendix.

The results of the flat tip pillars may be directly compared to those from the studies of *Greiner et al.* [2], as the tip geometry is similar. According to *Greiner et al.*, the pull-off force should increase with increasing AR, which cannot be confirmed by the results in this study. While the AR1 sample shows a low pull-off force of approximately 5 mN, the pillars with the higher AR showed similar pull-off forces around 7.5 mN. The low pull-off force for the AR1 sample may again be explained by some defects on the pillar tip. The SEM graphs in Figures 7.2b and 7.2e show a defect along the tip which might initiate a detachment and lead to a decreased pull-off force. However, the discrepancy between the findings of *Greiner et al.* and this study may be explained as follows. *Greiner et al.* performed their measurements on flat tip microstructures using a spherical probe. During their adhesion test the pillars below the center of the spherical probe experienced a “flat aligned” probe, while pillars in the boundary region of the contact area made contact with a “flat misaligned” probe due to the curvature of the sphere. According to the results presented in Figure 7.5, the pillars below the center of the spherical probe would contribute more to the pull-off force than pillars in the boundary region of the contact area. If the AR of the pillars for such a testing geometry is increased, the pillars on the boundary of the contact area would store less elastic energy to conform to the misaligned and would have a larger contribution to the pull-off force. This would then lead to an increased overall pull-off force, which would indeed depend on the AR. In this study, such a decreased angle dependent adhesion with increased AR was not found. This may be due to the small deformations applied to the pillars in this study. In the experiments of *Greiner et al.* the probe indentation into the patterned sample was large compared to the pillar size and thus the pillars were compressed much further than it was possible for the macroscopic pillars

tested in this study, where the compression for the flat tip pillars was less than 10% (see Figure 7.12b). It may be possible that the influence of AR on angle dependent adhesion for flat tip pillars is low for small deformation but becomes more significant with increasing pillar compression.

The mushroom tip pillars showed no systematic dependency of the pull-off force on AR as well (Figure 7.7). While the pull-off forces differ significantly, the pull-off strength values are comparable. Thus, the influence of tip diameter on the pull-off force is much larger than the influence of AR. A graph showing pull-off force as a function of tip diameter is shown in 7.7 Appendix.

All these results indicate that the AR has no influence on the pull-off force, if adhesion measurements are performed on single pillars using flat aligned probes. For contact configurations where the pillars do not attach perpendicular to a surface, e.g. spherical probes or rough surfaces, the AR is likely to influence the pull-off force. To strengthen this hypothesis, a detailed study with a wider variation in AR, tip radius for spherical tip pillars and tip diameter for mushroom shaped pillars is necessary, which is beyond the scope of this thesis.

7.4.2 Influence of aspect ratio and tip shape on compliance

The compression of tip, pillar and backing layer (see Figure 7.3, red, green and blue, respectively) can be described by the equation

$$\Delta l_{total} = \Delta l_{tip} + \Delta l_{pillar} + \Delta l_{backing} \qquad \text{(Eq. 7.1)},$$

where Δl_{total}, Δl_{tip}, Δl_{pillar} and $\Delta l_{backing}$ are the measured length change of the sample, the length change due to deformation of the tip, the length change of the pillar and indentation into the backing layer, respectively. Δl_{pillar} is a function of pillar height, while Δl_{tip} and $\Delta l_{backing}$ are independent of pillar height. Thus, the slope in Figure 7.11 represents the pillar strain $\Delta l_{pillar}/l$, while the y-axis intercept is composed of Δl_{tip} and $\Delta l_{backing}$. Note that strictly speaking Δl_{tip} for spherical tip pillars is composed of two parts, a geometry dependent part and a height dependent part. The latter is included in the pillar height in Figure 7.11 for the presented considerations. Thus, the slope represents both pillar compression and the height dependent part of the tip compression. However, the tip height is small compared to the pillar height. Neither the slope nor the y-axis intercept is significantly influenced by replacing the pillar height by the sum of pillar and tip height. Buckling and bending effects can be neglected here, because of the small deformation and the aligned measurement configuration.

PDMS has a Poisson's ratio of 0.5 (no volume change during compression) and viscoelastic effects can be neglected for the slow testing velocity of 10 µm/s. For these boundary conditions and small deformations it can be assumed that the change in pillar length Δl_{pillar} will depend linearly on pillar height and preload for low deformation. It is expected that the backing layer deformation $\Delta l_{backing}$ will be linear as well [3] and independent of AR and tip shape, because the geometrical pillar-backing layer transition is identical for all samples. No additional deformation Δl_{tip} is expected for flat tips. Spherical tips, however, will contribute to the sample deformation in a nonlinear way. Pillars with mushroom tip shape may show a behavior similar to flat tip pillars. Accordingly, the slope reflects the pillar deformation Δl_{pillar} (see Figure 7.3, green), while the y-axis intercept consists of a linear backing layer deformation (Figure 7.3, blue) and an additional nonlinear deformation for pillars with spherical tips (Figure 7.3, red). In Figure 7.14 the slopes *m* derived from Figure 7.12 are

plotted as a function of preload. The slopes, which represent the linear strain portion, increase linearly with preload. This shows that the material behaves in an ideally elastic manner as expected for PDMS.

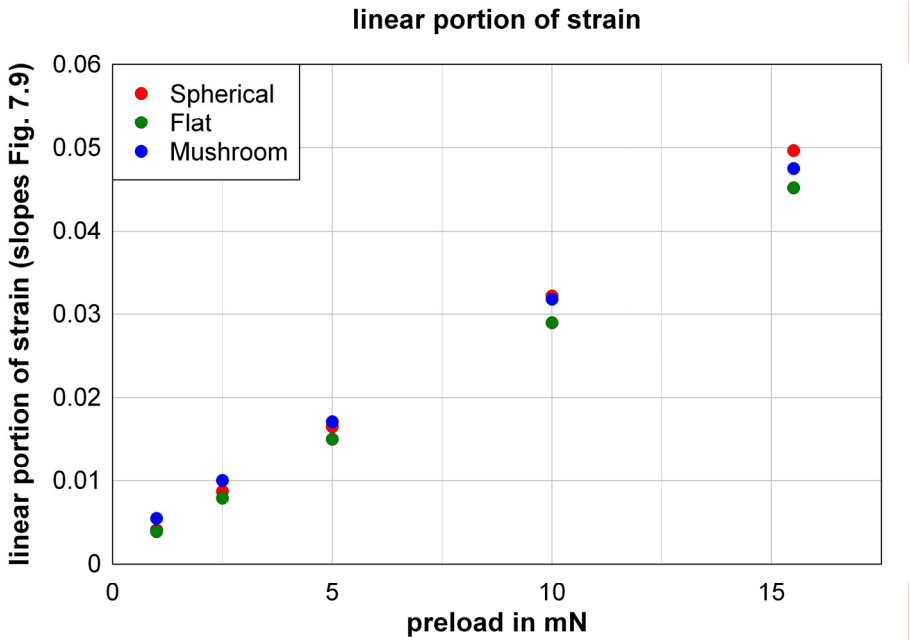

Figure 7.14: The slopes from Figure 7.12 are plotted versus the preload. The linear increase of the slopes with increasing preload shows that PDMS deforms linear elastic, as it is expected.

The graph in Figure 7.15 shows the y-axis intercepts from Figure 7.12 as a function of preload. In case of flat tip pillars, the additional length change increases linearly with preload. Spherical tip pillars show a larger length change than flat tip pillars, while mushroom shaped pillars show a slightly lower compression.

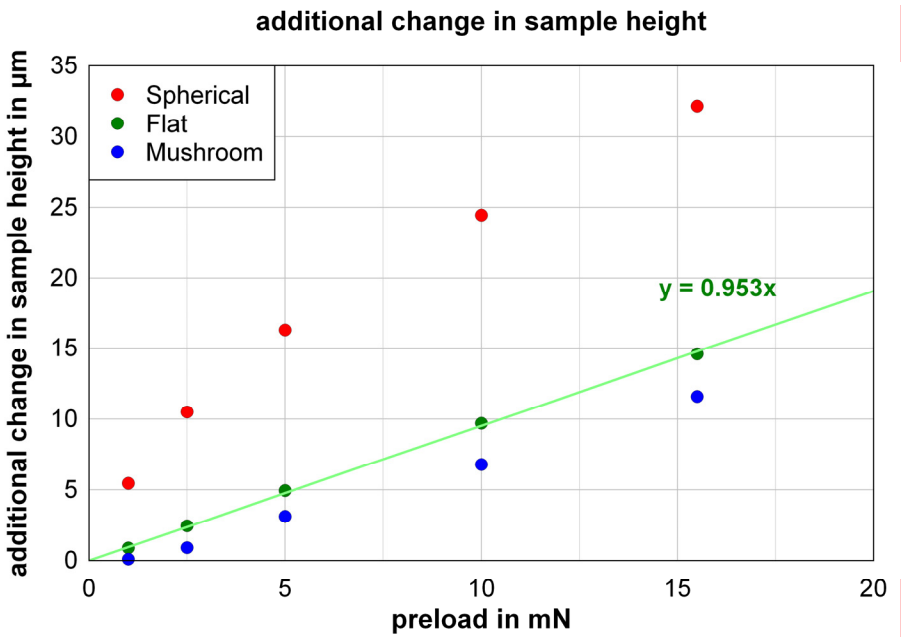

Figure 7.15: Height independent length change as a function of preload (y-axis intercepts from Figure 7.12). The length change is a combination of backing layer and tip deformation.

For the flat tip pillars, no contribution of tip shape to the length change is expected ($\Delta l_{tip} = 0$). From Eq. 7.1 we then obtain $\Delta l_{total} = \Delta l_{pillar} + \Delta l_{backing}$. In this case, $\Delta l_{backing}$ is the only height independent contribution to the deformation. This situation can be considered as an indentation of a polymeric cylinder into an elastic half-space. A similar problem has been investigated by Kendall [4]. Based on Kendall's assumptions, the indentation depth δ of a *rigid* cylindrical probe with radius r into an elastic half-space depends linearly on the load P

$$\delta = \frac{P}{2r}\left(\frac{1-\nu_1^2}{E_1} + \frac{1-\nu_2^2}{E_2}\right) \qquad \text{(Eq. 7.2)},$$

where ν_1, ν_2, E_1 and E_2 are the Poisson numbers and Young's moduli of the materials *1* and *2*, respectively. By assuming the *compliant* cylindrical probe of the presented experiments to behave in a way similar to a *rigid* cylindrical probe, Eq. 7.2 can be simplified to:

$$\delta = \frac{3P}{4rE} \qquad \text{(Eq. 7.3).}$$

According to Eq. 7.3, the indentation depth δ depends linearly on the load P, as found experimentally for the flat tip pillars (see Figure 7.15, green data points).

Both pillar deformation and backing layer indentation may now be subtracted from the measured total length change to determine the additional length change due to different tip geometries. In Figure 7.16 the length change due to backing layer deformation (defined by the fit for the flat tip pillars in Figure 7.15) is subtracted from all values. It can be seen that spherical pillars show a non-linear additional compression (higher compliance) compared to flat tip pillars, while the mushroom tip pillars are less compressed (lower compliance).

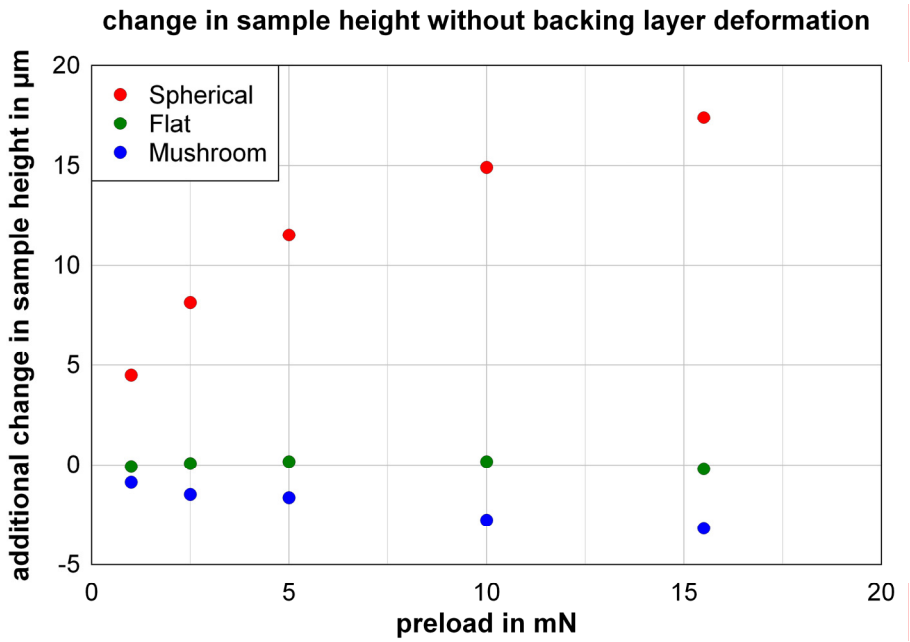

Figure 7.16: The flat tip pillar fit in Figure 7.15 is subtracted from all values in Figure 7.15 and re-plotted. The spherical tip pillars show an additional length change, while the mushroom tip structures have less length change than the flat tip pillars.

The additional length change of the spherical tip pillars has geometrical reasons. Although the forces are the same for all tip geometries, the local stresses at the contact area are the highest for the spherical tip geometry. This leads to the higher sample compression. In principle, the compression data of contact between a spherical tip and a flat rigid half space can be fitted using the Johnson-Kendall-Roberts (JKR) theory [5] (see Chapter 2.4.1). However, as the tip height of the spherical tips (radius of curvature) differs for the tested pillars and the tip compression lies in between 10 and 30% for the highest applied preload, the experimental results are not suitable for comparison with the JKR theory. A graph showing the sample compression of the spherical tip pillars and a JKR fit is shown in 7.7 Appendix.

The "negative" length change for the mushroom tip pillars can be interpreted as a local stiffening of the tips. As schematically shown in Figure 7.3, the mushroom tip does not only increase the contact area, but the diameter of the pillar in the tip region will be larger as well. This locally increased pillar thickness will lead to a more robust structure, which will be more difficult to compress compared to pillars without mushroom tips.

Based on the length change and the force data it is now possible to calculate the apparent Young's modulus for the pillar (barrel-like deformation of the pillar) and the backing layer (deformation constrained in the backing layer plane). As an example, we will now calculate these values for a flat tip pillar sample at a load of 5 mN. From the slopes in Figure 7.12b, we derive a strain of 1.501% at 5 mN load. Dividing the force by the contact area (circle with 200 µm radius) results in a stress of ~ 39.8 kPa. Using the stress and strain data, we calculate a Young's modulus of ~ 2.65 MPa for a single PDMS pillar in compression. Using the data from Figure 7.15 and Eq. 7.3, we derive a Young's modulus of ~ 3.93 MPa for the backing layer in compression. These values lie well within the range of 1.3 MPa to 4 MPa, which were

reported for similarly fabricated Sylgard 184 PDMS samples [6-11]. However, these different values also show that the determination of the Young's modulus strongly depends on the measurement configuration used.

7.5 Conclusion

The flat probe measurements on single pillars allow investigation of the influence of tip shape and AR on angle dependent pull-off force and of the pillar compliance. Angle dependent measurements on micropatterned surfaces as presented in Chapter 6 do not allow a separation of pillar geometry effects and effects due to indentation of the probe into the backing layer. For macroscopic single pillar measurements, however, no probe indentation into the backing layer occurs. Thus the measured effects originate from the pillar geometry. Based on these measurements the following main correlations can be identified.

- The pull-off force is strongly affected by the tip shape of the pillar. Pillars with mushroom shaped tips show the highest pull-off force, followed by flat tip pillars and pillars with spherical tips, as previously reported [5,12].
- Pillars with spherical tips show no angle dependent pull-off force, while the pull-off force for flat tip pillars decreases with increasing tilt angle. Mushroom shaped tips show angle dependent adhesion only for low preload and large tilt angles due to incomplete contact formation. For large preload the pull-off force is angle independent.
- By analyzing the sample compression it is possible to distinguish between pillar deformation (linear, dependent on pillar height), backing layer deformation (linear, independent of pillar height) and tip deformation (non-linear, independent of pillar height). This allows calculation of the Young's modulus.

7.6 References

[1] Paretkar, D. R.; Kamperman, M.; Schneider, A. S.; Martina, D.; Creton, C.; Arzt, E. *Mater. Sci. Eng. C*, in press.

[2] Greiner, C.; del Campo, A.; Arzt, E. Langmuir 2007, 23, 3495-3502]

[3] Maugis, D. *Contact, Adhesion and Rupture of Elastic Solids* **2000** Springer-Verlag Berlin Heidelberg, *Chapter 4.3*, pp. 234.

[4] Kendall, K. *J. Phys. D: Appl. Phys.* **1971**, *4*, 1186.

[5] del Campo, A.; Greiner, C.; Arzt, E. *Langmuir* **2007,** *23,* 10235-10243.

[6] Bar, G.; Delineau, L.; Brandsch, R.; Bruch, M. *Appl. Phys. Lett.* **1999**, *75* (26), 4198-4200.

[7] Deuschle, J. K.; Buerki, G.; Deuschle, H. M., Enders, D.; Michler, J.; Arzt, E. *Acta Mater.* **2008**, *56*, 4390-4401.

[8] Guidoni, G.M.; Schillo, D.; Hangen, U.; Castellanos, G.; Arzt, E.; McMeeking, R. M.; Bennewitz, R. *J. Mech. Phys. Solids* **2010**, *58*, 1571-1581.

[9] Gupta, S.; Carrillo, F.; Li, C.; Pruitt, L.; Puttlitz, C. *Proc. Natl. Acad. Sci. U.S.A.* **2006**, *61*, 448-451.

[10] Schneider, F.; Fellner, T.; Wilde, J.; Wallrabe, U. J. *Micromech. Microeng.* **2008**, *18*, 065008-0650017.

[11] Song, J.; Tranchida, D.; Vancso, G.J. *Macromolecules* **2008**, *41*, 6757-6762.

[12] Gorb, S.; Varenberg, M.; Peressadko, A.; Tuma, J. *J. R. Soc. Interface* **2007**, *4*, 271-275.

7.7 Appendix

The following graph shows the pull-off force for spherical tip pillars as a function of normalized tip radius. The tip radius r was calculated from the tip height h (Table 7.1) and the pillar radius a (200 µm) using $r = \frac{a^2 + h^2}{2h}$ and was then normalized by dividing with a.

With increasing tip radius, the pull-off force increases. To investigate the effect of tip radius on the pull-off force more closely, additional experiments need to be performed, providing a wider variety of tip radii, especially for low tip curvatures.

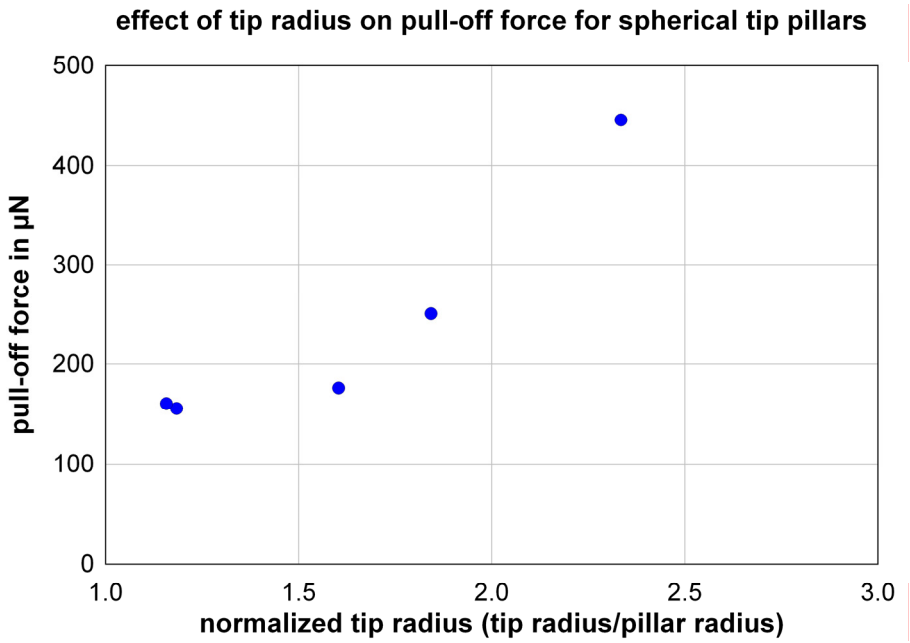

Figure 7.7 Appendix 1: Influence of the tip radius for spherical tip pillars on the pull-off force. The tip radius was normalized by the pillar radius (1.0 = perfect semi-sphere).

The pull-off force as a function of tip diameter for mushroom shaped tips is plotted in the following graph. The tip radius was measured using white light interferometry. The tip radius was then normalized by dividing with the pillar diameter (400 µm). With increasing tip diameter, the pull-off force increases. The graph indicates that the pull-off force scales with the tip diameter (or tip radius). To investigate this correlation, additional adhesion measurements on mushroom shaped tips are necessary.

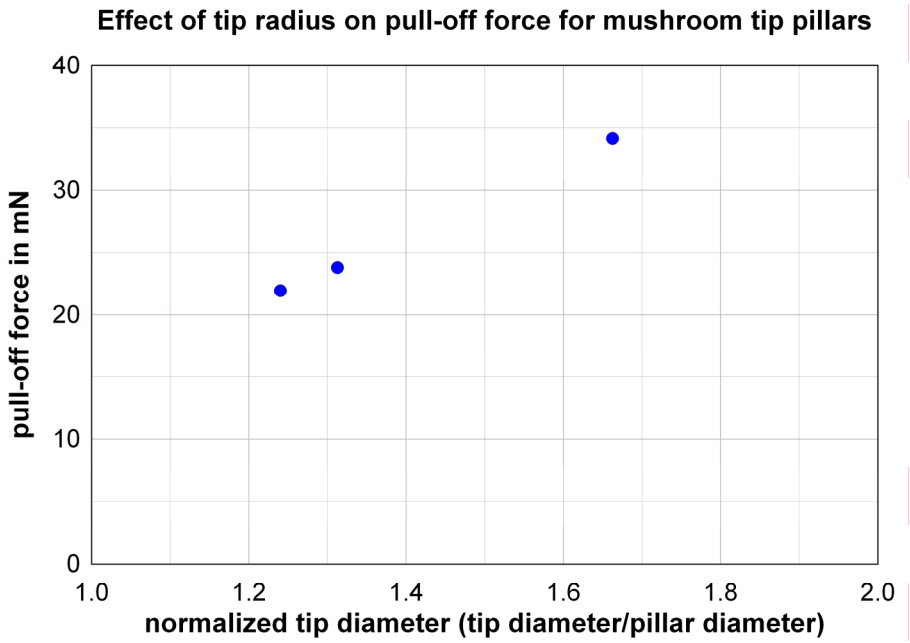

Figure 7.7 Appendix 2: Influence of the tip diameter for mushroom tip pillars on the pull-off force. The tip radius was normalized by the pillar radius.

The results for the spherical tip pillars from Figure 7.14 are plotted in the following graph with a JKR fit. The following parameters were chosen as fit parameters. The mean tip radius from all tips (see Table 7.1) was taken as the tip radius R, which was 324.9 µm. The Young's moduli and Poisson numbers for the spherical tip material (1) and the flat probe material (2) were chosen to be 2.65 MP (E_1) and 100 GPa (E_2) (see Chapter 7.4.3), as well as 0.5 (ν_1) and 0.3 (ν_2), respectively. 0.044 J/m² was taken as the work of adhesion ω. From this data, the indentation depth δ was calculated using

$$\delta = \frac{a^2}{3R} + \frac{2P}{3aK},$$

with $a^3 = \frac{PR}{K}\left[1 + \frac{3\pi\omega R}{P} + \sqrt{2\frac{3\pi\omega R}{P} + \left(\frac{3\pi\omega R}{P}\right)^2}\right]$ and $\frac{1}{K} = \frac{3}{4}\left(\frac{1-\nu_1^2}{E_1} + \frac{1-\nu_2^2}{E_2}\right)$.

The deviation from the experimental data and the JKR fit can be explained by the different tip radii and by the large deformation of 10 to 30% for the highest preload.

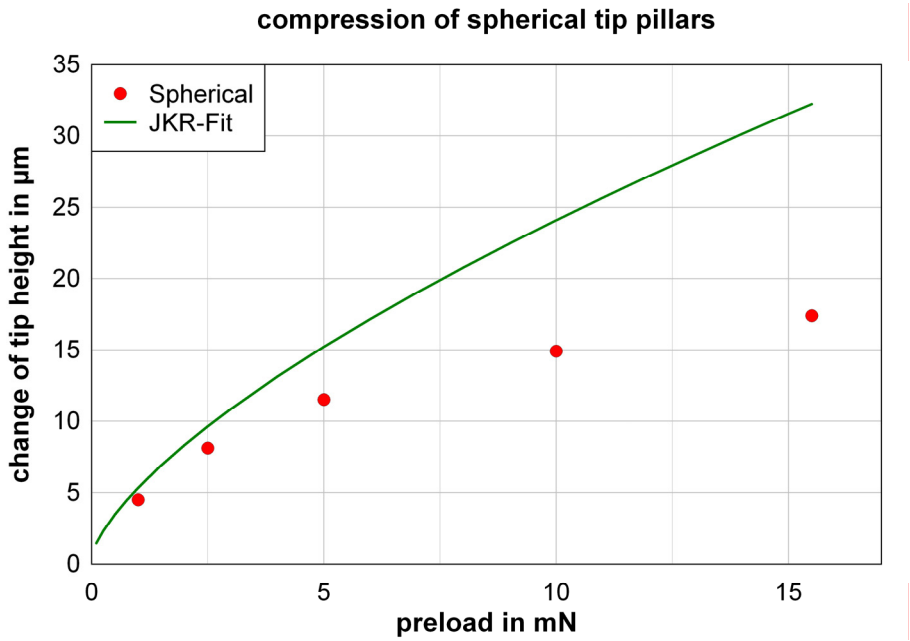

Figure 7.7 Appendix 3: Compression of the tip for spherical tip pillars. The red dots represent measurement data points, the green line a JKR-fit.

8. Summary

During the last decade, scientists around the world have made great progress in understanding and fabrication of gecko-inspired dry adhesives. They developed bioinspired adhesives based with complex structure geometries and provided equally complex theoretical models to describe the adhesion of patterned surfaces. However, the adhesion measurement techniques were not developed to the same extent and experimental results were often published without distinguishing between effects due to the special mechanical properties of bioinspired adhesives or due to the measurement setup.

The goal of this thesis was the investigation of effects which are directly related to the probe used for adhesion measurements. The influences of the surface properties of the probe as well as the probe geometry were investigated.

Sample fabrication (Chapter 3) – A new fabrication process was developed to fabricate templates for soft molding of micropatterned surfaces, consisting of three process steps: photo lithography for the pre-patterning of silicon wafers, reactive ion etching to transfer the pattern onto the silicon wafer and two-step molding to replicate the template geometry. Compared to conventional soft lithography (photo lithography for wafer patterning and a single molding step), the new process had two advantages.

- First, the resulting silicon template was more robust than photo resist-based silicon templates. This allowed easier cleaning of the template as aggressive chemicals could be used to remove residues from the molding process.
- And second, the reactive ion etching process enabled fabrication of new pillar geometries, such as conical or mushroom shaped pillars.

Although this new process necessitated a two-step molding process (the resulting pillar geometry of the templates could only be satisfactorily adjusted for pillars instead of holes), the new process allowed a reproducible and durable template fabrication with an additional degree of freedom to access new pillar geometries. Besides micropatterned polymeric surfaces, single macropillars were fabricated from milled templates using one molding step.

A new adhesion tester (Chapter 4) – To investigate the influence of the probe on adhesion measurements for patterned polymeric surfaces, a new experimental set-up was installed, in the following referred as MAD (Macroscopic Adhesion measurement Device). The main goal in designing MAD was the possibility to perform adhesion measurements with flat probes under controlled alignment with high force resolution of several μN, large measurement range and *in situ* visualization.

The set-up is composed of two main parts, an accurate sample positioning and a tilt sensitive force measurement. The sample positioning was realized by combining a six-axis table with a piezo stage, allowing high precision sample displacement as well as sample movement and rotation along all geometrical axes. The force sensing system was built from a newly developed double-clamped cantilever design, where large displacements were possible. The cantilever displacement was measured using a laser interferometer, which served both as a

high resolution displacement acquisition and a passive tilt control for the cantilever. If the cantilever experienced any torsion during measurement, the laser beam was not reflected back to the interferometer and the measurement was halted. By using a mirror system, the experiments could be visualized in side-view and top-view mode. MAD allowed adhesion measurements with a force resolution of a few μN and a force rage up to N at an angle precision of 0.02°. In addition, due to the constant contact area of the flat probe during the experiment, simple data analysis procedures were possible to determine stress, strain, Young's modulus and work of separation for each phase of the adhesion measurement.

Repeated adhesion measurements (Chapter 5) – Repeated adhesion measurements with a spherical probe were performed on flat (unpatterned) polydimethylsiloxane (PDMS) samples, to investigate the repeatability of the adhesion measurement process. The change in pull-off force as a function of number of contacts was measured for samples fabricated using different process parameters. It was found that the pull-off force decreased significantly during the first few contacts and leveled out after several hundreds of contacts. The initial pull-off force value and the rate of change strongly depended on the sample preparation procedure, for example curing time, cross-linking density, sample relaxation time and others. However, all samples showed comparable pull-off forces after approx. 1000 contacts. This behavior was explained by a gradual coverage of the probe with uncured oligomers from the PDMS sample. While the surface energy and the oligomer-polymer interactions changed during the first contacts, the probe-sample system reached a dynamic equilibrium after a certain amount of contacts, resulting in pull-off forces independent of the number of further contacts.

Comparison of flat and spherical probes (Chapter 6) – Adhesion measurements were performed on flat samples and arrays of low aspect ratio (AR) PDMS pillars using flat and

spherical probes. Experiments using spherical probes resulted in angle independent (but preload dependent) pull-off forces for flat and patterned samples. However, a strong angle dependency was found for experiments using flat probes. While measurements in the aligned state resulted in preload independent pull-off force values, the pull-off force dropped significantly with increasing misalignment of the probe and became preload dependent. For example, a misalignment of 1° resulted in a pull-off force reduced by 60% for a flat probe on a flat PDMS sample. This drop was more pronounced for patterned samples than for flat ones, where a misalignment of only 0.4° was sufficient to reduce the pull-off force to 60% of the initial value. By comparing the results from flat and spherical probes, it was shown that the ratio of pull-off force between patterned and flat PDMS samples was different for the applied probe geometries. Adhesion measurements with spherical probes resulted in lower pull-off force ratios compared to flat probe measurements. The angle dependent pull-off force of a flat punch in contact with a flat elastic half-space was modeled. For larger misalignment, the model predicted a linear dependency of the pull-off force on the tilt angle, which fitted very well with the experimental data.

Single pillar measurements (Chapter 7) – Angle dependent flat probe adhesion measurements on micropatterned surfaces had the drawback that it was not possible to distinguish between angle dependent adhesion of the pillars and indentation effects of the probe into the backing layer. For this reason, macroscopic single pillars with diameters of 400 µm, AR of 1 to 5 and different tip shapes (spherical, flat and mushroom shaped tips) were fabricated. Adhesion measurements with a flat probe and controlled alignment revealed that spherical tip pillars did not show an angle dependency of the pull-off force. In contrast, flat tip pillars showed a strong tilt angle dependent adhesion. The pull-off force for mushroom tip pillars was only tilt angle dependent for small preload and high tilt angles, where the pillar tip

did not form complete contact with the probe. By analyzing the sample compression, it was possible to determine the contribution of the pillar, the backing layer and the tip to the deformation. Thus, the apparent Young's modulus was calculated for two cases, the deformation of a free standing pillar and for the backing layer.

Outlook – The results of this thesis have shown that adhesion experiments with flat probes provide new insights into contact phenomena of patterned surfaces. It is clear that the normal adhesion changes not only with the mechanical properties of the chosen polymeric materials and the geometry of the surface pattern, but also with the geometry of the probe. The possibility to perform adhesion experiments with flat, aligned probes in combination with *in situ* visualization opens up a new way of data interpretation.

It is proposed that additional adhesion experiments on single macropillars should be performed to help understand the effects of pillar geometry on adhesion. Macropillars are easy to fabricate, allow accurate *in situ* observation of detachment mechanisms or buckling effects and their geometry can be precisely controlled. Studying the influence of tip curvature for spherical tip pillars or mushroom tip diameter on their adhesive properties will give a deeper insight into the adhesion of pillar structures. To solve the question of scaling, it is necessary to investigate the adhesive properties for pillars with different sizes. Thus, in addition to macropillar experiments, similar experiments on single micropillars could be performed. Such experiments will show the effect of pillar size, e.g. on angle dependent adhesion; is there a size effect at all? Do macroscopically observed effects scale with size? Do new effects occur below a certain critical size? However, these measurements will require a sophisticated adhesion measurement system, for example *in situ* scanning electron microscopy adhesion experiments on single micropillars.

One of the most important studies concerning adhesion of patterned surfaces will be the adhesion on rough surfaces. The pull-off forces for the single mushroom tip pillars reported in Chapter 7 indicate that high adhesion on smooth surfaces can already be achieved with macropillars. If the value for the single pillar is calculated into pull-off strength values by assuming a pillar packing density of 22.7% (hexagonal, center-to-center spacing of twice the diameter), a pull-off strength of more than 60 kPa is found. This value indicates that high normal adhesion on smooth surfaces can be achieved with large pillars. The strength of the gecko adhesion is the ability to stick on all kind of surface roughness. Thus, micropatterned surfaces should be tested in the disciplines where they are supposed to be superior: on rough surfaces.

An important focus in research on adhesion of patterned surfaces should be the combination of different functionalities for specific applications. Such multi-functional adhesives may find wide application in different fields. For example, adhesives could be designed in a way to both provide high adhesion to smooth glass surfaces and at the same time serve as optical coupling to the contacting glass surface, which could be interesting for optical applications. Another possibility would be the combination of adhesion to soft and humid tissue and a controlled directional cell growth, which would allow the adhesive to be used as an implant material in biomedical applications.